ADDIS ABABA UNIVERSITY

COLLEGE OF NATURAL AND COMPUTATIONAL SCIENCES

SCHOOL OF EARTH SCIENCES

TITLE ON: MAPPING OF FERRIC (Fe^{3+}) AND FERROUS (Fe^{2+}) IRON OXIDES DISTRIBUTION USING ASTER AND LANDSAT 8 OLI DATA, IN NEGASH LATERITIC IRON DEPOSIT, NORTHERN ETHIOPIA.

By: H/mikeal Hans

ID: GSR/3937/2012

Advisor: Dagnachew Legesse (Ph.D.)

Addis Ababa, Ethiopia

Sep, 2021.

ADDIS ABABA UNIVERSITY

COLLEGE OF NATURAL AND COMPUTATIONAL SCIENCES

SCHOOL OF EARTH SCIENCES

MAPPING OF FERRIC (Fe^{3+}) AND FERROUS (Fe^{2+}) IRON OXIDES DISTRIBUTION USING ASTER AND LANDSAT 8 DATA, IN NEGASH LATERITIC IRON DEPOSIT, NORTHERN ETHIOPIA.

A THESIS SUBMITTED TO THE SCHOOL OF GRADUATE STUDIES OF ADDIS ABABA UNIVERSITY IN PARTIAL FULFILLMENT OF THE REQUIREMENTS FOR THE DEGREE OF MASTERS OF SCIENCE IN REMOTE SENSING AND GEO-INFORMATICS.

By: H/mikeal Hans

ID: GSR/3937/2012

Advisor: Dagnachew Legesse (Ph.D.)

Addis Ababa, Ethiopia.

Sep, 2021.

Addis Ababa University School of Graduate program

This is to certify that thesis prepared by Haylemikeal Hans Abay, entitled "***Mapping of ferric (Fe^{3+}) and ferrous (Fe^{2+}) iron oxides distribution using ASTER and Landsat 8 OLI data, in Negash Lateritic iron deposit, Northern Ethiopia.***" submitted in partial fulfillment of the requirements for the degree of Master of Remote sensing and geo-informatics stream obey the regulations of the university and meets the expected standards concerning the originality and quality. Approved by the thesis examining committee.

Dr. Dagnachew Legesse	_____	05/10/2021
Advisor	Signature	Date
Prof. Solomon Tadesse	_____	____/____/____
Examiner	Signature	Date
Dr. Tibebu Kassawmar	_____	____/____/____
Examiner	Signature	Date
Head, School of Earth sciences		____/____/____
Signature		Date
_____		____/____/____

DECLARATION

I hereby declare that the dissertation entitled "**Mapping of ferric (Fe^{3+}) and ferrous (Fe^{2+}) iron oxides distribution using ASTER and Landsat 8 OLI data, in Negash Lateritic iron deposit, Northern Ethiopia**." has been carried out by me under the supervision of Dr. Dagnachew Legesse, Associate professor of Remote Sensing and Geo-Informatics, School of Earth Sciences, Addis Ababa University during the year 2019-2021 as a part of Master of Science program in Remote Sensing and Geo-informatics. I further declare that this work has not been submitted to any other University or Institution for the award of any degree or diploma.

Addis Ababa, Ethiopia
Date: September 2021

Haylemikeal Hans

Acknowledgments

I am extremely thankful to my advisor Dagnachew Legesse (Ph.D.), Associate Professor of Remote Sensing and Geo-Informatics, School of Earth Sciences, Addis Ababa University for his patient, valuable, constructive, and progressive comments and advice, and criticism throughout this work.

I am also grateful to Mekelle University for financial support to pursue my post-graduate study in remote sensing and geo-informatics Stream, under the college of natural and computational sciences at Addis Ababa University.

I would like to extend my gratitude to Balemwal Atnafu (Ph.D.), Head, School of Earth Sciences, Addis Ababa University for all his support during this thesis; and the School of Earth Sciences, Addis Ababa University, for letting us access Remote Sensing and GIS Lab facilities.

I am also grateful to all my friends and Remote Sensing and Geo-Informatics stream classmates for their contribution of ideas and encouragement during the study and this research work.

Table of Contents

List of Figures

List of Tables

List of Acronyms

ALOS - PALSAR	Advanced Land Observing Satellite- Phased Array type L-band Synthetic Aperture Radar
ARCGIS	Aeronautical Reconnaissance Coverage Geographic Information System.
ASTER	Advanced Spaceborne Thermal Emission and Reflection Radiometer
BIL	Band Interleaved by Line
CSAE	Central Statistical Agency of Ethiopia
DN	Digital Number
DEM	Digital Elevation Model
EMA	Ethiopia Metrological Agency
EMD	Ezana Mining Development
EMR	Electromagnetic Radiation
ENVI	Environment for Visualizing Images
FPCS	Feature-Oriented Principal Components Selection
GII	Geospatial Information Institute
GSE	Geological Survey of Ethiopia
L1T	Level One Trigger
LSU	Linear Spectral Unmixing
NASA	National Aeronautics and Space Administration
MF	Matched Filtering
MNF	Minimum Noise Fraction
MOME	Ministry of Mine and Energy of Ethiopia
MT	Mixture Tuning
MTMF	Mixture Tuned Matched Filter
N-D	N -Dimensional
NDVI	Normalized Difference Vegetation Index
NIR	Near Infrared
OLI	Operational Land Imager
PC	Principal Component
PCA	Principal Component Analysis
PPI	Pixel Purity Index
RCC	Ratio Color Composite
RGB	Red-Green-Blue

SD	Standard Deviation
SFF	Spectral Feature Fitting
SWIR	Short-Wave Infrared
TIR	Thermal Infrared
USGS	United States Geological Survey
X	Mean
XLSTAT	Statistical Software for Microsoft Excel
VNIR	Visible to Near-Infrared

Abstract

Iron play important role in the industrial and engineering development of a country and there is a rapid demand for iron in Ethiopia. However, the search for valuable and means of primary mineral resource exploration remains challenging and costly. Therefore, this study aims to map iron oxide minerals using Landsat-8 Operational Land Imager (OLI) and Advanced Spaceborne Thermal Emission and Reflection Radiometer satellite imagery in Negash Lateritic iron deposit, Northern Ethiopia. Different image processing techniques such as band ratio, selective principal component analysis, linear spectral unmixing and mixture tuned matched filter were used to produce iron oxide maps. Minimum Noise Fraction (MNF), Pixel Purity Index (PPI) and N-dimensional visualizer were also applied to extract endmembers in Automated spectral hourglass wizard. First, Normalized Difference Vegetation Indices (NDVI) were calculated and values greater than 0.4 and 0.3 for ASTER and Landsat 8 OLI were used to mask vegetation and, reduce the effects of vegetation on the processed image, respectively. Band ratio of band-2/band-1 and band-5/band-3 + band-1/band-2 of ASTER, band-4/band-3 and band-6/band-4 of Landsat 8 OLI was used to map ferric (^{3}+) and ferrous (^{2}+) respectively. In addition to this, the enhanced image thresholding (from ratio, selective PCA and unmixing) through a varying percentage of confidence level and scatter plot (from MTMF) were used to map anomalous (potential) areas. Ferric iron oxide band ratio of ASTER mapped maximum area of 62.1 km^2 followed by a laterite band ratio of ASTER covering 57.8 km^2. The result shows a high correlation between results obtained using selective PCA with r = 0.59, and r = 0.3 moderate correlation between ferric iron, a poor correlation for ferrous iron with r = 0.22. The correlation result shows that iron oxides mapped from the selective principal component analysis have a better correlation with one another. The result was validated using existing iron oxide polygons and results obtained from selective PCA show a strong match with the existing iron oxide polygons. The sub-pixel mapping techniques show poor accuracy in mapping goethite and hematite relative to the pixel level. Results obtained from ASTER images show a better match with the existing iron oxide polygons. The comparison shows ASTER mapped better than Landsat 8 OLI for band ratio selective PCA, unmixing and MTMF. In poor countries like Ethiopia applying these techniques is a good option to map and use as preliminary exploration tools.

Keywords: Endmembers extraction, Selective PCA, band ratio, LSU, MTMF.

CHAPTER ONE

1 INTRODUCTION

1.1 Background

Different researchers have provided different definitions for laterite. Laterite is defined as the consolidated product of humid tropical weathering predominantly composed of goethite, hematite, kaolin, quartz, ± bauxite and other clay minerals. It is red, brown to chocolate-colored at the top showing hollow, vesicular, and botryoidal structure (Haldar, 2018). Based on Widdowson, (2007) the term laterite, in its general sense, is given to a range of iron-rich, subaerial weathering products that develop as a result of intense, substrate alteration under tropical or sub-tropical climates. On the other hand, Prasad and Parthasarathy, (2018) defined it as a typical rock formation found commonly in the tropical monsoon regions as a capping over the hillocks. Laterites are residual sedimentary rocks, reddish or brownish colored, comparatively soft rocks, containing a high degree of porosity and are carrying vermiform structures. Laterites consist mainly of the minerals kaolinite, goethite, hematite, and gibbsite, which form in the course of weathering (Schubert, 2015).

Iron is the world's most commonly used mineral resource that accounts for almost 95% of all metal used per year. It is used primarily in structural engineering and in automobiles, generally in industrial applications. Worldwide, China is currently the largest consumer of iron ore, which makes it the world's largest steel-producing country followed by Japan and Korea (Chen *et al.*, 2020). The world's iron ore resources are hosted within low-grade terrains. Africa's role as a major world producer of iron ore has been based on sedimentary Precambrian rocks, particularly in western Africa (Gardiner, 2021). Among many sedimentary lateritic iron occurrences reported from the African continent, few are also reported from the Arabian Nubian Shield (Teklay Gidey *et al.*, 2020).

Ethiopia is one of the NE African countries with not many known iron deposits except the few occurrences such as the mafic intrusions hosted Bikilal P-Ti-Fe deposit in western Ethiopia; iron-rich laterites. According to Solomon Tadesse, (2009) and Teklay Gidey *et al*., (2020) there are three types of iron occurrences in Ethiopia. These are; magmatic iron (Fe- Ti type), banded iron formation (BIF) and secondary iron ores (lateritic and gossan) related deposits. These iron deposits are found in; Wollega (Chago, Dha, Gordona-Korree, Worakalu, Belowtuist, Katta valley, Yubdo); Kaffw (Garo, Melka Sedi, Dombova, Mai Guda); Sidamo (Melka Arba) and

Tigray (Adwa, Wukro and Enticho) (Hamrla, 2019; Solomon Tadesse, 2009). On preliminary investigation, other iron deposit occurrences are found in the localities such as Famasari, Billa, Gambo, Gambella, Dembidollo, Gebi-Daleti (Wollega), Assale, Beliga, Chilachii Adi Berbere (Tigray), Bissidimo, Galeti, Kunni, Ujau, Soka (Ham), Ghimira, Bash and Kurkure. And other lateritic/gossan-related iron occurrences are also identified in the Shire, Wukro (Mukuat) and Shiraro (EMD, 2007). According to MOME, (2009) field characteristics of Mai Gudo, Melka Sedi and Dombova lateritic iron deposit shows that these regions are dominated by trachyte rhyolite, dolerite and olivine-rich basalt. Besides these, there are also ferriferous lateritic iron formations in Tigray province. Some of the lateritic iron occurrences localities found in this province are; Adwa, Wukro and Enticho. These iron occurrences are similar to those in Eritrea and connected to the basement rocks as well as to the Mesozoic formations of Adigrat sandstones. In Adwa, Wukro and Enticho, the mineralization of lateritic iron crust has a maximum thickness of 5 to 6m, but the weathered zone of the sandstones is much thicker (Hamrla, 2019) and the average grade of iron metal is about 45%. Further exploration indicates there the lateritic iron ore occurrence in Adwa contains 0.672Mt reserve with an average iron ore grade of 23.9 % (EMD, 2007). The Enticho lateritic iron deposit is found 7km north of Enticho town along the Enticho-Gerhusernay road. Basement rocks such as metasedimentary and metavolcanic rocks are covering low-lying areas and are overlain by Phanerozoic sandstone. The estimated resource and reserve of iron ore in this area are 6.8Mt and 1.8Mt with 26% Fe (EMD, 2007). In addition to that, there are also other lateritic iron deposit occurrences at Shire, Wukro (Mukuat) and Shiraro areas (EMD, 2007). The Shiraro lateritic iron occurrences are identified in two localities: Mentebteb lateritic iron deposit occurrence is found 13 km south of Shiraro in the vicinity of Shiraro-Hummera road and Adamit lateritic iron deposit found about 20km west of Shiraro. The deposit is exposed as discontinuous patches in different directions. It has a reddish to the dark reddish-brown color of pebbles, cobbles and boulder size fragments cemented by a whitish clay matrix. The estimated resource and reserve are 29 and 7.2Mt respectively with an average iron ore grade of 24.85% (EMD, 2007). Shire lateritic iron deposit is occurring 3km from Shire town along the road from Shire to Kisad Gaba and the second is occurrence about 12km from Shire in Adi Kokeb locality. In most parts of the area, the dark brown iron deposit is underlain by a light-to-light brown massive Phanerozoic unit which contains boulder size dark brown iron-rich nodules and it is underlined by ferruginous sandstone, mudstone and quartz-rich conglomerate. Mukuat iron deposit is also another lateritic iron

occurrence at about 5km north of Wukro. The geology of the area is covered by meta black limestone, slate and phyllite units aligned in an east-west while, the lateritic iron deposit has reddish, brownish, yellowish to dark color (EMD, 2007; EMD, 2011; Solomon Gebresilassie *et al.*, 2012).

Iron oxide minerals are developed around many mineral deposits due to the oxidation of sulfide minerals. Geology is one of the most successful areas of remote sensing applications. One of the key motivations for developing the first multispectral satellite systems, such as the Landsat satellites, which were launched in 1972, was to map minerals from space. Modern satellites, like Landsat 8, Sentinel-2, and ASTER, have made progress in this area by providing more accurate measurements at higher resolutions. The main application aspects of geological remote sensing include identification and mapping, geological origin information detection, metallogenic prognosis, resource prediction and evaluation and so on, all of which mineral identification is the groundwork. One of the best cost-benefit methods for mineral mapping involves the application of remote-sensing data (Ducart *et al.*, 2016). Minerals containing iron oxide/hydroxides, such as limonite, jarosite, and hematite, have spectral absorption characteristics ranging from 0.4 to 1.1 µm in the electromagnetic spectrum (Beiranvand *et al.*, 2019; Pour and Hashim, 2014).

1.2 Statement of the problem

Mineral exploration relies on lithological mapping to get a better understanding of the geologic area and to help define viable exploration targets before more intense field research. Although many researchers such as Solomon Gebresilassie *et al.*, (2012) in the Mukuat iron deposit, Teklay Gidey *et al.*, (2020) in the Maikuhli area and Ezana mining development in a different part of Tigray have done a significant amount of work using ordinary methods, there is an increase in iron deposit exploration over time to time. Remote sensing methods can be used to map bedrock and determine the presence and quantity of specific diagnostic minerals at a certain scale and is an additional tool for geologists/researchers to understand the overall lithologic and structural history of the area and to define potential exploration targets. In Ethiopia, the lack of modern exploration methods, such as space-and airborne surveys combined with ground surveys, cause it to take more time and money for studying large areas to delineate promising zones for more detailed studies by ground follow-up. So far, most of the previous studies have been done using traditional field exploration methods (Abera Fantaye, 2009). This work aims to apply and

validate different digital image processing techniques for iron ore mapping which are time and cost-effective.

1.3 Objectives

1.3.1 General objective

Mapping of ferric (Fe^{3+}) and ferrous (Fe^{2+}) iron oxides distribution using ASTER and Landsat 8 OLI data, in Negash Lateritic iron deposit, Northern Ethiopia.

1.3.2 Specific objectives

1. Generating Iron oxide maps and identifying anomalous (potential) areas from ASTER and Landsat 8 OLI images in Negash Lateritic iron deposit, Northern Ethiopia.

2. Extracting endmembers for abundance mapping.

3. Applying MTMF and LSU for abundance mapping of the iron oxides from ASTER and Landsat 8 OLI.

4. Correlating, comparing and validating results obtained from ASTER and Landsat 8 OLI.

1.4 Research questions

1. How to generate mineral abundance maps and identify anomalous(potential) areas?
2. How many endmembers were used to map the abundance of iron oxides?
3. How to apply sub-pixel mapping techniques for abundance mapping?
4. What is the correlation between results obtained by analysis of ASTER and Landsat 8 OLI?
5. Which sensor performs better?

1.5 Significance of the study

The study results include maps showing abundance maps of iron oxides mapped, through different techniques which can be used for researchers as a reference for those who are interested to apply digital image processing techniques and those who are interested to do further study in the area. It will also offer a better understanding of how remote sensing and GIS technologies are applied in mapping iron oxide minerals.

1.6 Organization of the thesis

The thesis is divided into six chapters. The first chapter covers the background, statement of the problem, research questions, significance of the study, and research objectives. The mineral

mapping using satellite imagery, review of iron oxide mapping techniques, endmember extraction procedures, and iron oxide occurrence in Ethiopia are all included in Chapter 2 of the study. The study area description, data (primary and secondary data) and methods (endmember extraction, iron oxide mapping, and anomalous mapping techniques) are described, in Chapter 3: Methodology. The results of preprocessing, endmember extraction, iron oxide mapping, and correlation and validation are presented in Chapter 4. The findings of this study are discussed in Chapter 5. Finally, the Conclusion and recommendations are in Chapter 6.

CHAPTER TWO

2 LITERATURE REVIEW

2.1 Mineral mapping using satellite imagery

Mineral detection using remote sensing techniques is vital since it saves the time and effort of carrying out manual land surveys. Remote sensing has confirmed a valued aid during the early stages of mineral exploration in alteration mineral mapping (Ranjbar *et al.*, 2004; Rowan *et al.*, 2000). It is known that the digitally processed satellite images can be used to locate the assemblages of hydrothermal alteration minerals such as iron minerals, silica, and clay. Mineral identification is mainly based on the spectral characteristics in the visible near-infrared (VNIR) bands in 0.4-2.5 μm, and these characteristics are related to certain chemical compositions and lattice structures of minerals and rocks (Grebby *et al.*, 2014; Ni *et al.*, 2020). The physical technology of hyper- and multi-spectral sensors is the same. They both measure radiation in the Visible to Near-Infrared (VNIR) and Short-Wave Infrared (SWIR) regions of the spectrum, with VNIR encompassing 400–1000 nm and SWIR 1000–2400 nm, respectively (Transon *et al.*, 2018). Unlike multispectral sensors like Landsat-8 (11 bands), which record in a relatively small number of discrete spectral bands (4–20), hyperspectral sensors record in a high number of continuous and narrow spectral bands of 5–15 nm (Kaufmann *et al.*, 2009). Because of the widespread applications of multispectral remote sensing data. Different researchers used different images for mapping different minerals and alterations. Some of them are as follow:

Rouskov *et al.*, (2005) applied ASTER images have been shown to be extremely useful in geology and mineral exploration. For mapping distinct rock and hydrothermal alteration types, basic band rationing approaches can be quite beneficial. On the ASTER image of the examined area, the spatial distribution of iron oxides and clay minerals is well mapped. Band ratios 2/1, 4/3 and 4/5 were used for the recognition of iron minerals versus alterations.

Mishra *et al.*, (2014) studied on geospatial and geological mapping of iron ore prospective zones in Singhbhum – Keonjhar belt, Orissa. This research work explained the usage of Advanced Space-borne Thermal Emission and Reflectance Radiometer and Thematic Mapper data to deduce anomalous zones of Iron ore mineralization. Spectral properties are used to separate units in image data based on the spectral reflectance of the minerals. Band Ratio, Principal Component Analysis (PCA), Band combination, Ls-Fit image processing techniques have been commonly applied on Visible and near-infrared (VNIR) and Short-Wave Infrared (SWIR) sub-region of the

ASTER dataset to locate iron oxide minerals. ASTER imagery with Visible and near-infrared (VNIR), Short Wave Infrared (SWIR) and Thermal Infrared (TIR) bands were also used to delineate structural features, lineament pattern, geological setting, geomorphological anomalies, land use and land cover units, Digital Elevation Model & 5m contour that were also formulated between these parameters to map the zones characterizing potential Iron ore. And geological datasets available from the field were further correlated with the remote sensing database to define probable zones of Iron ore mineralization.

Crósta *et al.*, (2003) used ASTER imagery and principal component analysis to conduct a case study on targeting important alteration minerals in epithermal deposits in Patagonia, Argentina. The goal of this work was to map the occurrence of mineral endmembers associated with an epithermal gold potential using principal component analysis on ASTER bands encompassing the SWIR bands. The findings demonstrated ASTER's potential to offer valuable information on alteration minerals for mineral exploration, and they supported the use of principal component analysis as a particularly effective and robust image processing methodology for that purpose.

In the south High Atlas of Marrakech, Ourhzif *et al.*, (2019) used the multispectral Advanced Spaceborne Thermal Emission and Reflection Radiometer and Landsat 8 Operational Land Imager data to map lithological units and structural maps. Principal component analysis (PCA), band ratios (BR), and minimum noise fraction (MNF) transformation were employed as analytic methods. The Advanced Space-borne Thermal Emission and Reflection radiometer satellite's geomorphic characteristics, textures, and multispectral data were combined using a Support Vector Machine (SVM) classification algorithm. The use of SVM methods on ASTER and Landsat satellite data demonstrates that they can be used as a powerful tool to investigate and improve lithological mapping in mountainous semi-arid areas; the overall classification accuracy of Landsat 8 OLI data is 97.28 percent, and the Kappa Coefficient is 0.97. ASTER's overall classification accuracy with nine bands (VNIR-SWIR) is 74.8%, and the Kappa Coefficient is 0.71. Landsat 8 OLI ratio 4/2 was used for mapping iron oxides because it has an absorption in the blue region, where it has a high reflectance in the red region and ASTER ratio (2/1) was used the map the Ferric iron, Fe^{3+}.

Sadeghi *et al.*, (2013) employed ETM+ and ASTER sensors to locate iron deposits in central Iran's Esfordi. The goal of this study was to use Landsat ETM+ and Advanced Spaceborne Thermal Emission and Reflection Radiometer satellite data to locate and identify iron-bearing

occurrences. Linear Band Prediction (LS-Fit), Matched Filtering, Spectral Angle Mapper, Spectral Feature Fitting (SFF), Band Ratio (BR: 2/1 and 3/1) and Visual interpretation are some of the methods employed (RGB: 531). Visual interpretation of images and band combinations were used to identify structures (RGB: 431). An iron ore potential map for the study area was created using remote sensing techniques.

Alasta, (2011) used remote sensing data to identify iron deposits occurring in the Wadi ash shakti in the central part of western Libya. In this work, several advanced image processing techniques were applied and tested on a TM image of the study area. By applying ER mapper image processing techniques, color composites, band ratios, principal components PCA and supervised classification, images were created for enhancing mineral detection in this study. The final detection of the iron deposit was based on the difference in reflectance of the iron oxide content.

In the N4, N5, and N4WS iron deposits, Serra Norte, Carajás, Brazil, Ducart *et al*., (2016) used mapping methods for iron oxides and clay minerals, combining Landsat-8/Operational Land Imager and Earth Observing 1 (EO-1)/Hyperion imagery with aerial geophysical data. On Landsat-8/OLI data, band ratios were attained, permitting the identification of the principal minerals from iron deposits. Even in vegetated shrub areas, the Landsat-8/OLI imagery performed well for iron oxide investigation. The band ratio method, which was applied to Landsat-8/OLI data in the N4 and N5 open-pit sites, demonstrated to be appropriate for remote mapping of iron oxides and/or clay minerals. For mapping high-grade iron ore in N4 and N5 locations, the band ratio (4+6)/5 produced the best results. In the N4 and N5 areas, band ratio 4/2 accurately indicates iron oxides mostly associated with mafic saprolites from the Igarapé Cigarra Formation, as well as iron oxides under vegetation cover in the N4WS area. The Landsat-8 OLI band ratio 6/7 divided by the ratio 5/4 yielded an appropriate index for detecting clay minerals. In the sparsely vegetated N4WS area, no differences between mineral canga and chemical canga were found.

Gopinathan *et al*., (2020) employed ASTER band rationing to map the distribution of ferric (Fe^{3+}) and ferrous (Fe^{2+}) iron oxides in Kanjamalai and Godumalai, Tamil Nadu, India. To detect and describe the iron ores in Kanjamalai and Godumalai locations in Tamil Nadu, India, using spectral remote sensing and digital processing of ASTER data. The abundance of iron oxides, comprising ferric (Fe^{3+}) and ferrous (Fe^{2+}) components, was assessed using ASTER images. Using a multi-band analysis and the band rationing methodology, the abundance of iron oxide

content in various areas of the research area was generated using different band combinations such as band 2/band 1 (for Fe^{3+}) and band 5/band 3 + bands 1/ band 2 (for Fe^{2+}). The geochemical analysis is an important aspect of this effort to comprehend the relationship between the band ratio and the chemical makeup of the ore samples using band ratio techniques. As a result, Pearson's coefficient of correlation (ρ) was used to determine the correlation between the results of the geochemical analysis of the samples gathered from random places and the corresponding sites in the abundance image.

Abulghasem *et al*., (2011) studied integrated data of remote sensing and geophysical data for iron ore exploration in the western part of Libya. The target of the study is to explore iron ore deposits using remote sensing techniques for the study area using the integration of Enhanced Thematic Mapper Plus (ETM+) images. The authors generated supervised classification image and band ratio images to discriminate and delineate different lithological units in the study area. Ground magnetic data was also used in this study to identify any hidden deposits. Both the outputs were validated with the geochemical investigation. The results showed that the iron ore belt still extends from the study area to the sand dunes-covered area. Based on these data and interpretation, a new ore body map has been produced by researchers.

Abera Fantaye, (2009) studied mapping hydrothermally altered rocks and lineament analysis through the digital enhancement of ASTER data case study: Kemashi area, western Ethiopia. Contrast stretching, HIS transformation, principal component analysis (PCA), band rationing and spatial filtering were applied. The overall result of this study demonstrates that remote sensing method using multispectral data can be very useful for regional hydrothermal alteration, structure, lithologic mapping to provide important data for regional mineral assessment and to define a target for mineral exploration, particularly in the area of good rock exposure (very minor soil development and small or absence of vegetation) and if the interpretation supported by a published geological map and/or sufficient ground truth.

2.2 Iron oxide mapping techniques

There are different iron oxide mapping techniques including various image enhancement techniques such as Principle Component Analysis (PCA), Minimum Noise Fraction (MNF), Band Ratios (BRs), Band Combinations (BCs) and Spectral Indices (Gad and Kusky, 2007; Gad and Kusky, 2006; Rajendran *et al.*, 2012; Rajendran *et al.*, 2013; Van der Meer *et al.*, 2012) spectral mapping algorithms such as Spectral Angle Mapper, Spectral Feature Fitting (SFF),

Matched Filter, Constrained Energy Minimization (CEM), Linear Spectral Unmixing (LSU), Mixture Tuned Matched Filter (MTMF) have been well employed on ASTER datasets to obtain the lithological, mineral and hydrothermal alteration maps with reasonable accuracies (Gad and Kusky, 2007; Gad and Kusky, 2006; Galvao *et al.*, 2005; Gopinathan *et al.*, 2020; Hosseinjani and Tangestani, 2011; Pour *et al.*, 2011; Pour and Hashim, 2012; Qiu *et al.*, 2006). The techniques applied in this study are discussed below:

2.2.1 Image rationing (band ratio)

Rationing is a technique in which the DN value of one band is divided by the DN value of any other band in the sensor array, according to (Alasta, 2011). If both values are near to one, the quotient will be a number close to one. The quotient approaches zero when the numerator is low and the denominator is high. The number is substantially over 1 if the numerator and denominator are flipped (high numerator; low denominator). In a black-and-white display, these new numbers can be stretched or enlarged to form visuals with significant contrast fluctuation. In certain ratios, specific features or materials can produce distinct grey tones; three-band ratio images can be merged to create color composites that highlight certain elements in various ways. Shadowing is likewise reduced or eliminated in ratio images. We divide the DN value of one band by the value of another band for each pixel. This quotient produces a new set of numbers ranging from 0 to 255 (255/1) with the majority being fractional (decimal) values between 0 and generally 2 - 3 (e.g., 82/51 = 1.6078...; 114/177 = 0.6440...). These can be rescaled to create a grey-tone image. Because heavy shadows have values around 0 in all bands, rationing has the effect of eliminating them, resulting in a "truer" depiction of hilly topography in the sense that shaded regions are now depicted in tones similar to the sunshine sides. A worn or altered ore deposit, for example, may develop a distinctive surface staining known as gossan. This stain is made up of hydrated iron oxide (rust), which is often yellow-brown. Band ratios are useful for emphasizing features or materials that aren't visible in raw bands (Inzana *et al.*, 2003).

2.2.2 Principal component analysis

PCA is a method for lowering the dimensionality of such datasets, boosting interpretability while minimizing information loss. It accomplishes this by generating new uncorrelated variables that sequentially optimize variance, according to Jolliffe and Cadima, (2016). The statistical variance in multispectral images is impacted by the statistical dimensionality of the image data and is related to the spectral response of diverse surficial materials such as rocks, soils, and vegetation.

When multispectral images bands are considered as variables and transformed, the ordering of the major components is affected by the spatial abundance of the various surficial materials as well as the image statistics. On the other hand, Principal component analysis (PCA) is a methodology used to accentuate variance and bring out strong patterns in a dataset, according to Powell and Lehe, (2015). It's frequently used to make data exploration and visualization simple.

Guha *et al*., (2018) the Crosta technique, also known as Feature-Oriented Principal Components Selection (FPCS), is a method of analyzing eigenvector values that allow for the identification of PCs that contain spectral information about specific materials, as well as the contribution of each of the component's bands to the spectral response of the material of interest. This technique also indicates whether the materials are represented by bright or dark pixels in the principal components according to the sign and magnitude of eigenvectors.

Traore *et al.*, (2019) used Landsat-8 OLI and Advanced Spaceborne Thermal Emission and Reflection Radiometer data to discriminate Iron deposits using Feature-Oriented Principal Component Selection and Band Ratio Methods: Eastern Taurus/Turkey. They point out that when compared to previously mapped iron deposits, the data produced in this investigation utilizing FOPCS PC4 show an excellent geographical correlation. The important lithologic groupings Carbonate (limestone) can be recovered well from ASTER data, but alluvium can be mapped well using Band Ratio Color Composite in the Landsat -8 OLI images (BRCC). They find that the Landsat-8 OLI and ASTER images provide good precision for detecting iron ore in low-vegetation areas.

2.2.3 Linear spectral unmixing

Spectral unmixing is defined by Shi *et al*., (2016) as the process of deconstructing a mixed pixel's spectral signature into a set of endmembers and their associated abundances. Endmembers are the spectra of the pure components in the image, and abundances denote the percentage of each endmember present in each pixel (Shi and Wang., 2016). Because many spectral unmixing algorithms consider a pixel to be independent of its neighbors, just the image's spectral characteristics are employed to solve the spectral unmixing problem. The endmember should be extracted before unmixing (Shi and Wang, 2014). By finding a solution to the problem of decomposing the mixed reflectance spectrum of each pixel, pi, a linear combination of spectral end-members, peij (subscript i is the band number for the n bands and subscript j is the end-

member), produces fractions, fj, for each end-member (Bangira *et al*., 2017; Van Der Meer, 1999) Eq.(1).

$$pi = \sum_{j=1}^{n} \text{fjpeij} + £i \quad \text{.....(1)}$$

Unmixing can be further constrained by forcing the fractions to be within the range 0< fj < 1 and their sum within 0< fj < 1. The selection of end-members that best represent the spectral dimensionality and spectral variability of the image data is a major challenge in a spectral unmixing analysis. In future analysis, the RMS error image can be utilized to identify new end-members or reposition end-members.

2.2.3.1 Endmember's extraction

Endmembers are a group of constituent spectra that correspond to different ground materials (Keshava and Mustard, 2002). The selection of appropriate, representative endmembers is critical to the accuracy of spectral unmixing (Bangira *et al*., 2017). Endmember spectral fingerprints can be retrieved (1) directly from remotely sensed images (referred to as image endmembers) or (2) measured in the field or lab using spectroradiometers (referred to as reference endmembers) (Hosseinjani and Tangestani, 2011). The difference between image endmembers and reference endmembers is that the first is obtained at the same spatial scale as the image to be analyzed, whereas reference endmembers are usually collected under different atmospheric conditions than airborne or satellite imagery, and at a different spatial scale, due to their proximity to objects (Adams and composition, 1993). Furthermore, collecting adequate endmember spectra for all-important ground components in the field or laboratory is time-consuming (Shi *et al*., 2016). As a result, image endmembers are frequently appropriate for spectral unmixing if they exist in the image and can be precisely retrieved.

2.2.3.2 Endmember extraction methods

Endmembers for the provided study region must be retrieved before modeling the linear mixture for unmixing. The Pixel Purity Index (PPI), Orasis (Optical real-time Adaptative Spectral Identification System), N-FINDR, Iterative Error Analysis (IEA), Convex Cone Analysis (CCA), Automated Morphological Endmember Extraction (AMEE), and Simulated Annealing Algorithm are just a few of the techniques that have been used (Kumar *et al*., 2008; Settle and Sensing, 2006; Winter, 2000).

Pixel purity index (PPI)

Kumar *et al*., (2008) claim that PPI entails a dimensionality reduction using the Minimum Noise Fraction (MNF) transformation and the computation of the PPI for each point in the images cube. This is done by generating lines at random in the N-dimensional space that makes up a scatter plot of the MNF converted data after that, all of the points in the space are projected onto a line. Those pixels above a specific threshold are declared "pure" after several projections to different lines. In the pure pixel list, there could be a lot of duplicated spectra. The actual endmember spectra are chosen by a mix of spectral analysis and N-dimensional visualization. This provides a simple way to comprehend the spectral properties of materials (Kumar *et al*., 2008; Winter, 2000).

N-Dimensional visualization

First pixels from the spectral bands are imported into an N-dimensional scatter plot and rotated on the visualization tool until points or extremities on the scatter plot are exposed, according to Kumar *et al*., (2008). Next, these projections are marked with a region of interest (ROI) tool and rotated in smaller dimensions several times to see if their signatures are distinct. Then mean spectra for each ROI are then retrieved and used as endmembers for spectral unmixing. After that, these endmembers are used for classification and other processing.

Spectral analyst for matching known and unknown spectra

According to (L3harrisgeospatial.com.,2020a) spectral Analyst is a tool that may be used to identify materials based on their spectral properties. The Spectral Analyst ranks the match of an unknown spectrum to the materials in a spectral library using ENVI techniques including Binary Encoding, Spectral Angle Mapper, and Spectral Feature Fitting. For each of the materials in the input spectral library, the Spectral Analyst produces a ranked or weighted score. The highest score implies the closest match and a higher level of spectral similarity confidence. Similar resources may have high ratings, whereas unrelated materials should have low values.

2.2.4 Mixture tuned matched filtering

The partial unmixing classification algorithm Mixture Tuned Matched Filtering (MTMF) is a relatively new image processing technology that has proven to be an effective target recognition tool. Partially unmixing and subpixel target abundance estimates are possible with these techniques, which are not possible with typical mixture modeling or spectral angle mapping algorithms (Mundt *et al*., 2007).

“The “MTMF” technique (also known as CEM and/or orthogonal subspace projection) (Boardman *et al*., 2011; Pour *et al*., 2021). was designed to leverage mixing between a target of interest and the background to solve the “selectivity” problem inherent in existing classical MF techniques (also known as CEM and/or orthogonal subspace projection). Targets are replacing a portion of the backdrop signature in a pixel, according to the MTMF approach (not adding to it as has often been proposed in target detection schemes). MTMF improves performance over MF alone by combining components of hyperdimensional convex geometry spectral unmixing and statistical matched filter target detection. It maintains the MF's ease of calculation while allowing for increased target selectivity, excelling at the accurate mapping of extremely small subpixel targets with low false alarm rates. When utilized on the same input data as other apps that previously had a high number of false alarms, MTMF frequently delivers low false alarm rates. This increase in performance demonstrates the effectiveness of the approach's mixture tuning (MT) component. More challenging applications are needed to fully quantify the detection versus false alarm rejection. Preprocessing and data conditioning, MF for abundance estimate, and MT for false-positive rejection are the three primary processes of the MTMF approach (Boardman *et al*., 2011). The conventional MF entails calculating a linear operator or projection vector that attempts to strike the best balance between two goals: target detection and background suppression. The intended MF output image, which is a linear combination of the input images bands, has numerous distinguishing characteristics, including a zero mean, minimal variation, and perfect target match pixels scored to unity (Boardman *et al*., 2011).

Hosseinjani and Tangestani, (2011) attempted to explain the importance of earth observation technology and a sort of digital earth processing in the exploration and appraisal of mineral resources. In the Sarduiyeh area, SE Kerman, Iran, the sub-pixel distribution and quantity of alteration minerals were mapped using linear spectral unmixing (LSU) and mixture tuned matched filtering (MTMF) techniques, the data of the Advanced Spaceborne Thermal Emission and Reflection Radiometer instrument’s visible-near infrared (VNIR) and short-wave infrared (SWIR) bands were compared to evaluate the efficiency of approaches. There are three types of alteration minerals identified by the authors: (1) pyrophyllite-alunite, (2) sericite-kaolinite, and chlorite-calcite-epidote. Several previously unreported changed areas were also discovered. To confirm the major mineral phases observed remotely, the researchers employed field observations and X-ray diffraction (XRD) examination of field samples. They discovered that the LSU and MTMF outcomes were nearly identical, with an overall accuracy of 82.9 and 90.24

percent, respectively. The conclusion is that LSU and MTMF are suiTable for sub-pixel mapping of alteration minerals, and the MTMF technique might be offered when the goal is to identify specific targets rather than all of the elements in the scene.

CHAPTER THREE

3 METHODOLOGY AND STUDY AREA

3.1 General description of the study area

3.1.1 Location and accessibility

The study area is found in Eastern Tigray, Northern Ethiopia at four different woredas which are located at about 57 km from Mekelle city. Geographically, it is found in 37-zone and bounded by UTM coordinates of 557000m to 578000mE, and 1525000m to 1546500mN longitude and latitude respectively with total areal coverage of about 509.6 sq km (Fig 3.1). It is accessed by the main asphalt road running from Mekelle to Adigrat. Besides the asphalt road, there are also gravel roads running from Negash to Wukro and to the other directions with alternative small trail routes that accessed the target area.

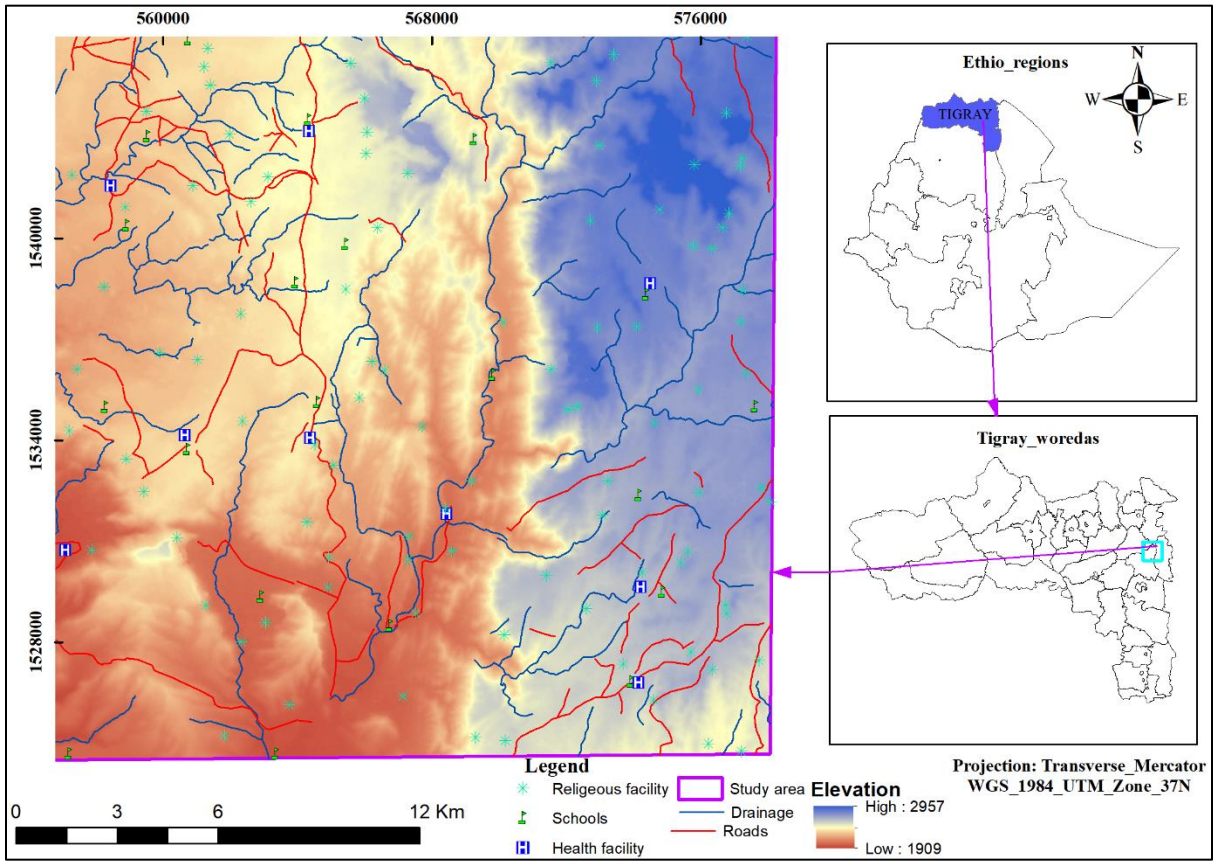

Figure:3. 1. Location and accessibility map of the study area.

3.1.2 Drainage patterns

The drainage pattern of the study area is characterized by trellis and dendritic drainage patterns. Most of the drainages were found along the river (streamflow) and these are used to understand the direction of groundwater flow. Most of the streams that are found in the study area are flowing in the western and southern parts. The collective drainage patterns are generally flowing in the southwestern direction. Negash area is characterized by dendritic to sub-parallel drainage patterns (Fig 3.2).

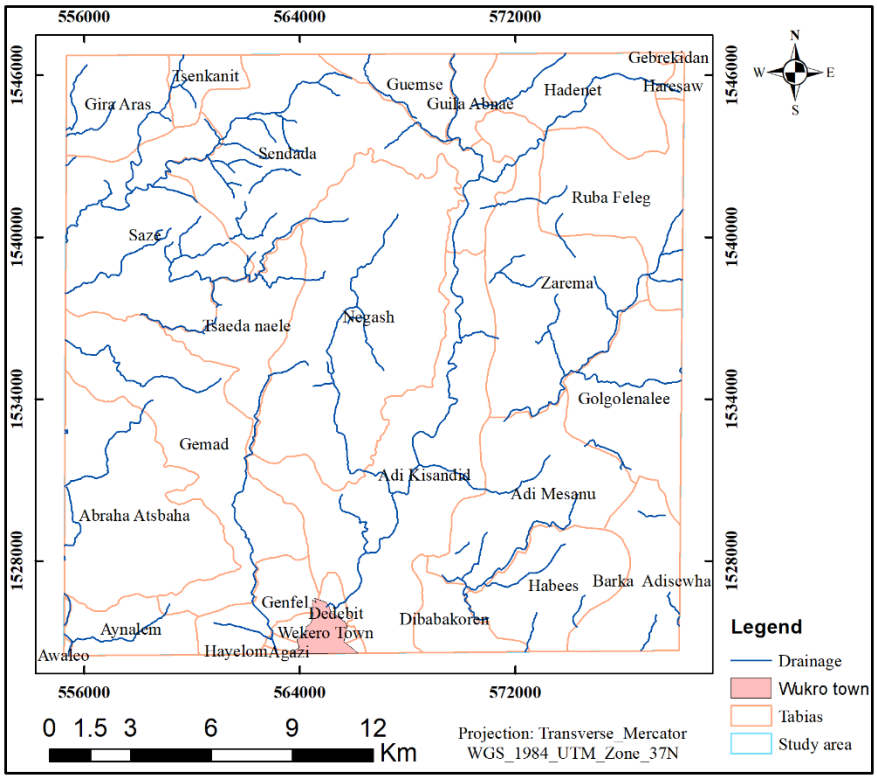

Figure:3. 2. Drainage map.

3.1.3 Physiographic features

Different topographic features, such as ridges, hills and flat surfaces, characterize the study area. The general topography of the study area is characterized by a gentle to a steep slope. The eastern part forms a synclinal fold due to deformation events. In general, the eastern, south-eastern and north-eastern of the study area has a steep slope, while some parts of north, south and north-western and south-western are gentle slopes. The minimum and maximum elevation of the area is 1950m and 2950 m above sea level respectively (Fig 3.3).

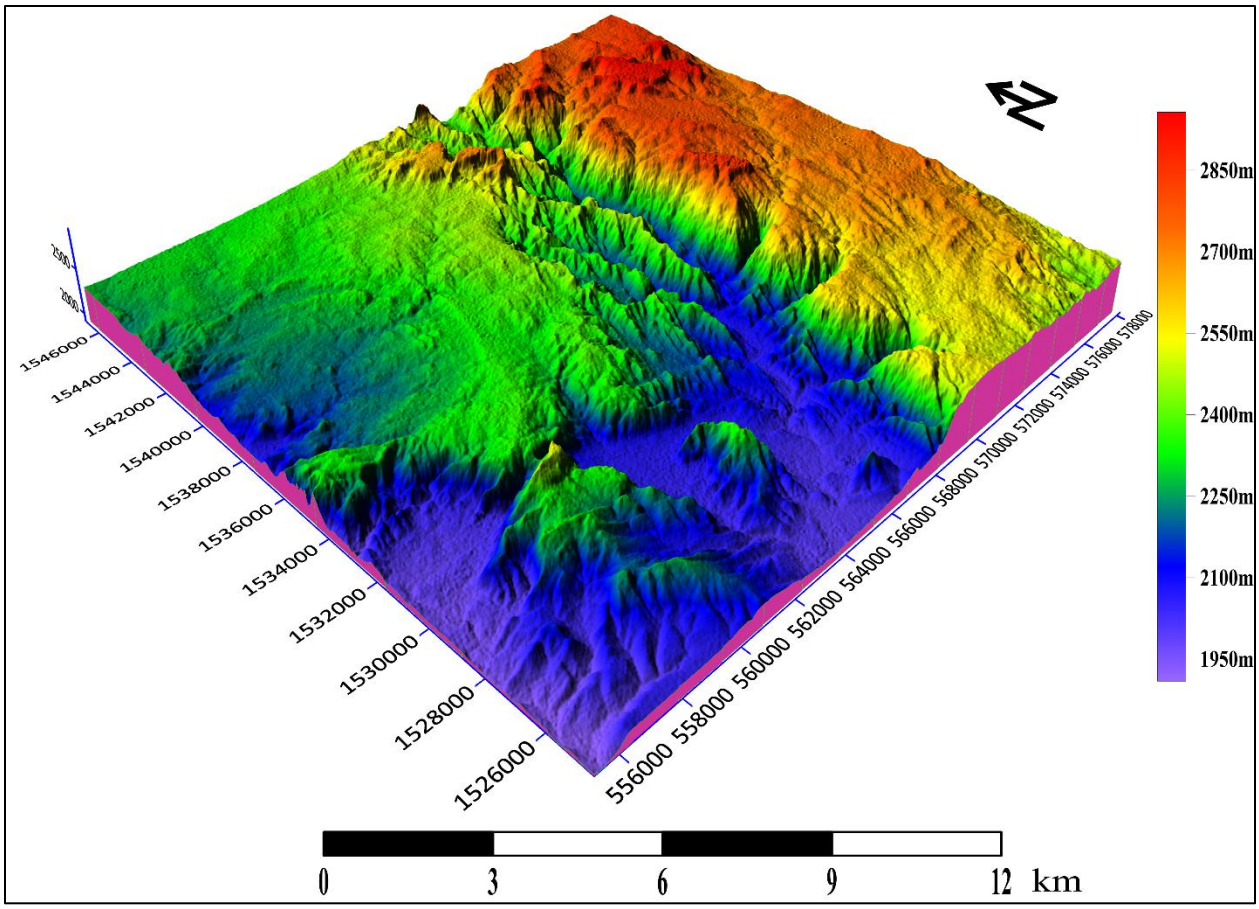

Figure:3. 3. Physiographic map.

3.1.4 Climatic condition and vegetation cover

Negash and its surrounding area are characterized by hot and semi-arid climatic conditions throughout the year. The rainfall pattern is seasonal mostly dominant between May and September. The average annual maximum and minimum precipitation is 1045.43 and 366.2 mm respectively (Fig 3.4) and also the average annual maximum and minimum temperature is about 28.82 ^{0}C and 12.31 ^{0}C respectively (Fig 3.5 and 3.6). Before graphs were prepared data gap was filled by Monte Carlo and Multiple Imputation technique in XLSTAT 2021.

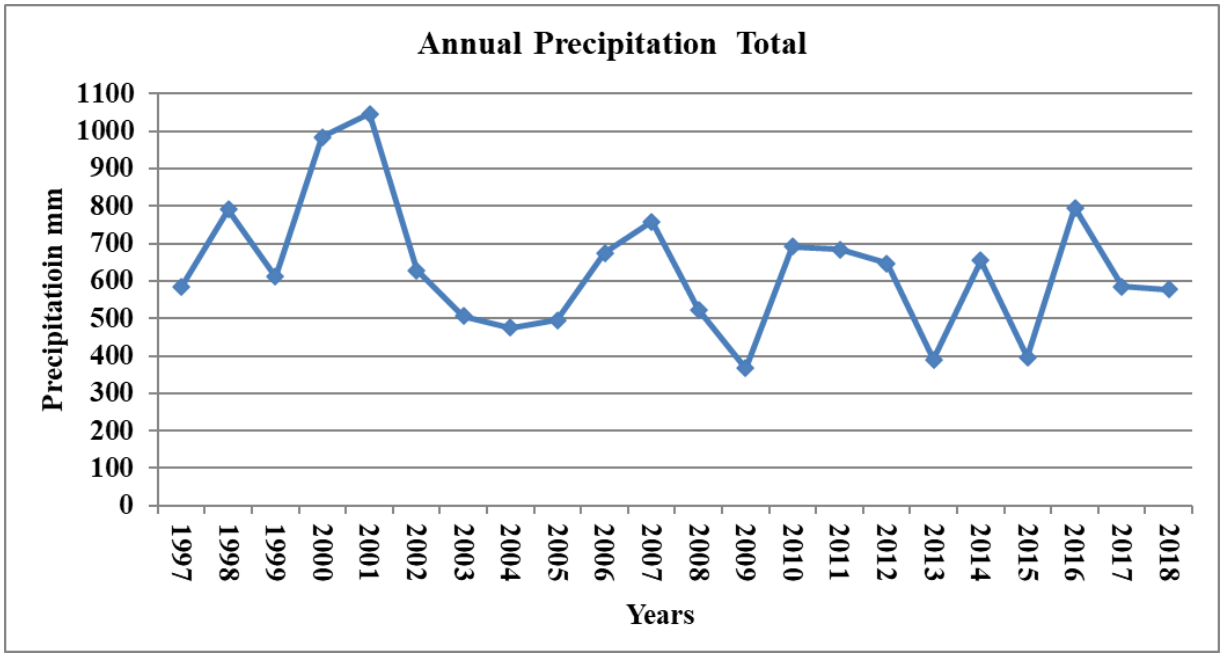

Figure:3. 4. Graph showing annual total precipitation of the study area.

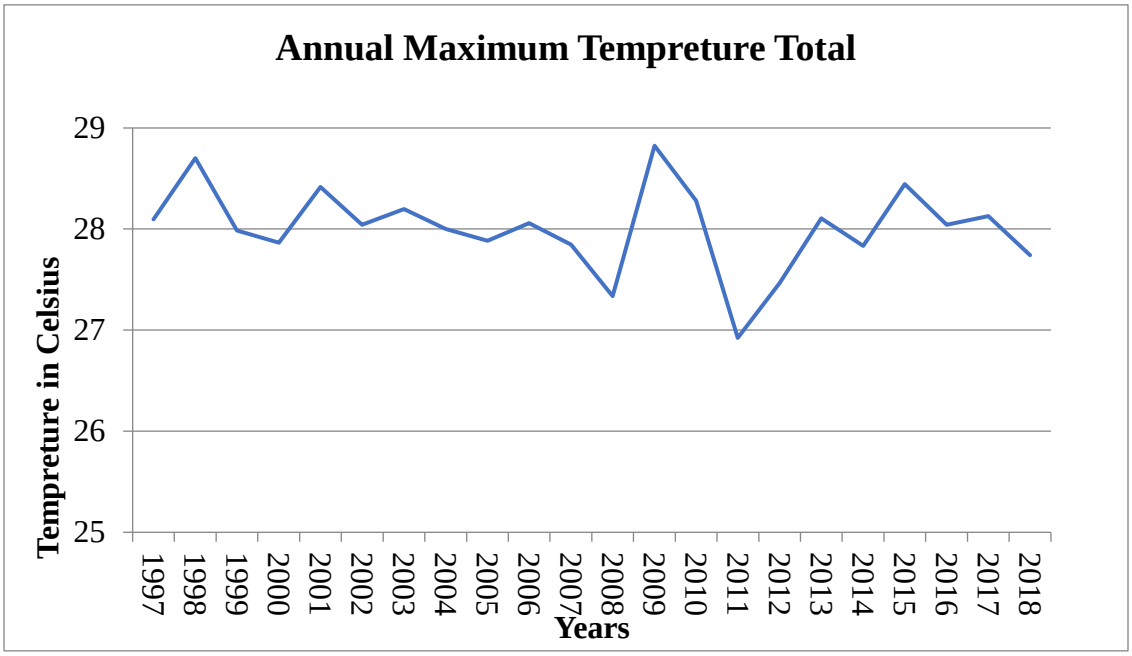

Figure:3. 5. Graph showing annual maximum temperature.

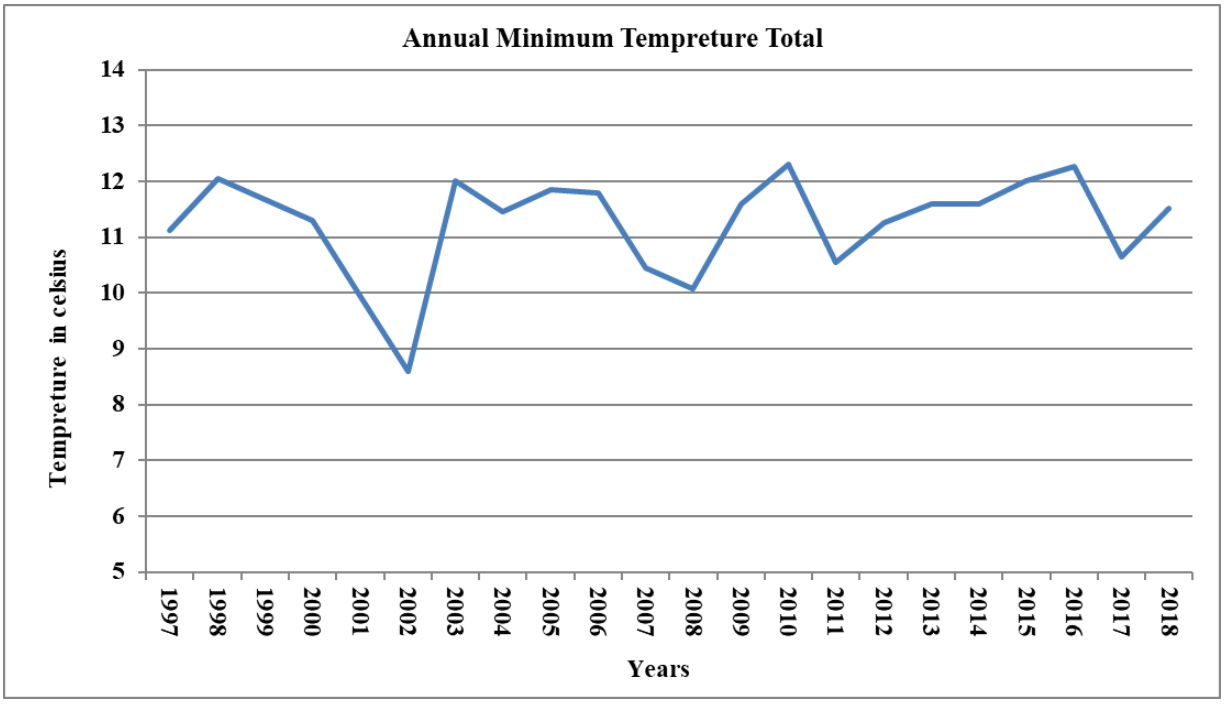

Figure:3. 6. Graph showing annual minimum temperature.

The area is sparsely vegetated, but the vegetation coverage of the western part is relatively denser than the other area. The vegetation types are olive, bushes, eucalyptus, cactus, etc.

3.1.5 Geology of Negash area

According to Solomon Gebresilassie *et al.*, (2012) the area forms part of Arabian Nubian Shield and consists of Neoproterozoic low-grade N-S to NE-SW trending basement rocks of Tsaliet Group (~860-750Ma) with metavolcanics, meta volcaniclastics and metasediments, and younger Tambien Group (~740 Ma) with metasediments, slate, phyllite, meta limestone and pebbly slate (diamictite). Apart from foliation, Tambien Group rocks show the development of synclinal structures (Negash syncline). These are intruded by post-tectonic granitoid (~600 Ma) and overlain unconformably by fluvial Paleozoic iron-rich Enticho Sandstone and Edaga Arbi tillite and by marine Mesozoic iron-rich Adigrat Sandstone, Antalo Limestone, Agula Shale and Amba Aradom Sandstone. Dolerite dikes have intruded during uplift and faulting during Cenozoic time. The Neoproterozoic assemblage of the Tigray region consists of two groups the oldest being the metavolcanic/meta-volcanoclastic unit (also called the Tsaliet Group), followed by phyllite, slate, and carbonate, which fall under the Tambien Group, and the syn- to post-tectonic plutonic units, granite to granodioritic composition (Asfawossen Asrat *et al.*, 2001; Mulugeta Alene *et al.*, 2006; Tarekegn Tadesse *et al.*, 2000). The Negash area includes (from bottom to top) Negash

Slate Dolomite and Slate, limestone (Negash Limestone), Slate/Pebbly slate (Diamictite Slate). The Negash Limestone's composition and grain size, together with only weak fabric development, suggest that it should be connected with the Mai Kenetal section's Upper Limestone, and we give isotope evidence to back this up (Mulugeta Alene *et al.*, 2006). Also, they grouped the two lowermost units of the Negash sequence as the Didikama Formation and the three top units as the Matheos Formation and described both formations as units younger than the Tambien Group. Tsaliet Metavolcanics covers the largest area followed by Meta-greywacke 35.19% and 15.28 % respectively (Fig 3.7, Fig 3.8 and Table 3.1).

Table 3: 1. Statistics of the geology of the study area.

Lithology	Area	Percentage
Enticho sandstone	49.75	9.81
Intrusive	24.29	4.79
Limestone-marl	5.96	1.17
Lower sandstone	23.47	4.63
Meta-conglomerate	61.72	12.17
Meta-greywacke	77.53	15.28
Meta-limestone	11.61	2.29
Meta-sediment	68.30	13.46
Meta-volcanic	178.54	35.19
Transition	6.15	1.21

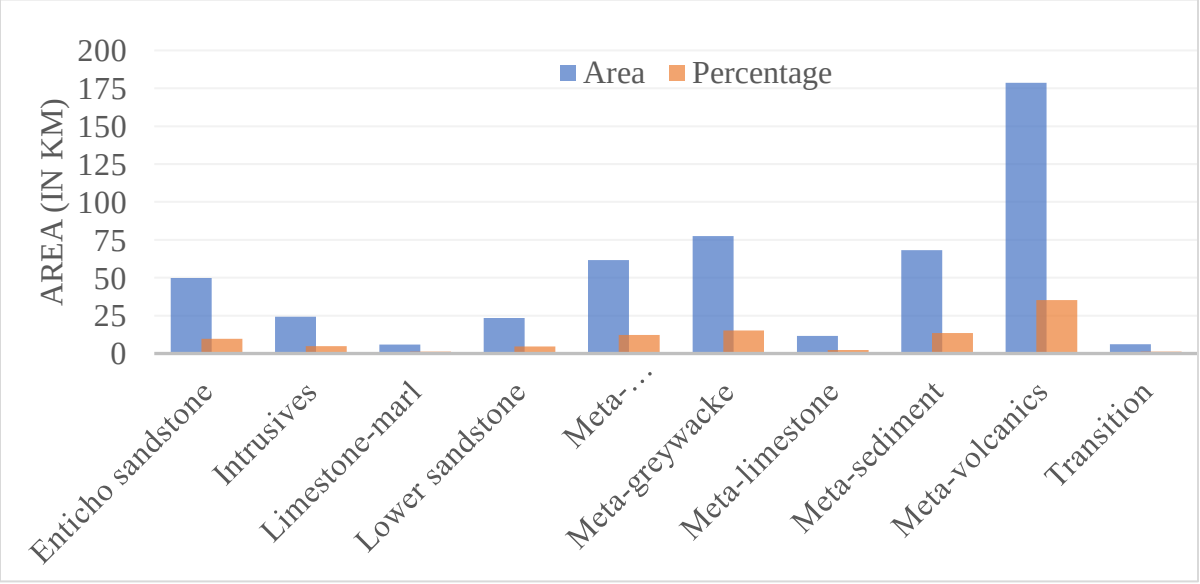

Figure:3. 7. Graph showing area and percentage of lithologies.

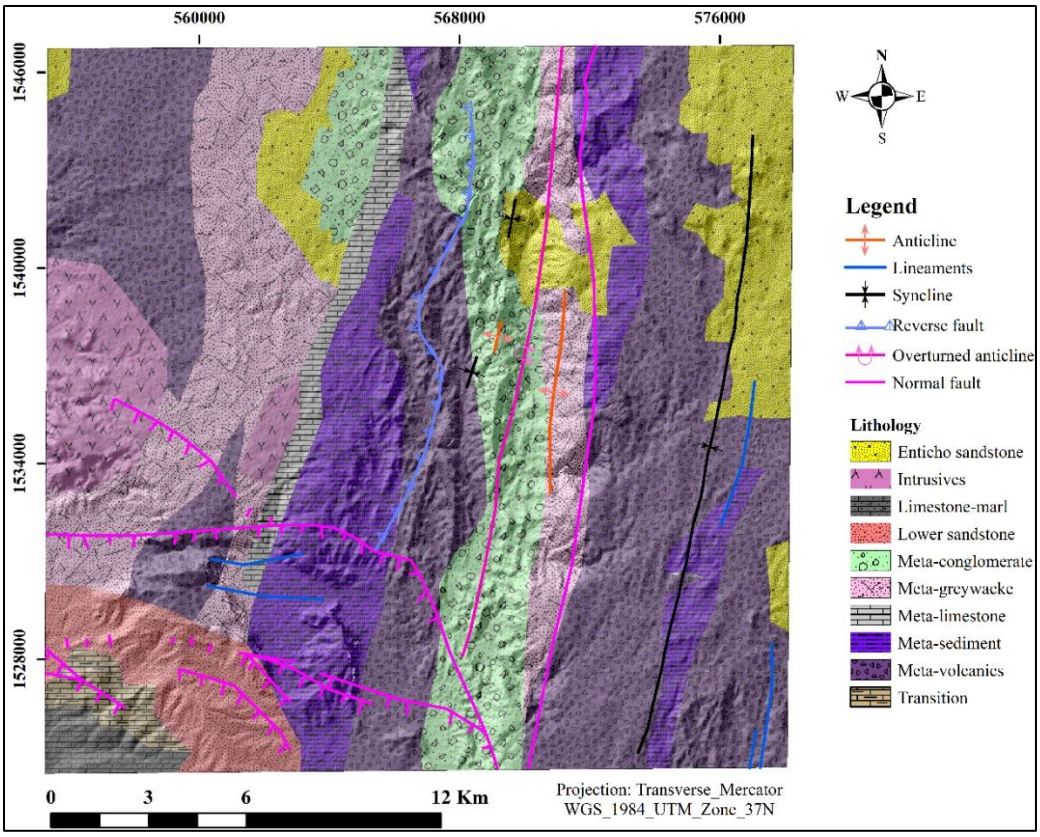

Figure:3. 8. Geological map of Negash area (Source: Tesfamichael Gebreyohannes et al., (2010)).

3.2 Data description

The ASTER (Advanced Spaceborne Thermal Emission and Reflection Radiometer) and Landsat 8 OLI cloud-free image data were used, covering the iron ore deposits of the Negash area. In this study, VNIR and SWIR bands were used to decipher the spatial distribution of iron oxide at the studied sites since iron oxides have absorption features in these bands. Primary (ASTER, Landsat 8 OLI and DEM) and secondary data which includes a geological map of the Wukro sheet, topo-sheet of Wukro area and shapefiles of different objects were used (Table 3.2). Resampled 12.5 m DEM was used to prepare a hill shade map.

Table 3: 2. Primary and secondary data used.

Data	Path	Raw	Date of acquisition	Source	Data type
ASTER L1T	-	-	December 10, 2005	http://earthexplorer.usgs.gov/	Raster
Landsat 8 OLI L1T	169	050	Jan 28, 2020	https://glovis.usgs.gov/	Raster
DEM	-	-	Feb 22, 2011	https://search.asf.alaska.edu/#/	Raster

Secondary data	Source	Purpose	Data type	Scale
Geological map of Mekelle sheet	GSE (geological survey of Ethiopia)	For geological map preparation	Raster	1/250,000
Topo sheet Wukro 1339 B	GII (geospatial information institute)	For digitizing study area	Raster	1/50,000
Metrological data	EMA (Ethiopia metrological agency)	For annual average precipitation and T calculation.	Tabular	-
Shapefiles	CSAE (a central statistical agency of Ethiopia)	For different map works	Vector	-

3.2.1 ASTER data

The ASTER instrument was launched on the Terra satellite in December 1999 as part of the NASA Earth Observing System. It is one of five sensors on the Terra satellite and designed to acquire repetitive, high spatial resolution, multi-spectral data from the VNIR to the TIR region, the first time for any commercial satellite. It comprises three separate subsystems operating with three channels in the VNIR region (with 15 m pixel resolution), six channels in the SWIR region (with 30 m pixel resolution), and five channels in the TIR region (with 90 m pixel resolution) (Table 3.3).

Table 3: 3. ASTER bands and their wavelength.

Band	Reflected Range (μm)	Spatial Resolution (m)	Band Explanation/Uses
1	0.52 - 0.60	15 m	Visible and Near-Infrared
2	0.63 - 0.69	15 m	Visible and Near-Infrared
3N	0.78 - 0.86	15 m	Visible and Near-Infrared
3B	0.78 - 0.86	15 m	Visible and Near-Infrared
4	1.600 - 1.700	30 m	Shortwave Infrared
5	2.145 - 2.185	30 m	Shortwave Infrared
6	2.185 - 2.225	30 m	Shortwave Infrared
7	2.235 - 2.285	30 m	Shortwave Infrared
8	2.295 - 2.365	30 m	Shortwave Infrared
9	2.360 - 2.430	30 m	Shortwave Infrared
10	8.125 - 8.475	90 m	Thermal Infrared
11	8.475 - 8.825	90 m	Thermal Infrared
12	8.925 - 9.275	90 m	Thermal Infrared
13	10.25 - 10.95	90 m	Thermal Infrared
14	10.95 - 11.65	90 m	Thermal Infrared

Source: https://lpdaac.usgs.gov/data/get-started-data/collection-overview/missions/aster-overview/

3.2.2 Landsat 8 OLI

Landsat 8 Operational Land Imager and Thermal Infrared Sensor (TIRS) images consist of nine spectral bands with a spatial resolution of 30 meters for bands 1 to 7 and 9. New band 1(ultra-blue) is useful for coastal and aerosol studies. New band 9 is useful for cirrus cloud detection. The resolution for band 8 (panchromatic) is 15 meters. Thermal bands 10 and 11 are useful in providing more accurate surface temperatures and are collected at 100 meters(Table 3.4). The approximate scene size is 170 km north-south by 183 km east-west (106 mi by 114mi).

Table 3: 4. Landsat 8OLI bands and their wavelength.

Bands	Wavelength (micrometers)	Resolution (meters)
Band 1 - Coastal aerosol	0.43-0.45	30
Band 2 – Blue	0.45-0.51	30
Band 3 – Green	0.53-0.59	30
Band 4 – Red	0.64-0.67	30
Band 5 - Near Infrared	0.85-0.88	30
Band 6 - SWIR 1	1.57-1.65	30
Band 7 - SWIR 2	2.11-2.29	30
Band 8 – Panchromatic	0.50-0.68	15
Band 9 – Cirrus	1.36-1.38	30
Band 10 - Thermal Infrared (TIRS) 1	10.6-11.19	100
Band 11 - Thermal Infrared (TIRS) 2	11.50-12.51	100

Source:https://www.usgs.gov/faqs/what-are-band-designations-landsat-satellites?qt-news_science_products=0#qt-news_science_products

3.3 Methods

3.3.1 Data preprocessing

Preprocessing applied to ASTER imagery consisted of the following steps: conversion from the DN value to radiance using radiometric calibration, layer stacking, conversion to BIL format (since FLAASH accepts BIL format) and then atmospheric correction using the Fast Line-of-sight Atmospheric Analysis of Spectral Hypercubes (FLAASH) to determine surface reflectance values by removing atmospheric effects from satellite images. On the other hand, for Landsat-8/OLI DN value to radiance using radiometric calibration, conversion to BIL format and then FLAASH atmospheric correction was applied. In FLAASH atmospheric tropical atmospheric model and tropospheric aerosol model were used for both images. FLAASH was used because it improves the accuracy of the atmospheric correction by detecting and compensating for sensor-introduced artifacts such as optical smiles and inaccurate spectral calibration (Bangira et al., 2017). Then followed by band math to scale reflectance between 0 and 1 because FLAASH produces negative minimums and multiplies reflectance by 10,000. After that, the image was subsetted using the study area. Panchromatic and thermal infrared (TIR) bands (from both

images), as well as bands 1,8 and 9 of the OLI, were excluded from the analysis. Bands 1 and 9 of the OLI sensors were designed for coastal studies and cirrus cloud detection, respectively (Masoumi et al., 2017).

Finally, NDVI was calculated for both images because it only needs the spectral measurements from the satellite, i.e. we only need the image pixels and can compensate for changing illumination conditions, surface slope, and viewing angle. Also, this tool is very useful in assessing vegetation stress differences that could be due to the underlying rock formations or water availability (Gopinathan et al., 2020). Areas greater than 0.4 for ASTER and 0.3 (Landsat 8 OLI) were masked as vegetation and ignored from further analysis (Tompolidi *et al.*, 2020). NDVI was calculated from both images using Eq (1)(Gandhi *et al.*, 2015).

$$\text{NDVI} = NIR - Red/NIR + red \quad \ldots\ldots\ldots\ldots\ldots\ldots\ldots\ldots\ldots\ldots\ldots\ldots\ldots\ldots \quad (1)$$

where NIR= band 3 and 5 and red = band 2 and 4, for ASTER and Landsat 8 OLI respectively. The overall workflow of the research is seen in Fig 3.9.

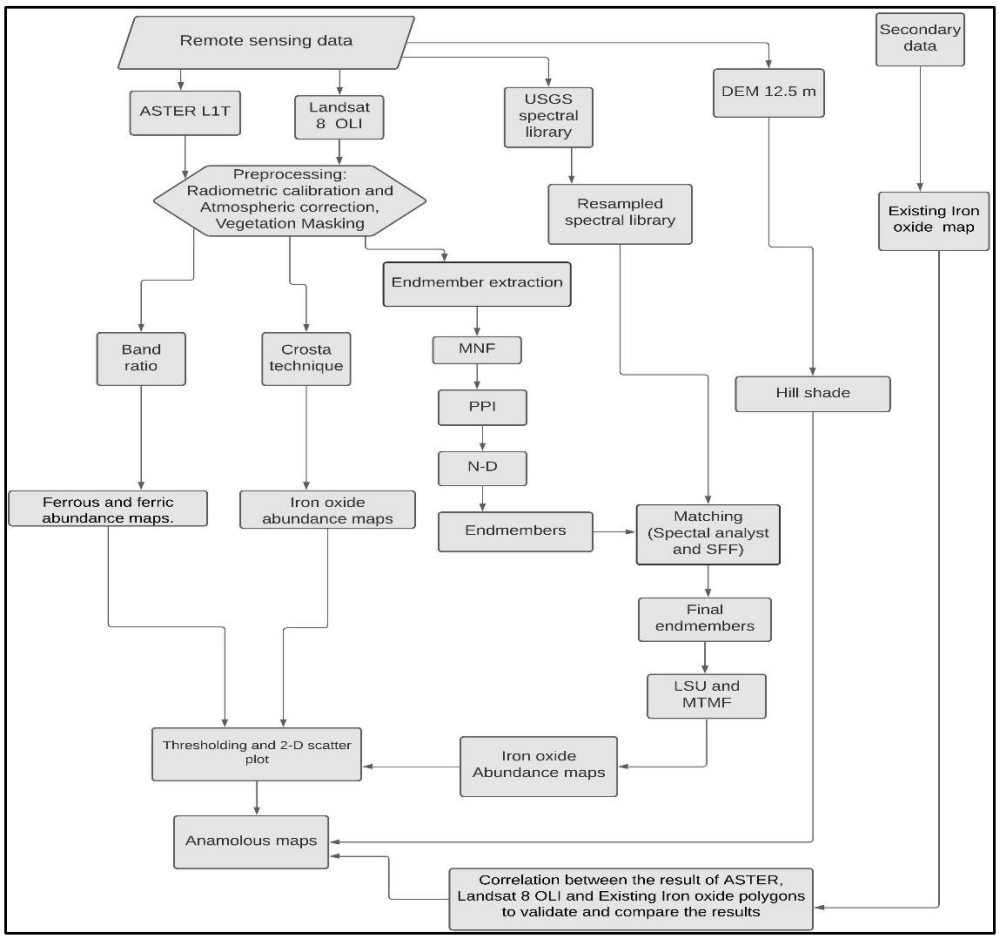

Figure:3. 9. Methodology flow chart.

3.3.2 Endmember extraction methods

Endmembers are spectrally pure, unique materials that occur in the scene. Endmember extraction is an important process in the creation of useful material abundance maps. Although there are different endmember extraction methods, image spectra which were extracted through a 'spectral endmember selection' procedure, including minimum noise fraction (MNF), pixel purity index (PPI) (Boardman, 1993; Boardman *et al.*, 1995; Hosseinjani and Tangestani, 2011) and N-dimensional visualization (Boardman *et al.*, 1995; Hosseinjani and Tangestani, 2011) were used in this research. To run the steps sequentially an Automated spectral hourglass was used and image endmembers were generated. Because image endmembers are obtained at the same spatial scale as the image to be analyzed, whereas reference endmembers are usually collected under different atmospheric conditions than airborne or satellite imagery, and at a different spatial scale, due to their proximity to objects (Adams and composition, 1993). Furthermore, collecting adequate endmember spectra for all-important ground components in the field or laboratory is time-consuming (Shi *et al.*, 2016). Therefore, image endmembers were generated for this study.

3.3.2.1. Pixel purity index (PPI)

The PPI image shows the locations of the purest pixels in the image. By definition, a pure pixel contains only one spectrally unique material. First, minimum noise fraction was applied for ASTER 9 bands and 6 Landsat 8 OLI bands to reduce the dimensionality (i.e., the number of bands) in the data, and compress as much of the information in the original bands into fewer bands. All 9 ASTER and 6 Landsat 8 OLI were used for further analysis since the eigenvalues are >1(Hosseinjani and Tangestani, 2011). The Pixel Purity Index (PPI) was run on the MNF data to aid in deriving endmembers from the image and spatial data reduction. The number of iteration and thresholds used were 10,000 and 2.5 for both images (Hosseinjani and Tangestani, 2011).

3.3.2.2. N-Dimensional visualizer

The N-dimensional Visualizer is an interactive tool that allows the user to select endmembers in n-space. Pixels from the spectral bands are loaded into an n-dimensional scatter plot and rotated on the visualization tool until points or extremities on the scatter plot are exposed. The ENVI N-dimensional Visualizer was loaded with the top-scoring pixels from the PPI result and 10 and 7 of endmembers retrieved from N-D Visualizer automatically for ASTER and Landsat 8 OLI. These projections are marked using a region of interest (ROI) tool and are repeatedly rotated in lesser dimensions to determine if their signatures are unique. Then using the Spectral analyst the known reference spectral (USGS spectral library found in ENVI resource) was matched with

unknown spectral derived from the images and weights were given using SFF (Hosseinjani and Tangestani, 2011). Here SFF values > 0.77 were taken as endmember for ASTER image and 1 for Landsat 8 OLI which is above 0.5 (Kalinowski. and Oliver, 2004). These endmembers are then used for subsequent classification and other processing (Kumar *et al.*, 2008).

3.3.2.3. Spectral feature fitting

In this study spectral feature fitting (SFF) was used to compare the fit of image spectra to reference spectra using a least-squares technique to give rank. SFF was applied because it is an approach based on absorption features. After the continuum is eliminated from both datasets, the reference spectra (USGS spectral library) are resampled and scaled to match the images spectra and finally, the score was given by SFF to validate the image spectra.

3.3.3 Abundance mapping techniques

Abundance maps are maps that show the abundance of the mineral, which is obtained using pixel or sub-pixel level mapping techniques.

3.3.3.1 Band ratio

The band ratio is a simple and effective method for identifying and demarcating iron ore mineral occurrences (Gopinathan *et al.*, 2020). This process entails the split of two bands, with the numerator being the band with the highest reflectance features of the provided material, and the denominator being the band with the highest absorption features of the same material. By defining the slope of the spectral curve between two bands, rationing can be viewed as a means of emphasizing tiny differences between materials. The resulting gray-scale band ratio image isn't a direct measurement of the substance's contents; rather, it denotes the area where the presence of the provided item is most likely. The combination of three-band ratio images as red-green-blue (RGB) images is useful for the interpretation of the result. For instance, iron ore absorbs in the 0.85–0.9 μm region of electromagnetic radiation (EMR). Band ratio images are used to remove the effect of uneven illumination caused by the topography with an assumption that the ratio of two bands in the same rock type will be the same, no matter in which way the slope faces (Gopinathan *et al.*, 2020).

Band ratios 6/4 (ferrous iron oxides), 4/3 (ferric iron oxides) (Cardoso-Fernandes *et al.*, 2019) and 5/4 (vegetation) of Landsat 8 OLI (Ducart *et al.*, 2016) and band 2/band 1 (for Fe^{3+}), 4/5 (Laterite) and band 5/band 3 + band 1/band 2 (for Fe^{2+}) of ASTER (Gopinathan *et al.*, 2020) were used in this study. The essential difference between ferrous mineral abundance and ferric

mineral abundance is the Fe^{2+} and Fe^{3+} states. Iron oxide abundances include both ferrous and ferric irons.

3.3.3.2 Feature-oriented principal component selection

Feature-oriented principal component selection (FPCS) or Crosta Technique is a method based on principal component analysis, according to (Traore *et al.*, 2019). The covariance matrix obtained from the input multi-spectral data is typically used to calculate principal components, and the related eigenmatrices are also determined. In multispectral data, different bands are frequently highly correlated and hence contain identical information. Image processing techniques can be used to reduce data redundancy and band correlation. The primary transform is an example of such a transformation. Rather than trying to employ all bands, the interpretation and analysis of these three bands of data can be done more readily and efficiently by merging them visually or digitally. Only the bands of the image that have a reflection and an absorption are used in feature-oriented principal component selection. FOPCS is based on determining which of the main component images will concentrate the information directly relevant to the hypothesized spectral signatures of specific targets by examining PCA eigenvector loadings. The ability to forecast whether the target surface type is highlighted by dark or bright pixels in the matching principal component image is a key feature of this method. In this investigation, ASTER bands 1, 2, 3 and 4 (Traore *et al*., 2019) and Landsat 8 OLI bands 2, 4, 5 and 6 (Osinowo *et al*, 2021) were employed for iron oxide mapping.

3.3.3.3 Linear spectral unmixing

This method was used to determine the abundance of the minerals in each pixel of an image (Sentayehu Berihun, 2018). The reflectance at each pixel of the image is assumed to be a linear combination of the reflectance of each material (endmember) present within the pixel. However, there are certain limitations in applying the linear spectral unmixing technique. The number of endmembers must be less than the number of spectral bands and all of the endmembers in the image must be used for an efficient mapping result (Kumar *et al.*, 2008; Sentayehu Berihun, 2018). The results of spectral unmixing are highly dependent on the input of endmembers and changing endmembers also changes the final results (Gopinathan *et al.*, 2020). In this LSU was applied on the MNF image of the ASTER image using different endmembers and the target area was detected using thresholding.

3.3.3.4. Mixture tuned matched filtering

The partial unmixing classification algorithm Mixture Tuned Matched Filtering (MTMF) is a relatively new image processing technology that has proven to be an effective target recognition tool (Mundt *et al.*, 2007). (Boardman,1998) developed "MTMF" to tackle the "selectivity" problem inherent in existing traditional MF approaches (also known as CEM and/or orthogonal subspace projection) (Boardman *et al.*, 2011). MTMF improves performance over MF alone by combining components of hyperdimensional convex geometry spectral unmixing and statistical matched filter target detection. It maintains the MF's ease of calculation while allowing for increased target selectivity, excelling at the accurate mapping of extremely small subpixel targets with low false alarm rates. When utilized on the same input data as other methods that previously had a high number of false alarms, MTMF frequently delivers low false alarm rates. This increase in performance demonstrates the effectiveness of the approach's mixture tuning (MT) component. More challenging applications are needed to fully quantify the detection versus false alarm rejection. Preprocessing and data conditioning, MF for abundance estimate, and MT for false-positive rejection are the three basic processes in the MTMF approach (Boardman *et al.*, 2011). Here MTMF was applied for iron oxide target detection for both images using generated endmembers.

3.3.4 Anomalous (potential) area detecting techniques

An anomaly is a pattern in the image data that does not follow the expected behavior, also referred to as outliers, exceptions, peculiarities (Chandola *et al*., 2009: Zhou *et al*., 2016). To acquire quantitative information about the areas of mineral abundances, thresholding (or density slicing) is applied to the transformed data to separate the high potential pixels (anomalous areas) and exclude iron oxide lower concentrations similarly applied by (Wambo *et al*., 2020). A threshold was applied on band ratios, selected PCA and LSU which is generated using the mean and standard deviation. The standard deviation used varies with the confidence level used to calculate the anomaly which is applied by San *et al*., (2004). Before calculating the threshold, the results were stretched to 0- 255 and mean and standard deviation was taken from the basic statistics. For MTMF results 2D scatter plot was used to identify the pixels with low infeasibilities and high MF scores. MF results in the x-axis and infeasibility in the y-axis were used. Pixels lying in the bottom right corner were selected as potential areas since they have high MF and low infeasibility values similarly used by Calin *et al.*, (2015). The threshold is calculated using Eq. (2).

$$Threshold = X + SD \quad \text{..... (2)}$$

Where X is the mean and SD standard deviation. If confidence level = 92%, 2SD if 95% and 3SD if 98%. Where X = mean and SD = standard deviation

3.3.5 Correlating, comparing and validating techniques

To correlate the results obtained from remote sensing analysis Pearson correlation coefficient was used. To perform the operation above 1000 random points were generated using 50 rows and 50 columns in ArcGIS, then correlation was done in XLSTAT 2020. The Pearson correlation coefficient results were interpreted as strong correlation values ranging from ±0.50 to ± 1, a medium correlation is defined as ± 0.30 to ± 0.49, and a weak correlation is defined as one with a value of less than ± 0.30 (Neway Kifle and Binyam Tesfaw, 2021).

Validation of accuracy is a process that involves evaluating the accuracy of a product and becomes an integral part of any remotely sensed data-derived map. It's critical to know the map's accuracy before making any decisions based on it. The most frequent metric of map accuracy is positional accuracy, which is a measure of how closely the imagery matches the ground. In other words, positional accuracy refers to the precision with which a point in imaging is located with its physical location on the ground (Congalton, 2007). Although there are different accuracy assessment techniques, in this study visual interpretation, and existing iron oxide maps of the study area (Appendix 4) were digitized into polygons and overlain to the mapped results to check the positional accuracy which was similarly applied by Foody, (2002). Results of ASTER and Landsat 8 OLI analysis were compared with the iron oxide existing polygons to check the performance of the sensor.

3.4 Softwares

Table 3: 5. Softwares used.

Softwares used	Purpose
ArcGIS 10.6.1	Layout preparation
ENVI 5.3	Data analysis
Global Mapper 20	To export vector grid
Surfer 16	Physiographic map preparation
XLSTAT 2021	For correlation calculation and precipitation and temperature data gap filling.

CHAPTER FOUR

4 RESULTS

4.1 Preprocessing results

Table 4.1 shows the mean radiance and reflectance value of each band used for both Landsat 8 OLI and ASTER.

Table 4: 1. Mean of the preprocessed images of both images.

	ASTER		Landsat 8 OLI	
Bands	Reflectance (mean)	Radiance (mean) (W/ (m2. sr)	Reflectance (mean)	Radiance (mean) (W/ (m2. sr)
Band 1	0.14	4.32	0.05	4.39
Band 2	0.18	4.36	0.06	4.22
Band 3	0.26	4.17	0.12	4.18
Band 4	0.32	1.07	0.16	4.24
Band 5	0.24	0.30	0.26	3.98
Band 6	0.24	0.28	0.31	1.14
Band 7	0.24	0.24		
Band 8	0.20	0.17		
Band 9	0.18	0.12		

4.1.1 NDVI and vegetation masked maps

The NDVI image of the study is in the range of – 0.08 to 0.76 derived from ASTER (Fig 4.1) and -0.21 to 0.51 derived from Landsat 8 OLI (Fig 4.2). The green portion shows the highly vegetated zone. In the study site, NDVI maps (Fig 4.1 and 4.2) areas of excess vegetation seen along stream beds and valleys are depicted as green regions, while the less vegetated areas as seen as moderately yellow regions, areas with the shadow and bare land are seen as red patches. Since the NDVI values contain values that can affect the mapping of iron oxides. After vegetation masking, only the iron ore bands and country-rock are visible for interpretation and dark represent masked areas (Appendix 1 and 2).

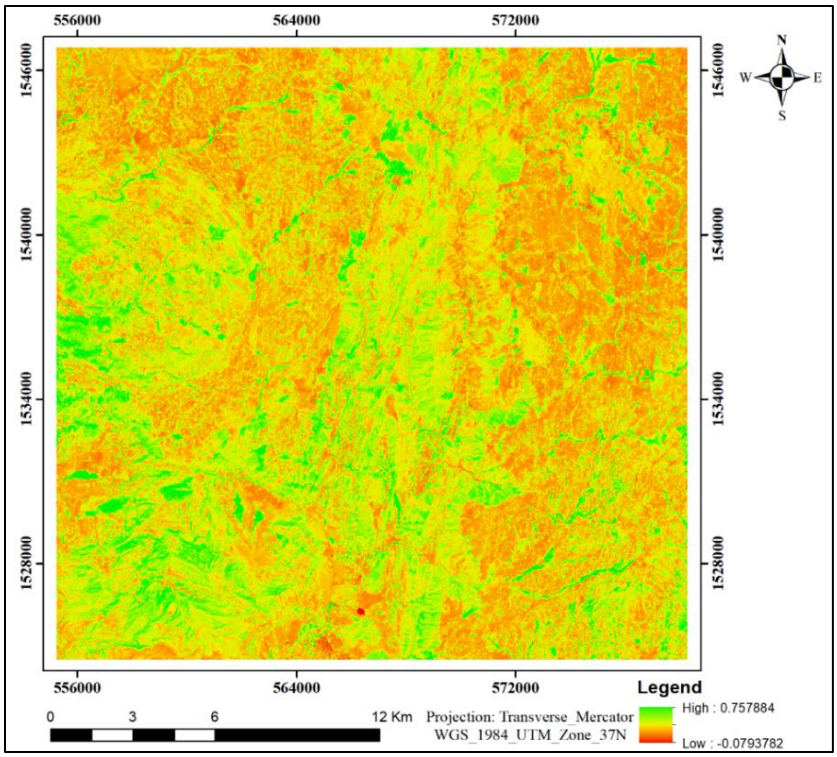

Figure 4. 1. NDVI map generated from ASTER.

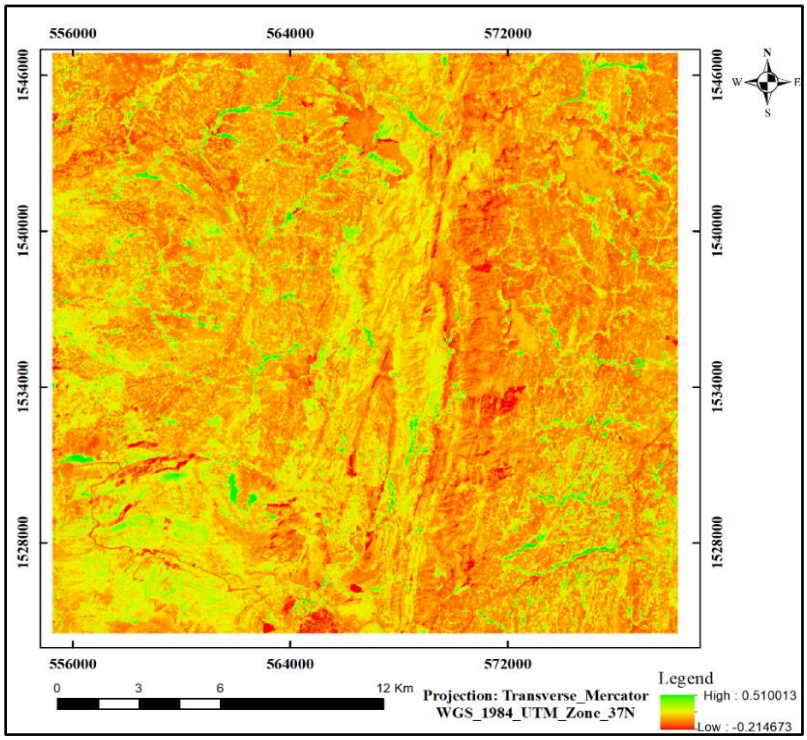

Figure 4. 2. NDVI maps derived from Landsat 8 OLI.

4.2 Ratio maps

4.2.1 Ferrous iron maps

The ferrous iron map is used to highlight the ferrous minerals mainly ores of iron in the map. The value above the threshold was overlain on the hill shade images. The result shows that in the ferrous generated from ASTER the ore is high in the Saze area and west of Tsenkanet (Fig 4.3). Whereas in Landsat 8 OLI the targets are in the Abrha-we-Atsbha area (Fig 4.4). The anomalous area covered by this technique is 56.8 and 13.75 sq km for ASTER and Landsat 8 OLI derived maps respectively. The areas were identified using 220 threshold values and 92% confidence level for ASTER derived and 197.2 and 95% for Landsat 8 OLI (Table 4.2).

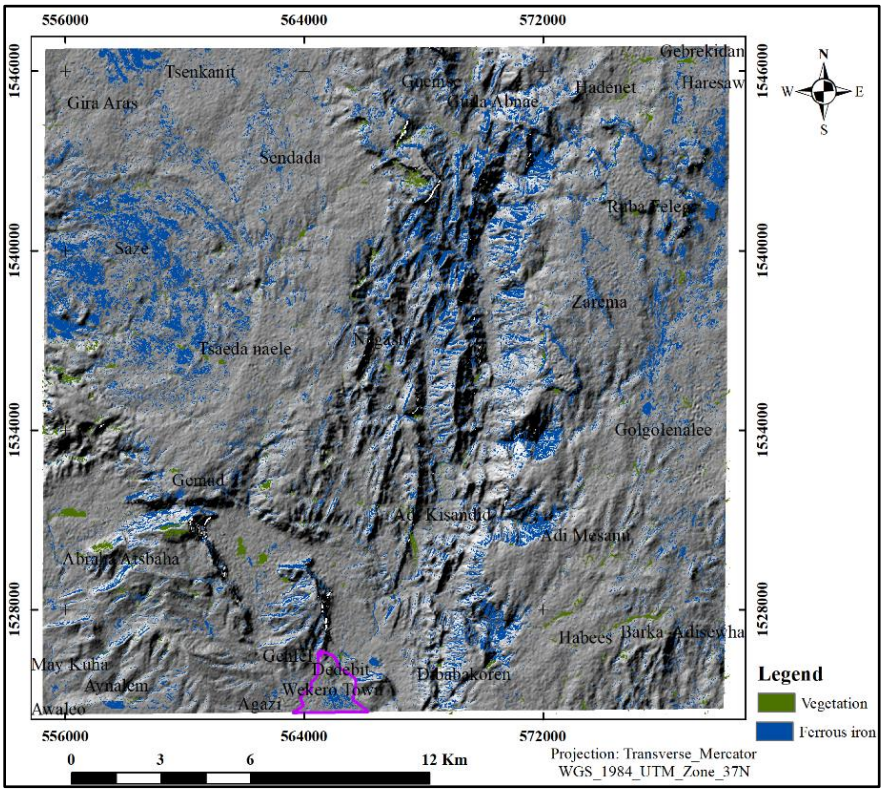

Figure 4. 3. Ferrous iron anomaly map generated from ASTER.

Table 4: 2. Threshold, confidence level and area mapped using all techniques.

Sensor	Technique	Used equation	Confidence level	Threshold used	Area mapped (in km^2)
ASTER	Band 2/1	X+SD	92%	222.8	62.1
	Band 5/3+1/2	X +SD	92%	220	56.8
	Band 4/5	X +SD	92%	210	57.8
	Selective PCA	X +2SD	95%	210.5	34.79
	Unmixing (goethite)	X+SD	92%	197	8.4
	Unmixing (hematite)	X+3SD	98%	185	26.5
	Goethite MF				16.4
	Hematite MF				52
Landsat 8 OLI	Band 6/4	X+2SD	95%	197.2	13.75
	Band 4/3	X+2SD	95%	188	13.2
	Selective PCA	X+2SD	95%	214.2	32.5
	MF (goethite)				28.4
	MF (hematite)				14.8

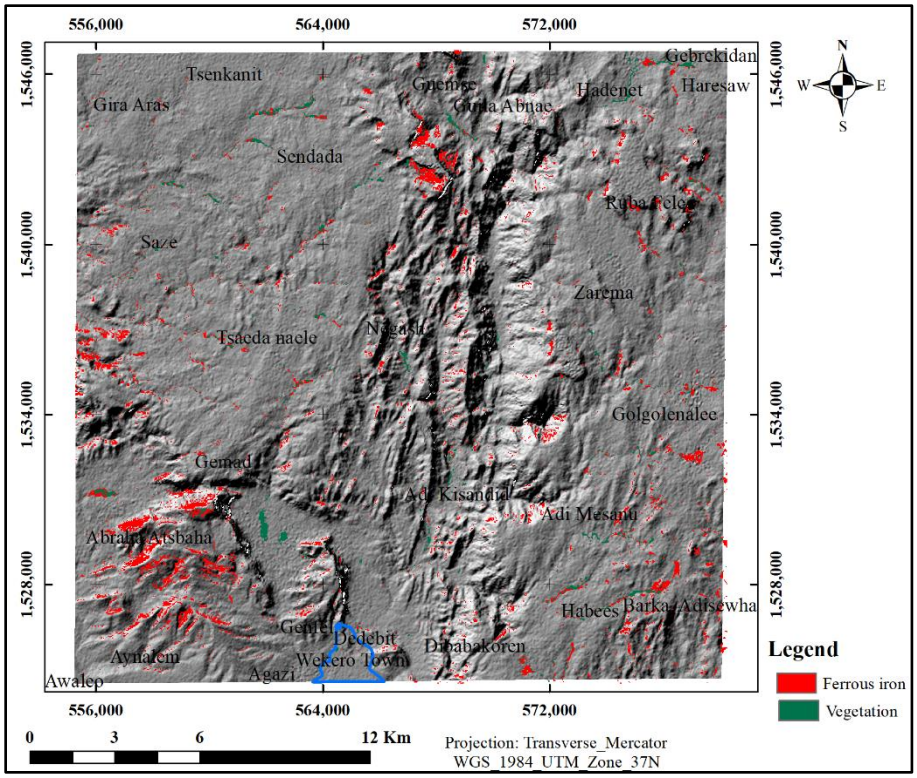

Figure 4. 4. Ferrous iron anomaly map generated from Landsat 8 OLI.

4.2.2 Ferric iron maps

The ferric iron oxide abundance map has been generated to highlight the iron oxide minerals. Bands 2 and 4 are reflective and bands 1and 3 are absorptive for ASTER and Landsat 8 OLI respectively. In Fig 4.5 below the ferric iron is dominated in the north around Sendeda and Graaras and southwest around Abrha we Atsbha part of the study area. On the other hand, in Fig 4.6 the target is found around Wukro town and other localities such as Abraha we Atsbha, Zarema and Graaras. The area mapped using threshold values of 222.8 with 92 % confidence level and 188 with 95% confidence level are 62.1 and 13.2 sq km respectively for ASTER and Landsat 8 OLI (Table 4.2).

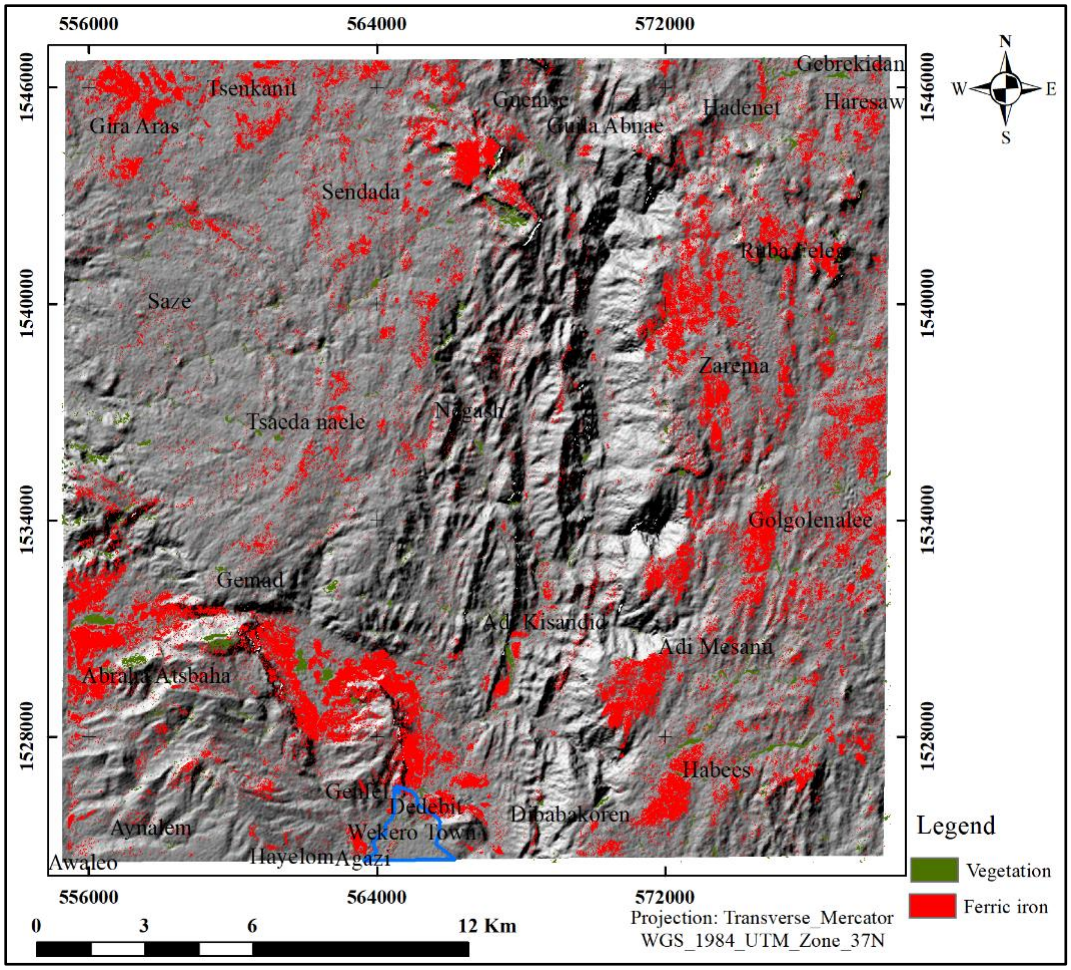

Figure 4. 5. Ferric iron anomaly map generated from ASTER.

4.2.3 Laterite distribution maps

A laterite distribution map has been generated for this study using ASTER. Band 5 is absorptive and band 4 is reflective. Values greater than 210 with a 92% confidence level were taken to map the target area (Table 4.2). From Fig 4.7 below the distribution is dominated in the southwest and southeast. The area covered by the anomaly is 57.8 (Table 4.2).

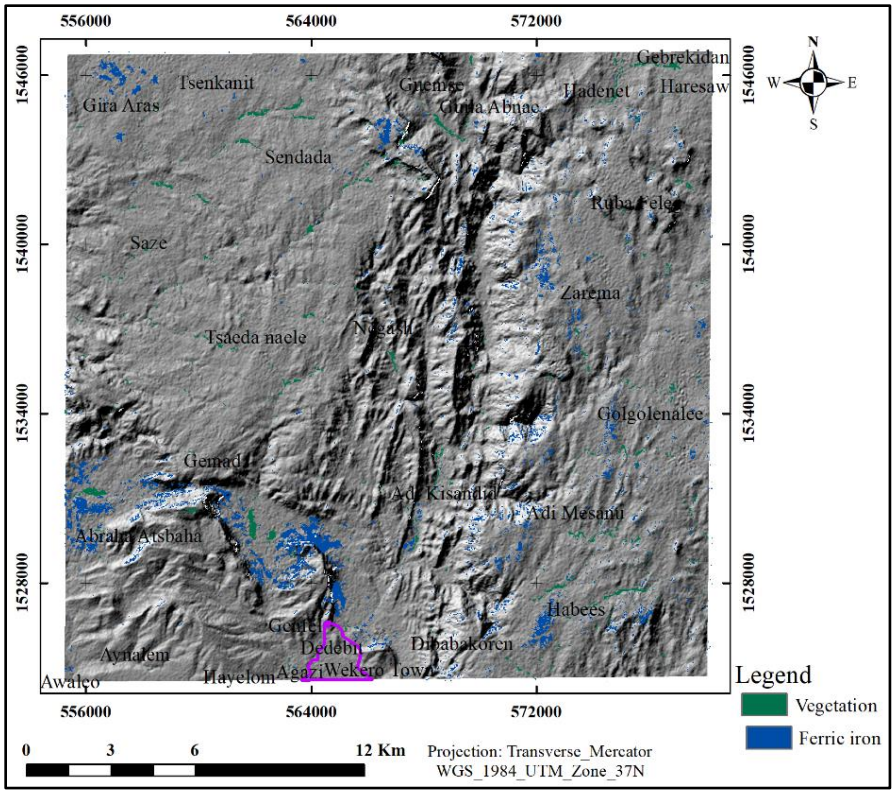

Figure 4. 6. Ferric iron anomaly generated from Landsat 8 OLI.

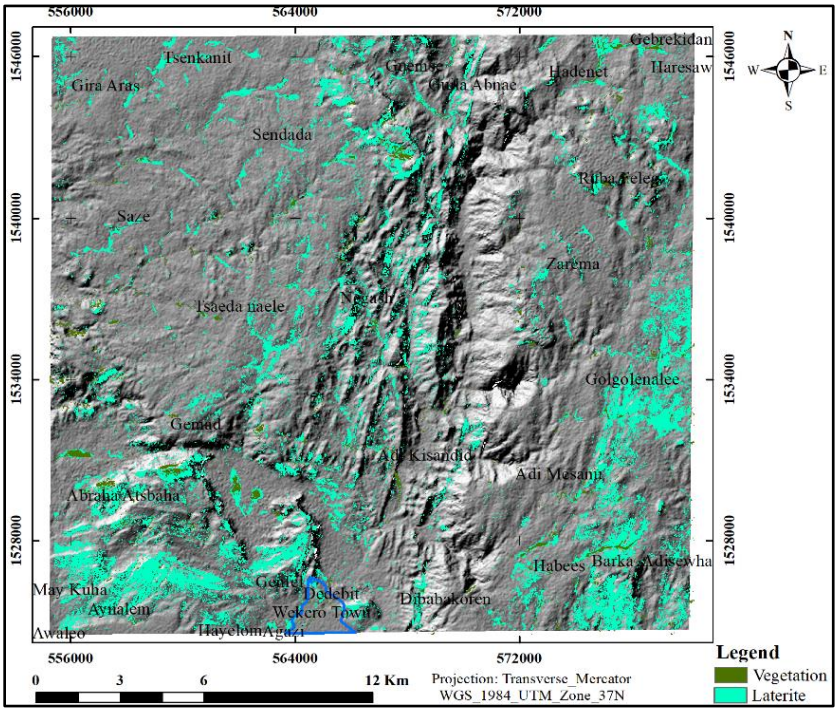

Figure 4. 7. Laterite abundance map generated from ASTER band ratio.

4.2.4 Ratio color composite (RCC)

In this study, ratio color composite images were produced using ASTER band ratio maps, such as band 5/3 + band 1/2, band 4/ band 5 and band 2/ band 1 in RGB (Fig 4.8) and Landsat 8 OLI band ratio maps, such as band 6/band 4, band 5/band 4 and band 4/ band 3 in RGB (Fig 4.9). Each color in the color composite indicates its respective band ratio and the other colors indicate a combination of the RGB.

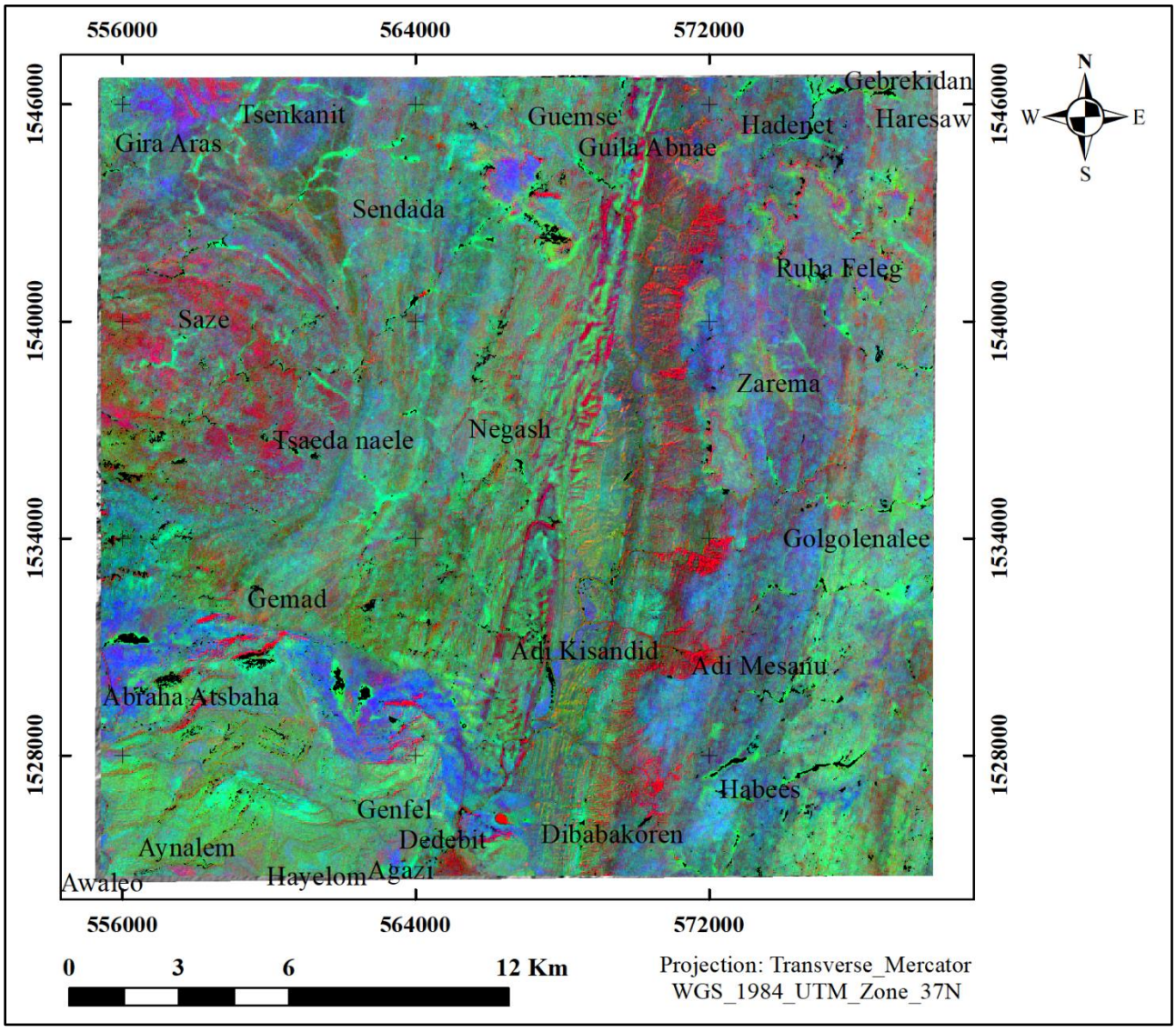

Figure 4. 8. Band composite ratio bands 5/3+1/2,4/5 and 2/1 in RGB.

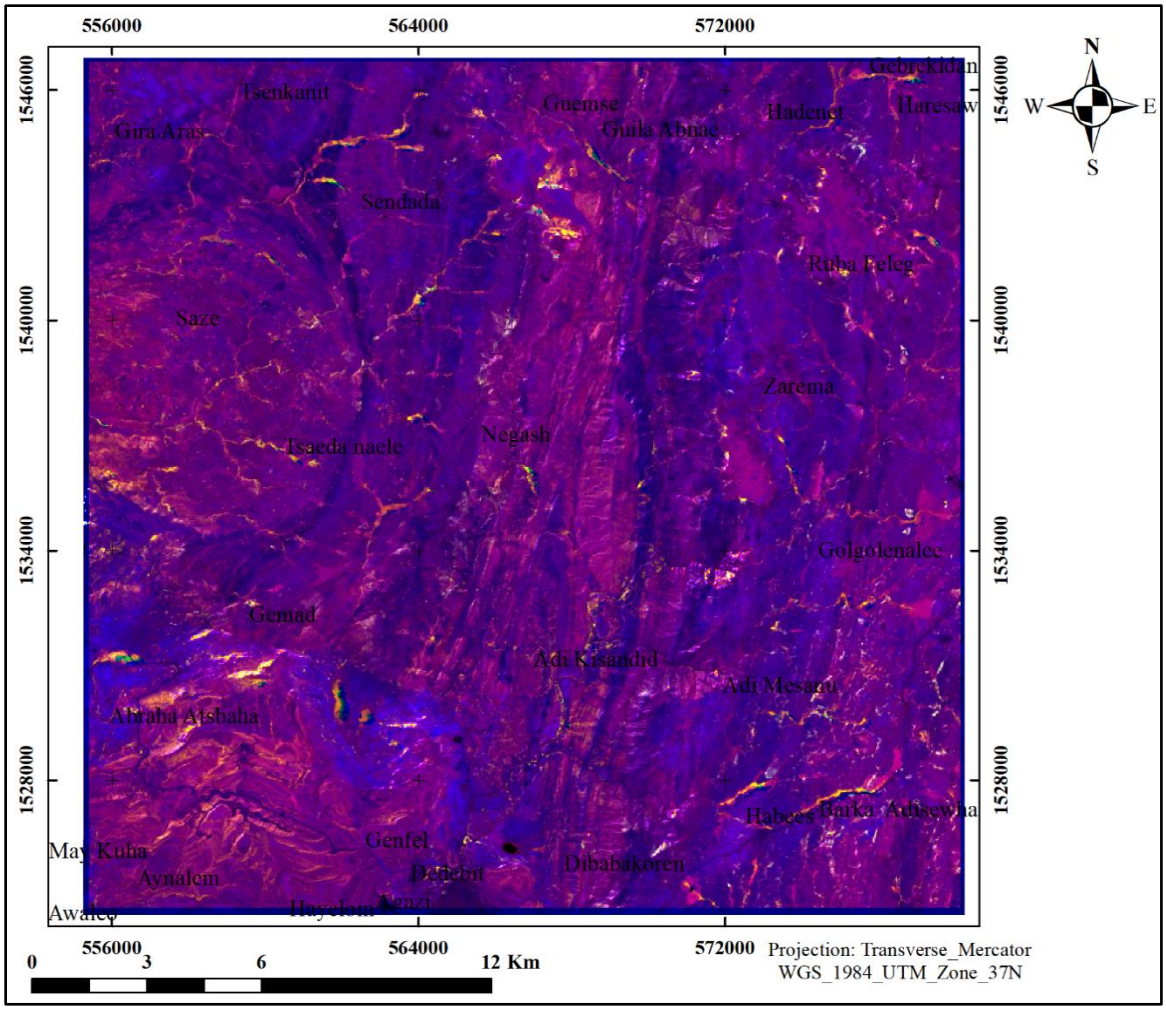

Figure 4. 9. Band composite ratio bands 6/4, 5/4 and 4/3 in RGB.

4.3 Selective PCA abundance maps

To map iron oxides, four bands were chosen from each ASTER and Landsat 8 OLI image. The bands were selected based on absorptive and reflective characteristics of the mineral of interest. Based on Table 4:3, PC4 shows the strong values of the opposing signs between bands 2 (0.853) and band 4 (-0.513) and low contribution from bands 5 and 6. Similarly in Table 4:4, PC4 shows the strong values of the opposing signs between band 1 (- 0.79) and band 2 (0.6) low contribution from bands 3 and 4. To map in bright the PC4 was negated. From Fig 4.10 the target areas are located around Graaras and Abrha we atsbha. Similarly in Fig 4.11 target areas are located around Graaras, Abrha we atsbha, Sendeda, Zarema and Adi mesanu.

Table 4: 3. ASTER bands 1, 2, 3 and 4 eigenvector loadings.

Eigenvectors	Band 1	Band 2	Band 3	Band 4
PC 1	-0.332	-0.473	-0.515	-0.634
PC 2	-0.428	-0.512	-0.152	0.729
PC 3	0.267	0.39	-0.844	0.254
PC 4	0.797	-0.602	-0.013	0.042

Table 4: 4. Landsat bands 2, 4, 5 and 6 eigenvector loadings.

Eigenvectors	Band 2	Band 4	Band 5	Band 6
PC 1	0.189	0.443	0.492	0.725
PC 2	-0.365	-0.468	-0.436	0.677
PC 3	-0.323	-0.567	0.753	-0.08
PC 4	0.853	-0.513	-0.010	0.098

4.4 Endmember spectra generated

All 9 ASTER and 6 Landsat 8 OLI were used for further analysis since the eigenvalues are >1(Table 4.5 and Fig 4.12). The result of the PPI processing is a PPI image showing dark and bright where the bright pixels represent pure pixels (Appendix 3). 10 and 7 of endmembers retrieved from n-D Visualizer for ASTER and Landsat 8 OLI (Fig 4.13 c and d) with their identified region of interest (Fig 4.13 a and b). SFF values > 0.77 were taken as endmember (Table 4.6) for ASTER image and 1 for Landsat 8 OLI (Table 4.7). Finally, 5 for Landsat 8 and 8 for ASTER endmembers were used for this study (Fig 4.15). Since the focus of the study is on mapping iron oxides the matched curves for hematite and goethite are shown in Fig 4.14 a, b, c and d. The SFF values are 0.85 and 0.81 for hematite and goethite of ASTER respectively, and 1 for both in Landsat 8 OLI (Table 4.6 and 4.7).

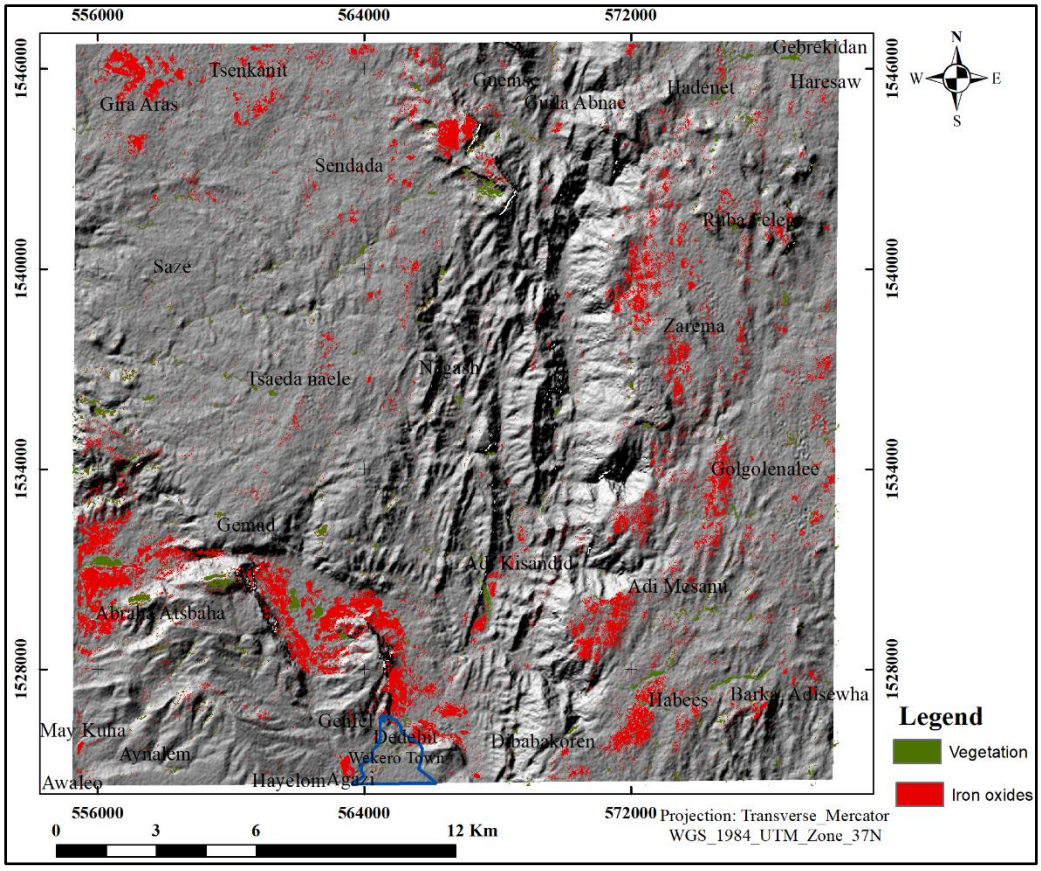

Figure 4. 10. Anomalous map generated from ASTER PC4 overlain on Hill shade image.

Table 4: 5. MNF eigen values of ASTER and Landsat 8 OLI.

Eigenvalues			
ASTER		Landsat 8 OLI	
MNF 1	57.2	MNF 1	16.1
MNF 2	29.3	MNF 2	7.8
MNF 3	11.1	MNF 3	6.4
MNF 4	8.2	MNF 4	5.8
MNF 5	6.2	MNF 5	3.4
MNF 6	5.8	MNF 6	1.99
MNF 7	3.8		
MNF 8	3.3		
MNF 9	2.6		

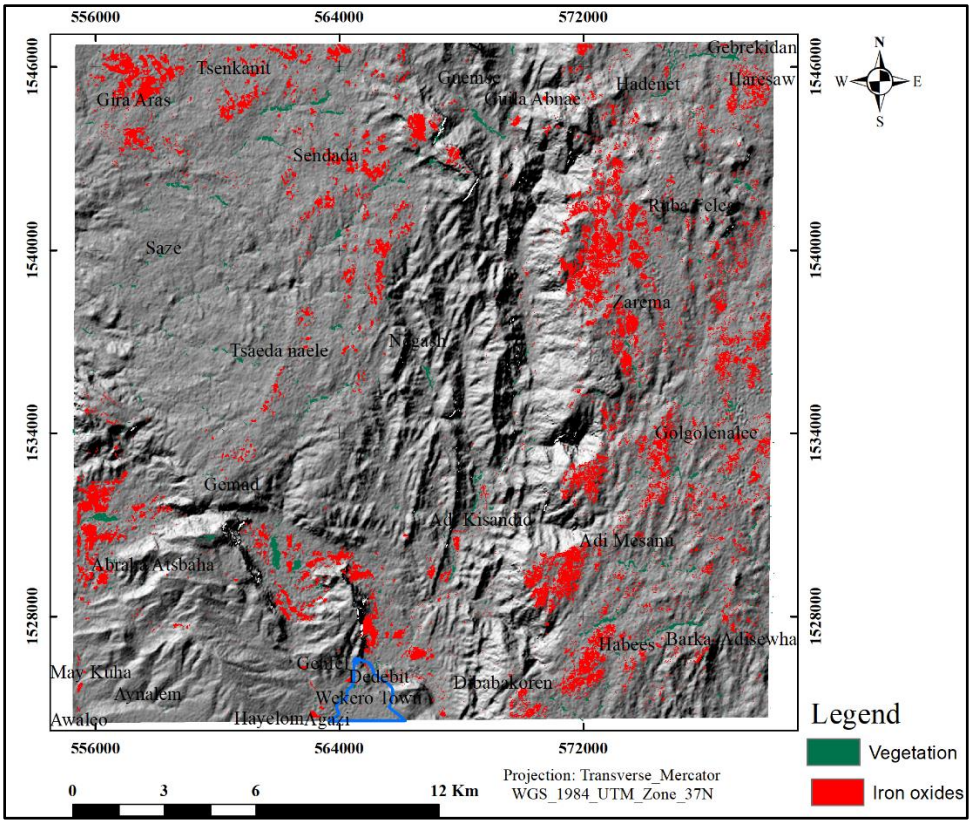

Figure 4. 11. Anomaly map generated from PC4 Landsat 8 OLI overlain on hill shaded image.

Table 4: 6. Unknown and reference spectral curve matching values of ASTER.

n-D class mean	SFF value	Matched known mineral
1	0	No matching mineral
2	0.95	Topaz
3	0.81	Goethite
4	0.96	Alunite
5	0.99	Topaz2
6	0	No matching mineral
7	0.77	Lepidolite
8	0.85	Hematite
9	0.97	Pyrophyllite
10	0.82	Hornblende

Table 4: 7. Unknown and reference spectral curves matching values of Landsat 8 OLI.

n-D class mean	SFF	Matched mineral
1	1	Goethite
2	1	Kaolin
3	1	Hematite
4	1	Alunite
5	0	No matching mineral
6	1	Wollastonite
7	0	No matching mineral

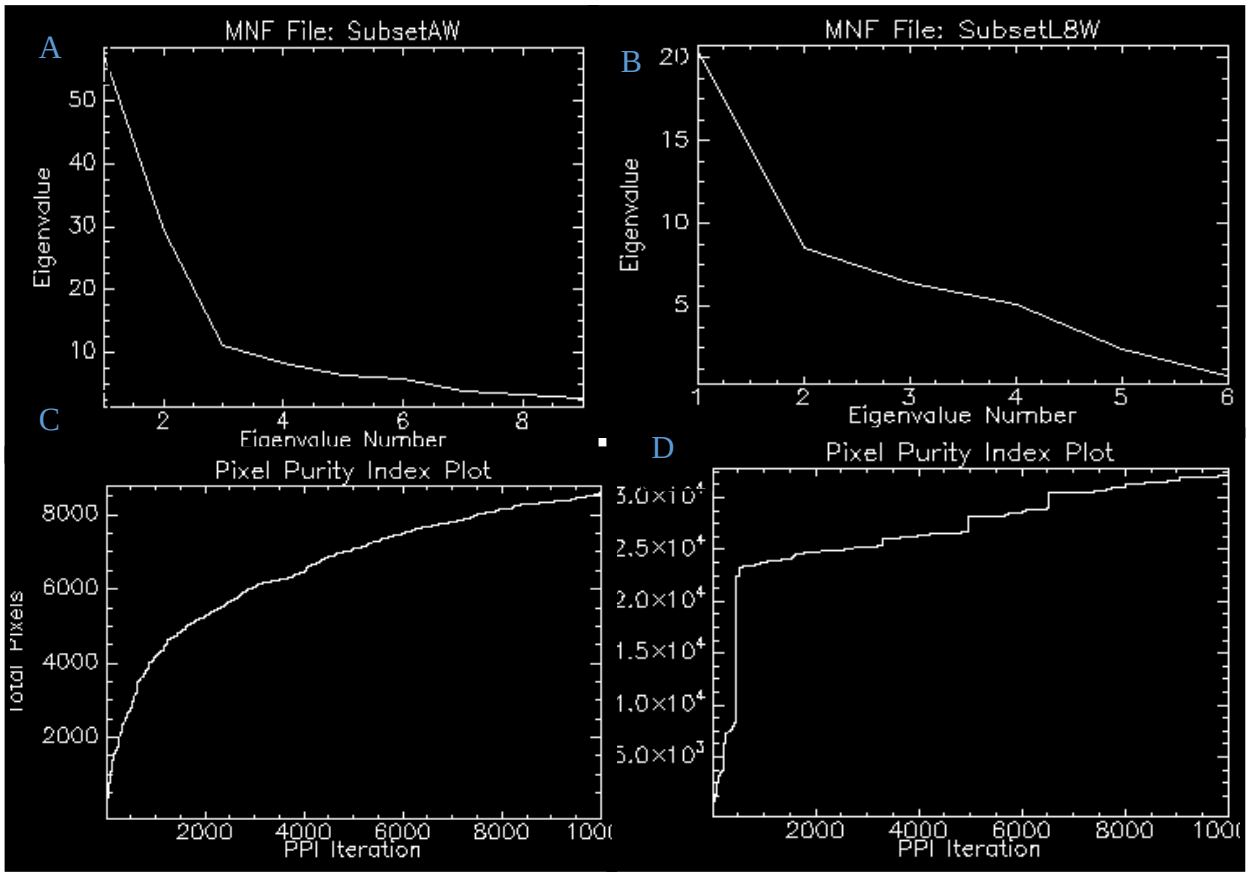

Figure 4. 12. MNF and PPI plots of ASTER (A and C) and Landsat 8 OLI (B and D).

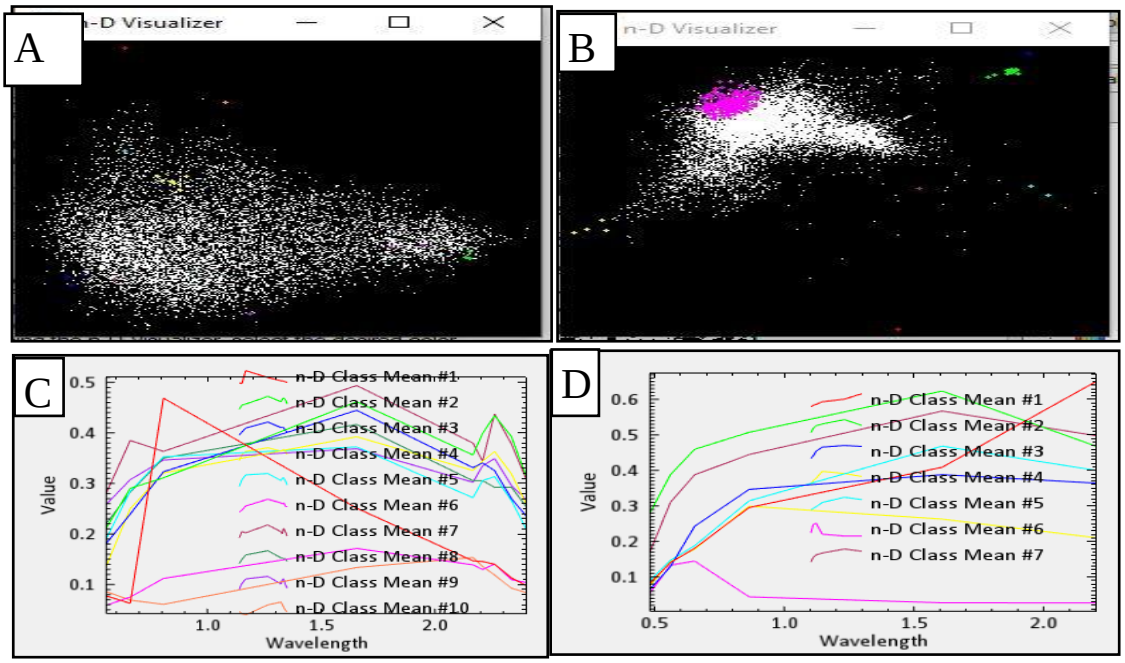

Figure 4. 13. Endmembers extracted in N-D visualizer (a and b) and endmember plots c and d for ASTER and Landsat 8 OLI respectively.

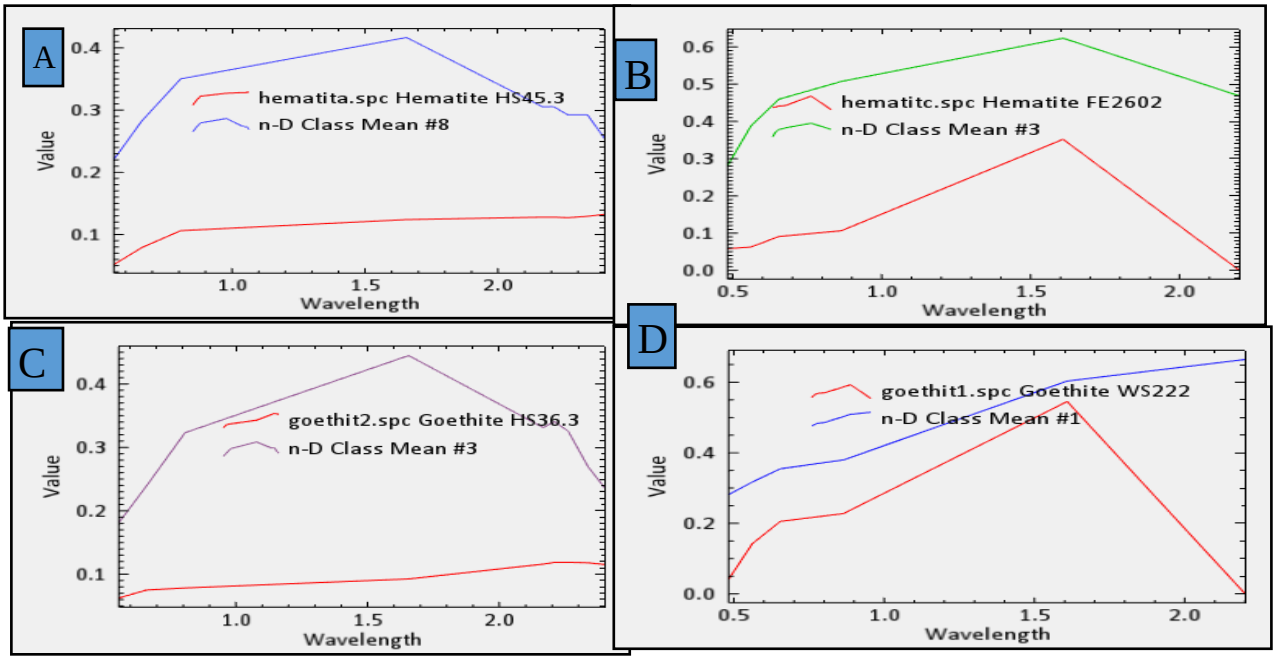

Figure 4. 14. Matched curves of Hematite and goethite for ASTER (a and c) and Landsat 8 OLI (b and d).

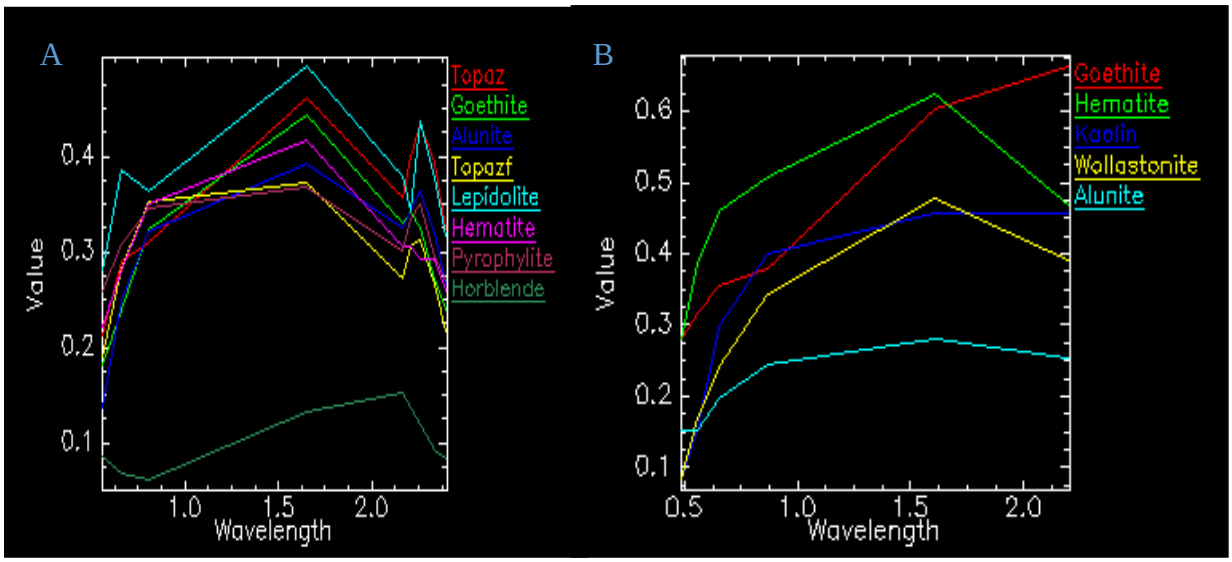

Figure 4. 15. Final endmembers extracted from (a) ASTER and (b) Landsat 8 OLI.

4.5 Abundance maps

4.5.1 Linear spectral unmixing results

The results of linear spectral unmixing are an abundance map for each endmember and one RMS error image. The bright areas indicate a high abundance of the endmember whereas dark areas represent low abundance. Fraction image for the study site gives information about the relative abundance of the endmember material considering each endmember present in a pixel. From Fig 4.16 and 4.17 brighter areas in the fraction, images represent higher abundances of the corresponding end-member, in this case, goethite ranging from -0.45 to 0.75 and hematite -0.8 to 1.

4.5.2 Mixture tuned matched filtering results

The analysis of MTMF produces a collection of rule images that correlate to both the MF and infeasibility scores for each pixel when compared to each endmember spectrum (two rule images per endmember). Places with higher MF scores appear as brighter pixels in the MF images, showing areas with a large abundance of the associated endmember. From Fig 4.18 and 4.19 goethite generated from ASTER ranges from -0.31 to 1 and hematite ranges from -0.42 to 0.88. Whereas goethite has an abundance value ranging from -0.45 to 0.75 and hematite from -0.22 to 0.75 generated from Landsat 8 OLI (Fig 4.20 and 4.21).

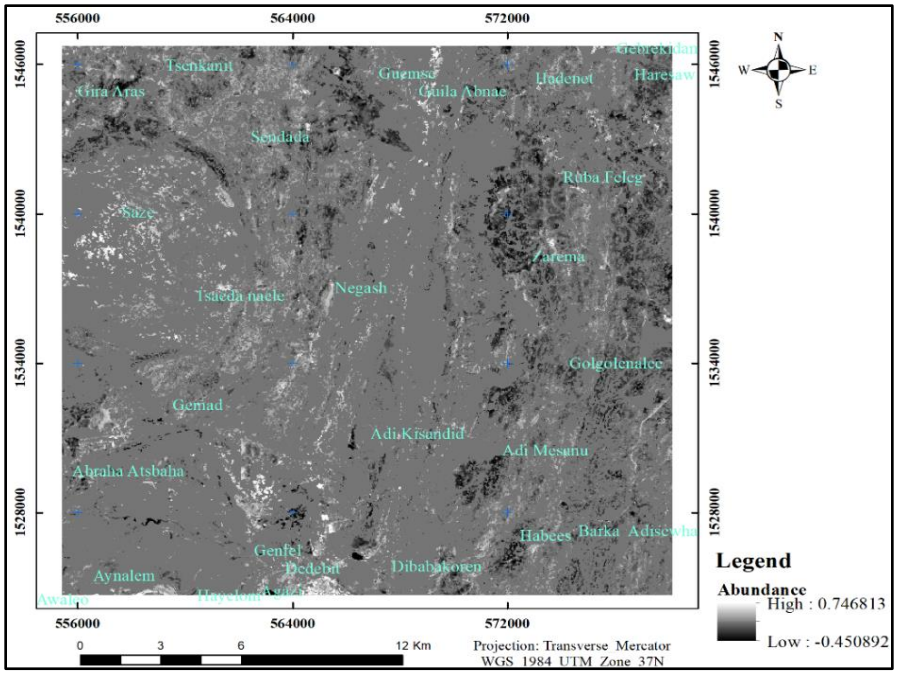

Figure 4. 16. Goethite fractional image derived from ASTER.

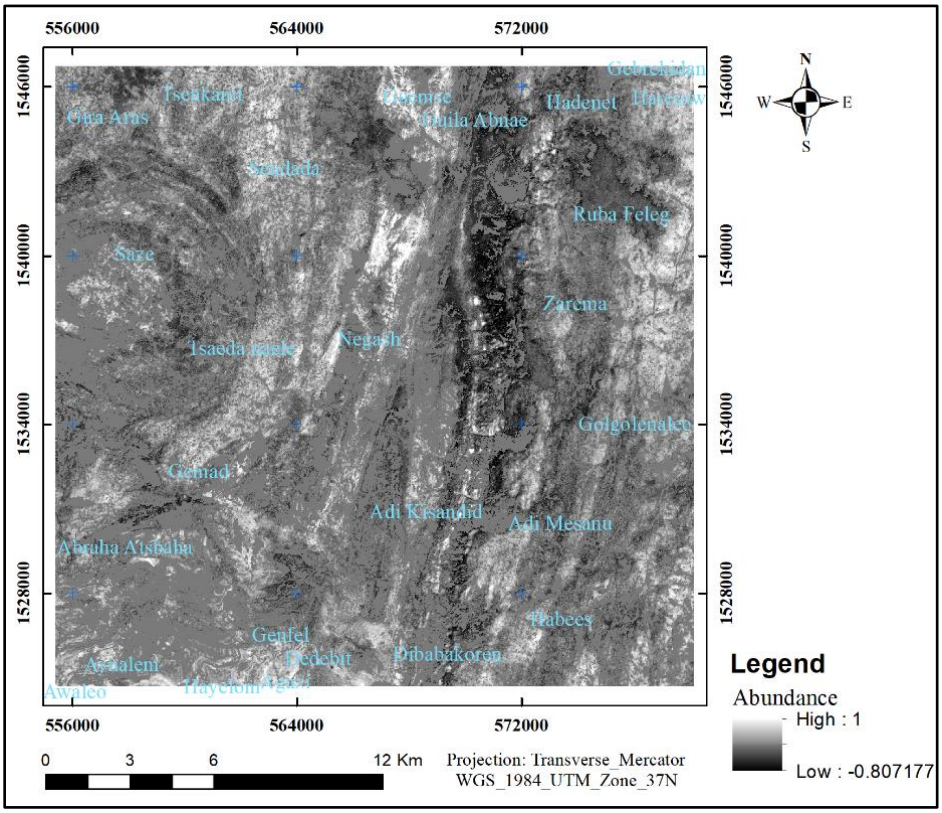

Figure 4. 17. Hematite fractional image derived from ASTER.

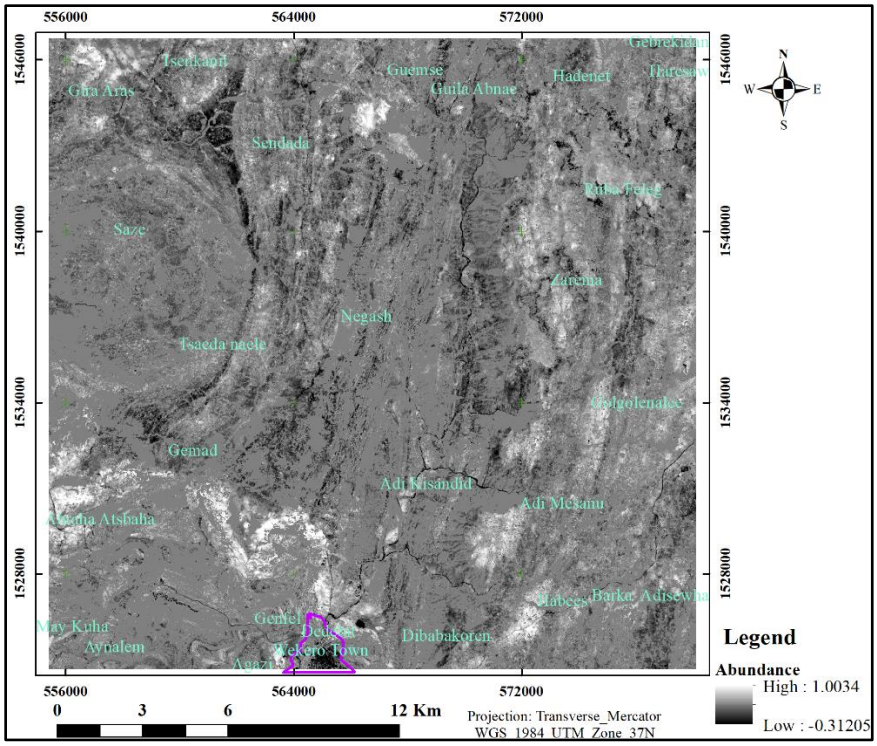

Figure 4. 18. Goethite MF fractional image derived from ASTER.

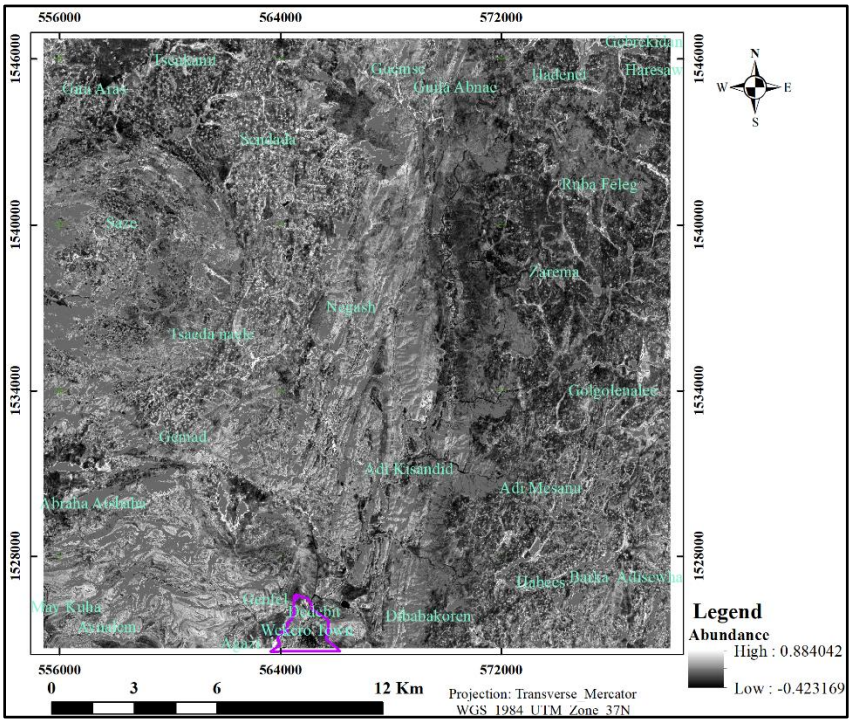

Figure 4. 19. Hematite MF fractional image derived from ASTER.

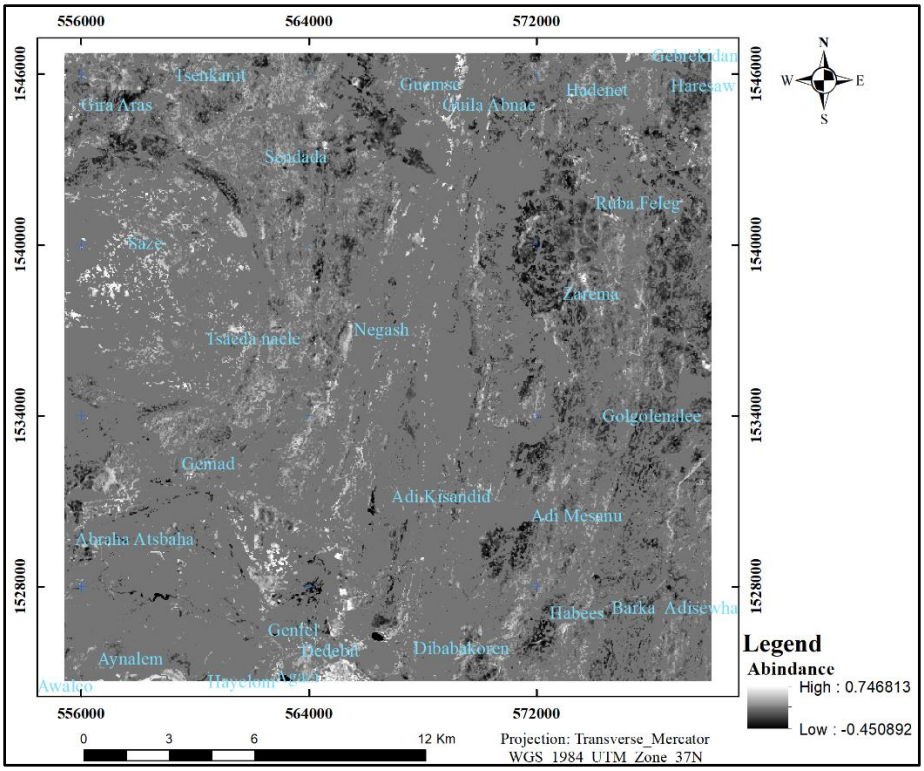

Figure 4. 20. Goethite MF fractional image derived from Landsat 8 OLI.

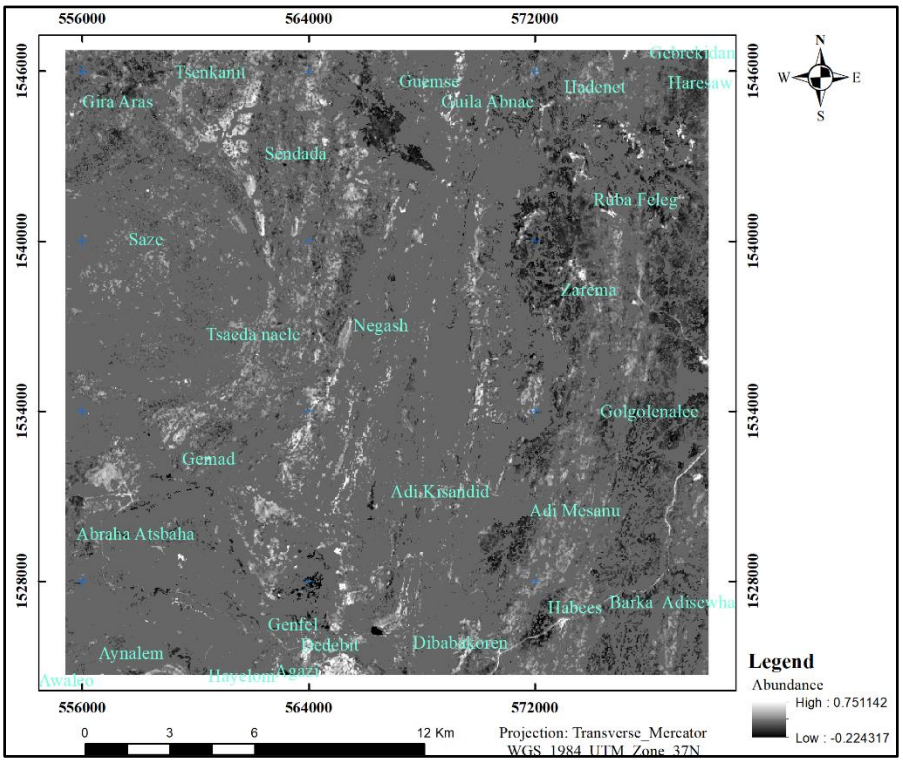

Figure 4. 21. Hematite MF fractional image derived from Landsat 8 OLI.

To map the anomalous areas from unmixing results threshold values of 197 with a confidence level of 92% for goethite and 188 with a confidence level of 98% for hematite were used (Table 4.2). The anomalous areas are shown in Fig 4. 22 and 4.23. In terms of the area mapped hematite unmixing has a maximum which covers an area of 26.4 sq km whereas goethite unmixing lowest area is 8.3 sq km. In Fig 4.22 and 4.23 Saze area shows high goethite and hematite anomalous area.

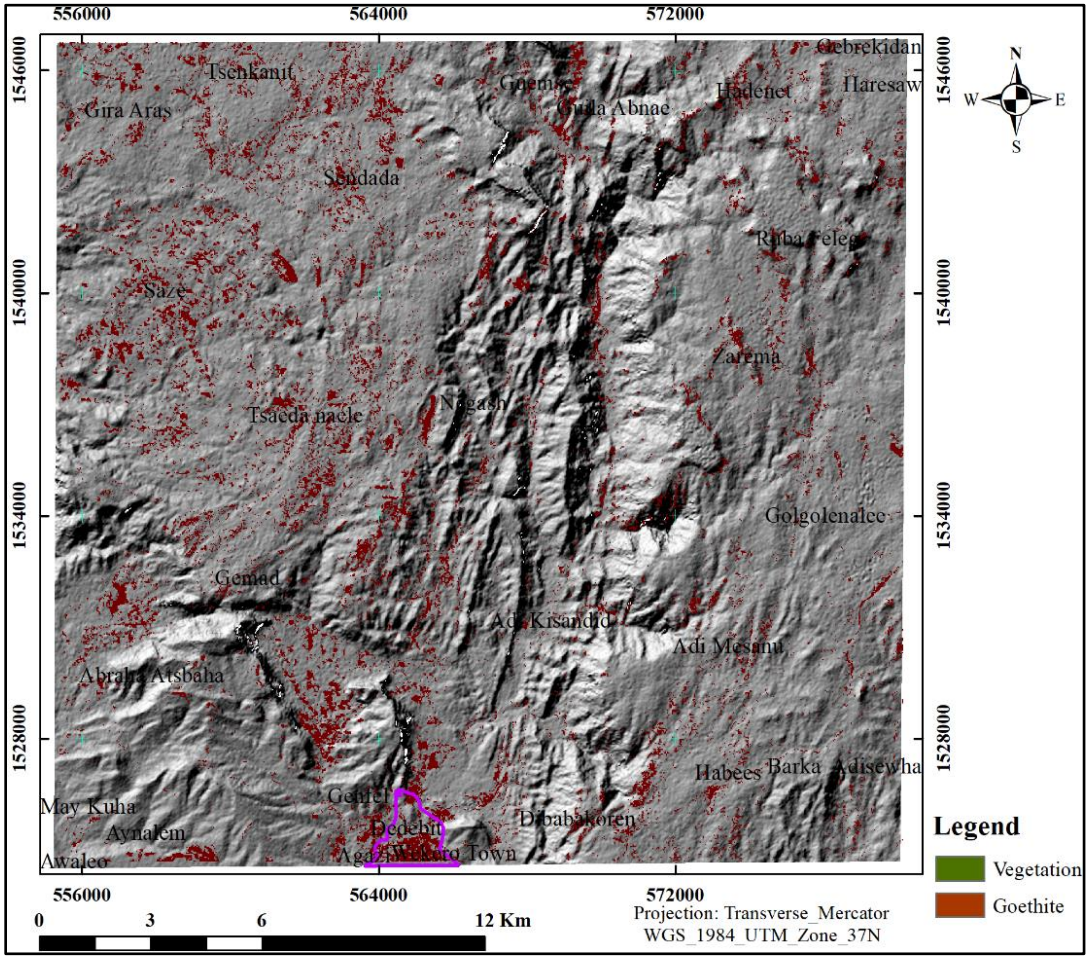

Figure 4. 22. Goethite anomaly derived from ASTER unmixing.

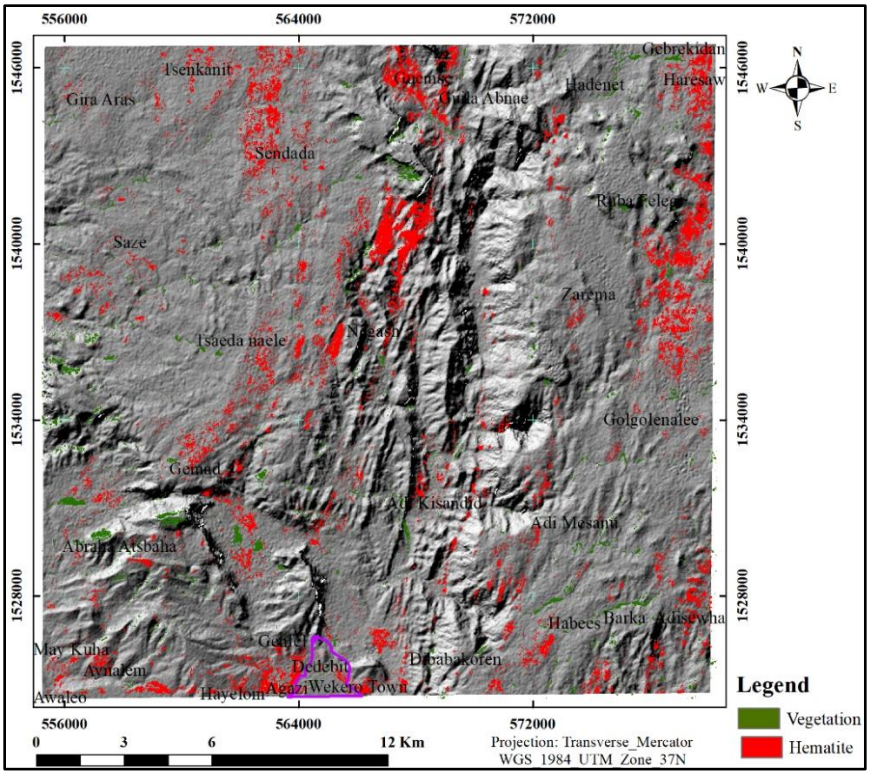

Figure 4. 23. Hematite anomaly derived from ASTER unmixing.

For the MTMF results of both images, the potential areas are identified from MF scores and infeasibility images. The red and green areas in scatter plots are the abundance areas excluding false positives (Fig 4.24 and 4.25).

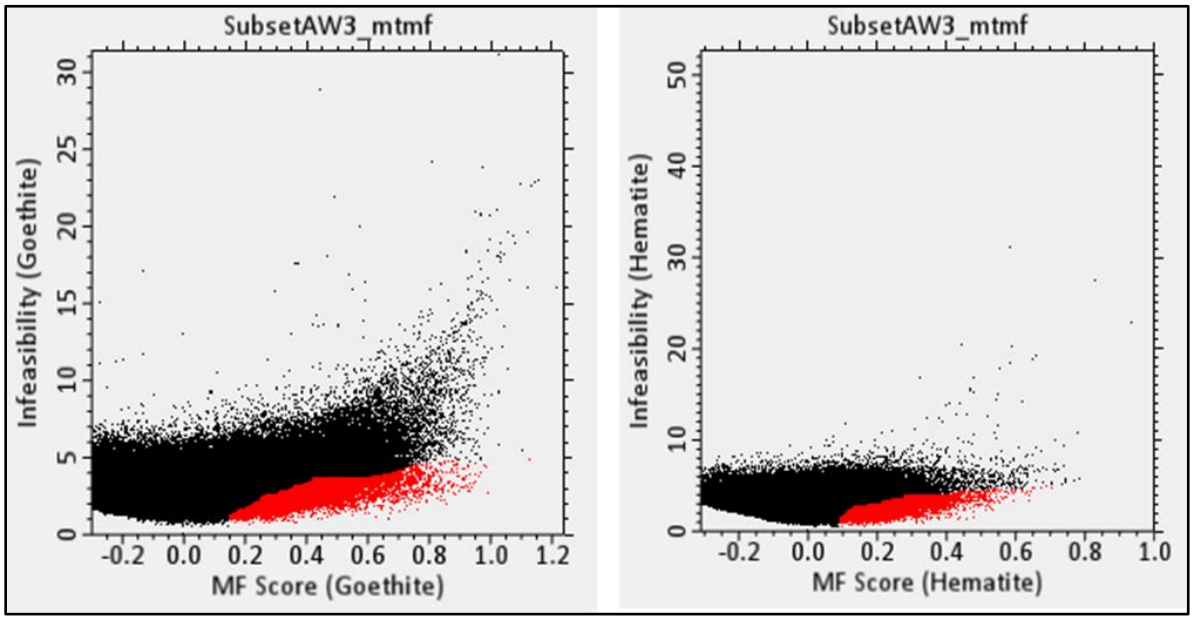

Figure 4. 24. Scatter plots showing high MF and low infeasibility goethite (left) and hematite (right) of ASTER.

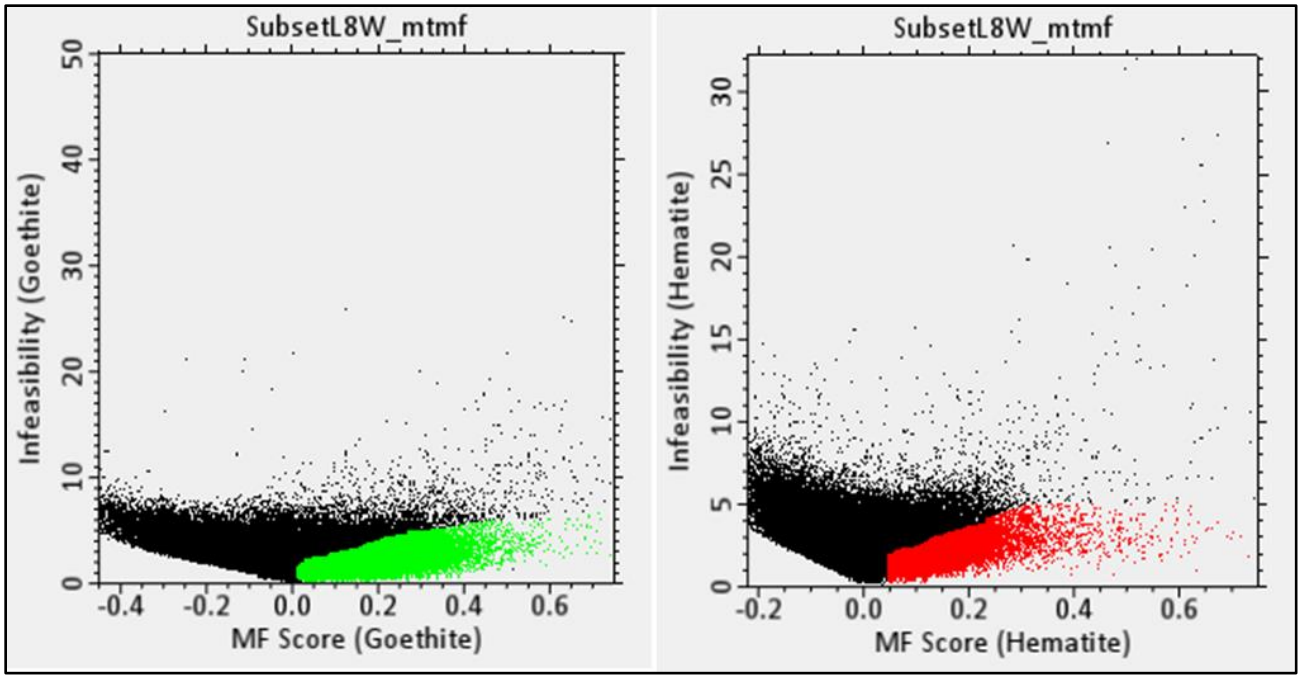

Figure 4. 25. Scatter plots showing high MF and low infeasibility goethite (left) and hematite (right) of Landsat 8 OLI.

The areas having high MF and low infeasibility are shown in Fig 4. 26 to 4. 29.

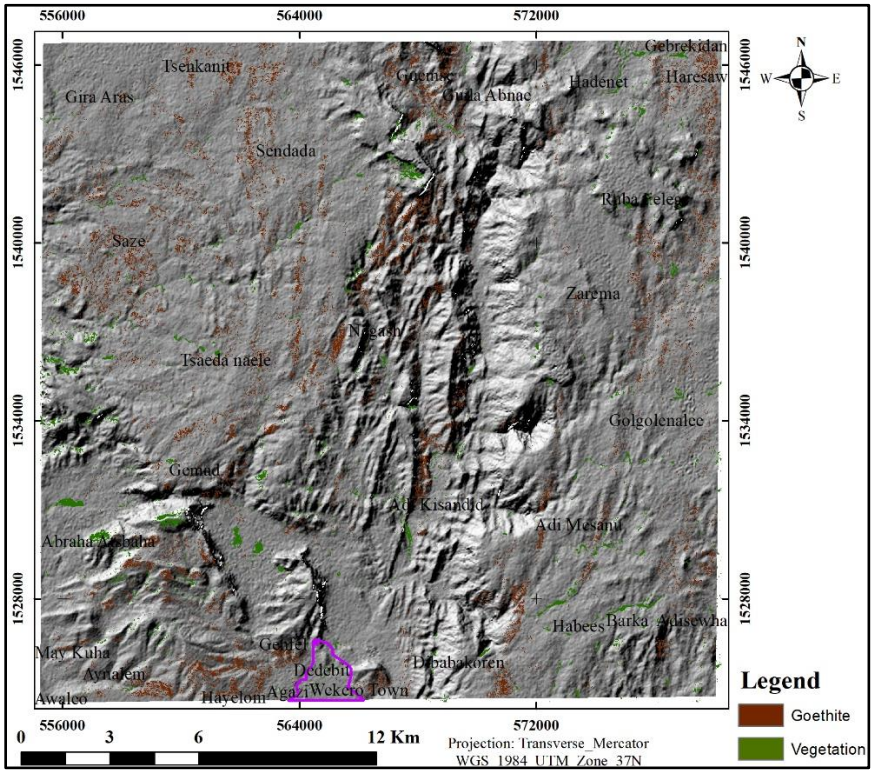

Figure 4. 26. Goethite anomaly derived from ASTER MTMF.

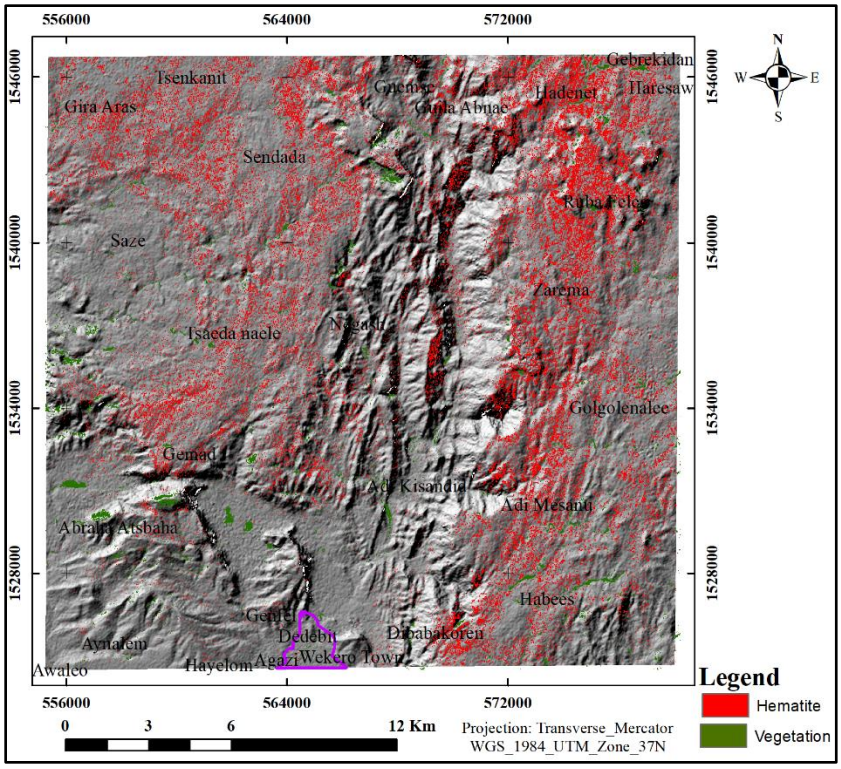

Figure 4. 27. Hematite anomaly derived from ASTER MTMF.

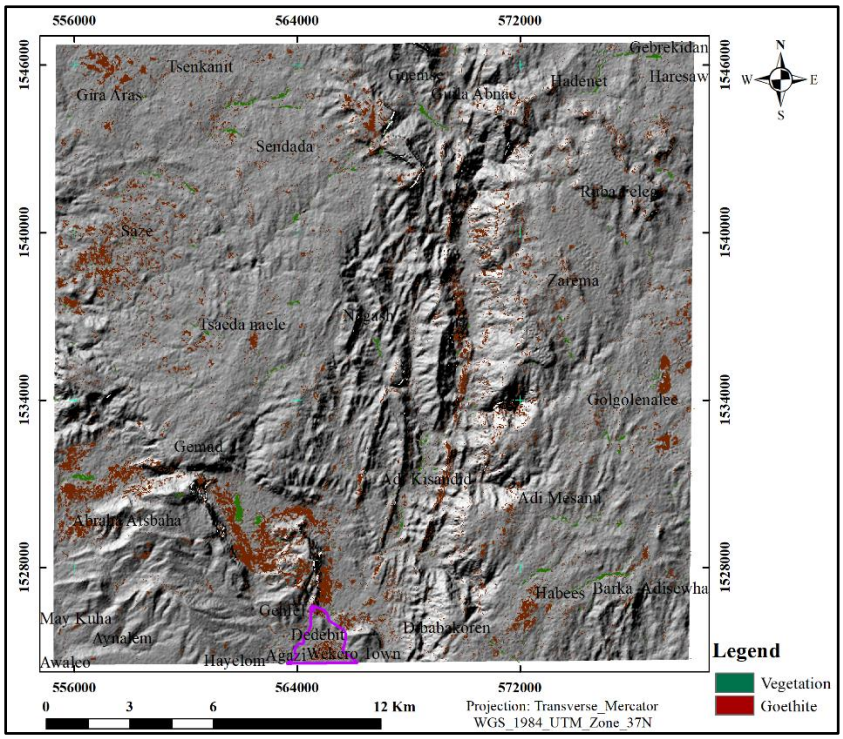

Figure 4. 28. Goethite anomaly derived from Landsat 8 OLI MTMF.

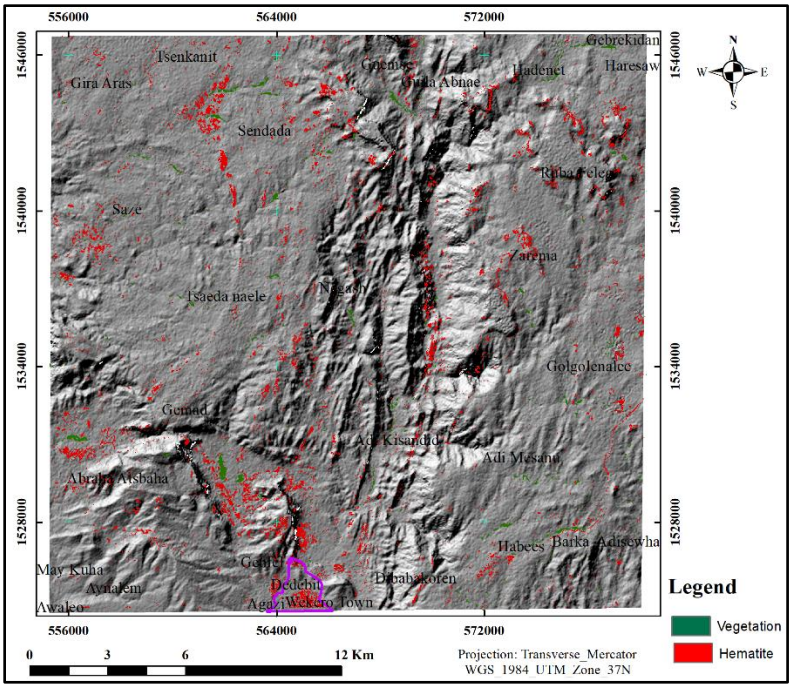

Figure 4. 29. Hematite anomaly derived from Landsat 8 OLI MTMF.

4.6 Correlation and validation of results

4.6.1 Correlation analysis results

To see the relationship between results obtained from Landsat 8 OLI and ASTER Pearson correlation coefficient was calculated. The result shows a strong positive correlation between results obtained using selective PCA with r = 0.59, and r = 0.3 moderate positive correlation between ferric iron, a poor positive correlation for ferrous iron with r = 0.22. For MTMF results both hematite and goethite have a poor positive and negative correlation with r= 0.15 and -0.25 respectively. The low correlation could be because of the inability of the multispectral sensors to differentiate minerals having the same group. Fig 4.30 and 4.31 show scatter plots of the results.

4.6.2 Validation and comparison results

The results show that the existing iron oxide polygons overlay with the iron oxides of ferric iron, laterite, ferrous iron of ASTER but the band ratio resulted from Landsat 8 OLI has poor overlay (Fig 4.32). From Fig 4.33 the results obtained from selective PCA shows a better overlay with the existing iron oxide polygons. Although, both of the overlays with the existing iron oxide polygons selective PCA of ASTER fits better. On the other hand, Fig 4.34 Whereas results obtained from hematite unmixing and goethite ASTER MTMF have a better fit with the existing

polygons whereas hematite ASTER MF shows a good overlay. The MTMF obtained from Landsat 8 OLI and goethite unmixing show a very poor overlay. The results obtained from MF Landsat 8 OLI have a better fit with the existing polygons.

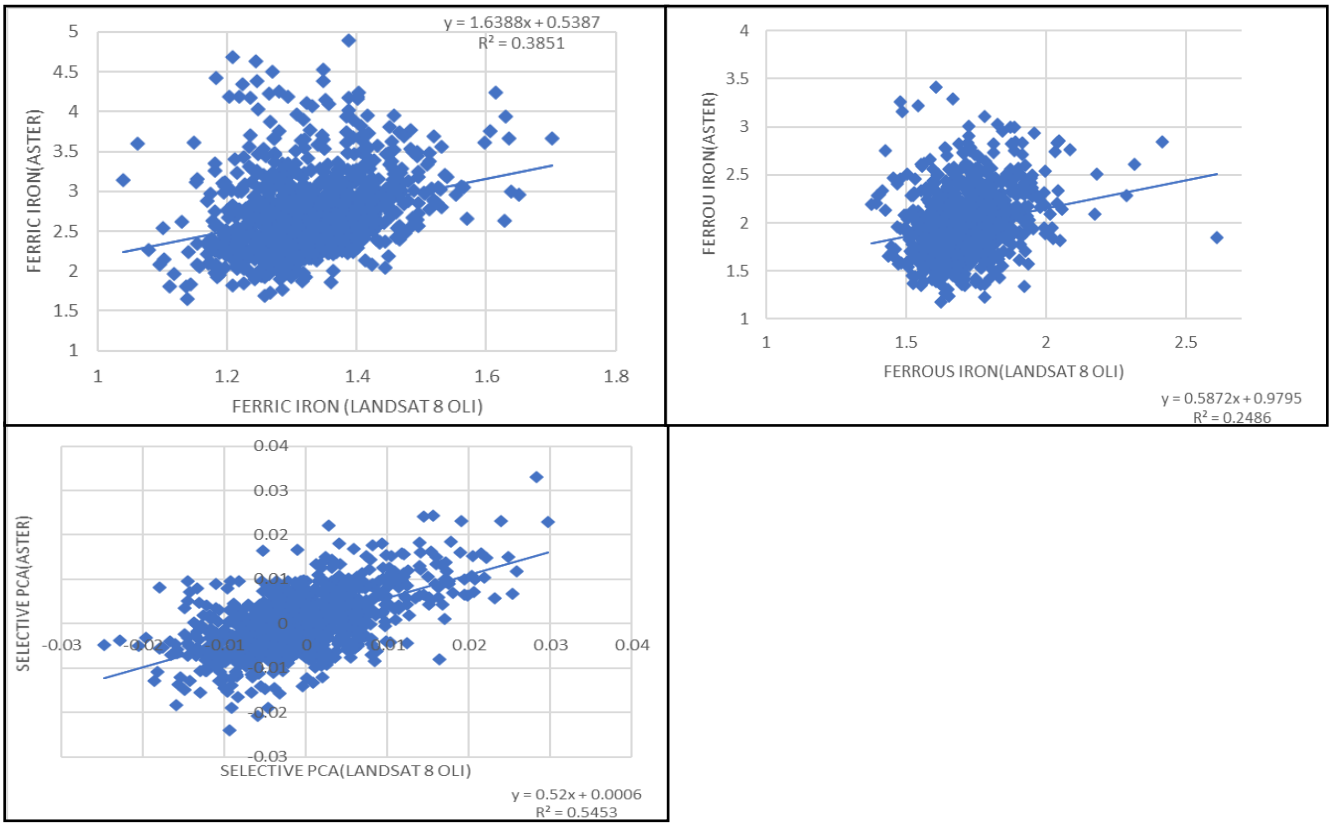

Figure 4. 30. . Graphs showing b/n results obtained from image processing of Landsat 8 OLI and ASTER.

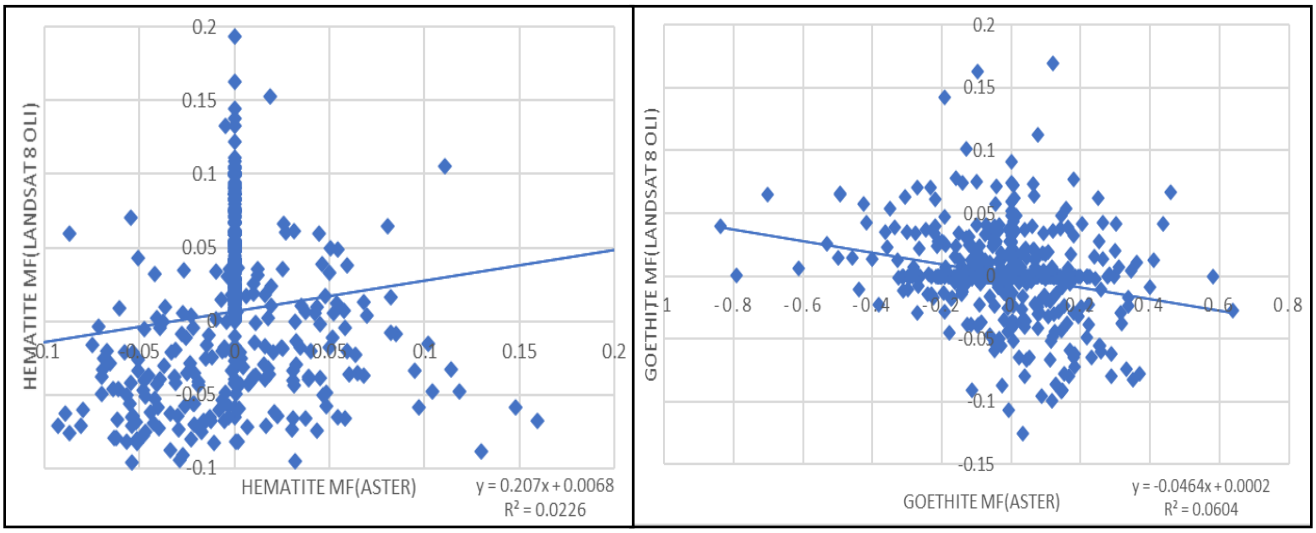

Figure 4. 31. Graphs showing correlation b/n results obtained from Landsat OLI and ASTER MTMF.

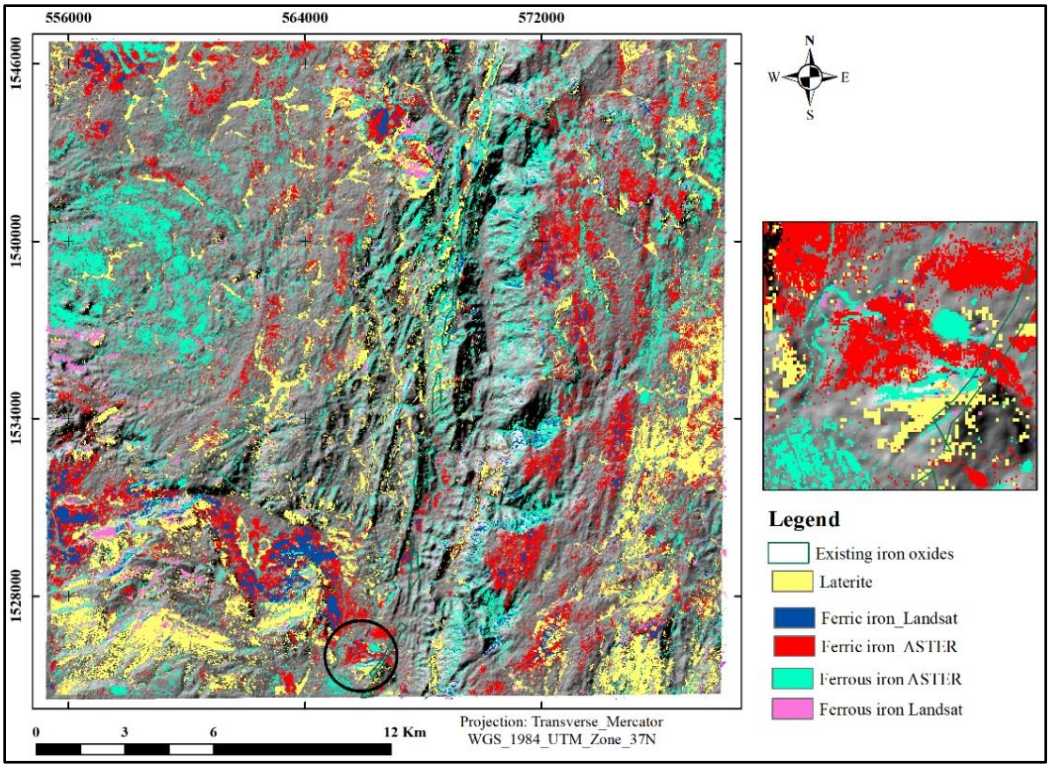

Figure 4. 32. Ratio anomalous areas overlay on polygons of the existing iron oxides.

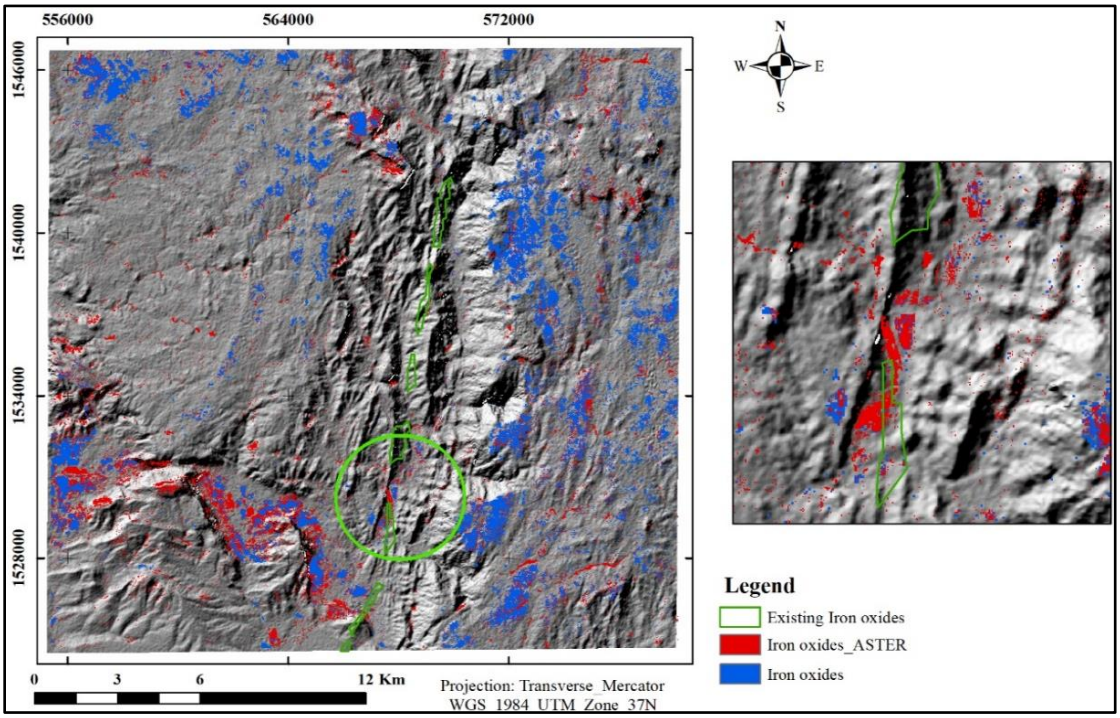

Figure 4. 33. Selective PCA results overlay with existing iron oxide polygons.

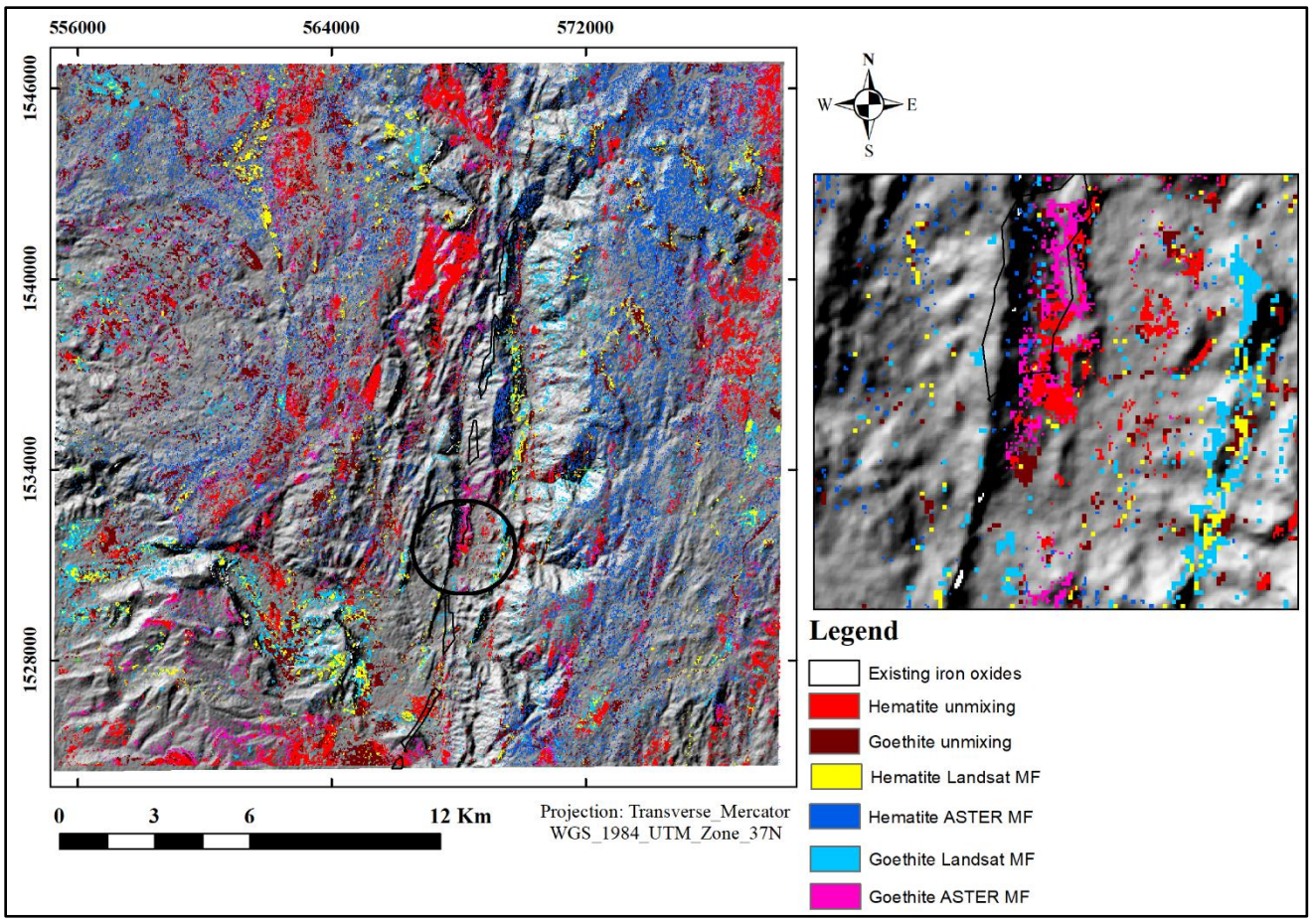

Figure 4. 34. Unmixing and MTMF result overlay on existing iron oxide polygons.

CHAPTER FIVE

5 DISCUSSION

5.1 NDVI and NDVI masking

The better spectral and spatial characteristics of ASTER and Landsat 8 OLI images provide useful information on the delineation of iron ore deposits. In the wavelength ranges covered by Landsat TM bands 1 (blue) and 2 (green), which are analogous to bands 2 (blue) and 3 (green) in Landsat 8 OLI, vegetation and iron oxides show similar reflectance spectra. In places with heavy or low vegetation cover, these bands aren't very useful for differentiating iron oxides. As a result, in this investigation, it is decided to mask out the vegetation. Hence, there is much interference by vegetation while mapping the iron ore bands, from the ASTER images and Landsat 8 OLI. To overcome these different vegetation indices such as ratio indices and soil adjusted vegetation indices and NDVI were mapped. Since NDVI saturates values above 0.7, NDVI maps were generated to know areas that contain either the country rocks or iron ore bands which was also adopted by Gopinathan *et al*., (2020). The use of masking to remove vegetation helped to reduce the influence of vegetation in delineating areas with high iron oxide content in this study values greater than 0.3 for Landsat 8 OLI which was similarly used by (Tompolidi *et al*., 2020) and 0.4 for ASTER. The ASTER image's vegetation mask is denser than the Landsat 8 LI images which agrees with Traore *et al*., (2019). This discrepancy is due to the acquisition date of these images.

5.2 Band ratios and ratio color composites

Band rationing techniques were used to generate the abundance of iron oxide content in various parts of the study area. The results were obtained using different band ratios such as Ferric (Fe^{3}+) band 2 / band 1, for Ferrous iron (Fe^{2}+) band 5 / band 3 + band 1 / band 2 and laterite band 4 / band 5 whereas from Landsat 8 OLI band 6/band 4 for Ferrous (Fe^{2}+), band 4/band 3 for ferric iron (Fe^{3}+). Although band 4/2 was also tested to map ferrous iron from Landsat 8 OLI it showed very poor results. To distinguish the minerals, the threshold value for each resultant image was computed statistically using mean and standard deviation (Table 4.2) which was similarly used by San *et al*., (2004). The value above the threshold was overlain on the hill shade images of ASTER and Landsat 8 OLI. The high anomalous iron content in the western part of the study area in the ferrous iron map (Fig 4.3) and laterite map (Fig 4.7) generated from ASTER could be explained by the alteration of biotite in granite to iron oxides which were similarly interpreted

by Cardoso-Fernandes *et al*., (2019). Area mapped was also calculated for iron oxide to know and estimate the extent of the anomalous zones.

In displaying the color composite image, three primary colors (red, green and blue) are used. In this study, ratio color composite images were produced using ASTER band ratio maps, such as band 5/3 + band 1/2, band 4/ band 5 and band 2/ band 1 (Fig 4.8) and using Landsat 8 OLI band ratio maps, such as band 6/band 4, band 5/band 4 and band 4/ band 2 (Figure 4.9). The ratio color composite maps are perhaps better for visualization and interpretation to bring out the location of iron ore bands and laterites which were similarly applied by Gopinathan *et al*., (2020) only for ASTER images and Traore *et al*., (2019) for Landsat 8 OLI.

5.3 Selective PCA

Based on Table 4.3, PC4 shows the strong values of the opposing signs between bands 2 (0.853) and band 4 (-0.513) and low contribution from bands 5 and 6. Similarly in Table 4.4, PC4 shows the strong values of the opposing signs between band 1 (- 0.79) and band 2 (0.6) low contribution from bands 3 and 4. For both images, PCA 4 is selected since PCA 4, in ASTER in band 1 and 2 the values are high with opposite magnitude and in Landsat 8, PCA 4 has a high value in opposite sign in band 2 and band 4. Since the values are negative in reflective bands iron oxides are dark (Table 4.2 and 4.3). But to show in bright the PCA 4 was multiplied by negative 1, similarly iron oxide was mapped in PC4 from both images by Traore *et al*., (2019). And the target was sliced using 210.5 and 214.2 thresholds for ASTER and Landsat 8 OLI respectively to map anomalous area.

5.4 Abundance maps analysis

Before endmember extraction spatial and spectral data reduction is important. In this study, minimum noise fraction was applied for ASTER 9 bands and 6 Landsat 8 OLI bands for spectral data reduction. All 9 ASTER and 6 Landsat 8 OLI were used for further analysis since the eigenvalues are >1(Table 4.5). The Pixel Purity Index (PPI) was run on the MNF data to aid in deriving endmembers from the image and spatial data reduction. The number of iteration and thresholds used were 10,000 and 2.5 for both images (Fig 4. 14 c and d) which was similarly used by Hosseinjani and Tangestani, (2011). The result of the PPI processing is a PPI image showing dark and bright where the bright pixels represent pure pixels (Appendix 3) which agrees with Hosseinjani and Tangestani, (2011). To use for matching reference spectra with unknown spectra the USGS spectral library was resampled in ENVI 5.3 using ASTER and Landsat 8 OLI

as input images. Using Spectral analyst the known reference spectral was matched with unknown spectral derived from the images and spectral feature fitting ranked the match. SFF values > 0.77 were taken as endmember (Table 4.6) for ASTER image and 1 for Landsat 8 OLI (Table 4.7) which is above 0.5 thresholds by (Kalinowski. and Oliver, 2004).

Finally, 5 for Landsat 8 and 8 for ASTER endmembers were used for this study (Fig 4.18). Since the focus of the study is on mapping iron oxides the matched curves for hematite and goethite have shown a good match (Fig 12 a, b, c and d). The SFF values are 0.85 and 0.81 for ASTER and 1 for Landsat 8 (Table 4.6 and 4.7). Spectral unmixing results are highly dependent on the input endmembers and changing the endmembers would change the results which were also proved by Gopinathan *et al*., (2020).

Linear Spectral Unmixing is a means of determining the relative abundances of materials depicted in multispectral imagery based on the materials of spectral characteristics. The bright areas indicate a high abundance of the endmember whereas dark areas represent low abundance. Although the unmixing result was constrained to one, the results contain a negative value, which is physically meaningless. The negative values are the background similar result was obtained by Calin *et al*., (2015). Both goethite anomaly derived from ASTER unmixing (Fig 4.22) and derived from Landsat 8 OLI MTMF (Fig 4.28) shows high targets in the western part of the study area could be explained by the alteration of biotite in granite to iron oxides which were similarly interpreted by Cardoso-Fernandes *et al*., (2019).

The MF images show areas with higher MF scores as brighter pixels, thus highlighting the areas with a large abundance of respective endmember. Correctly mapped pixels have an MF score above the background distribution, which has some noise-limited spread around zero, and a low infeasibility value. To map the potential areas 2-D scatter plot was prepared using MF score and infeasibility. Pixels at the right bottom show high MF scores and low infeasibility which are mapped as potential areas. MTMF is not dependent on the input endmembers. Although it was constrained to 1 there is a negative result that is physically meaningless which was similarly interpreted by Calin *et al*., (2015).

5.5 Correlation, comparison and validation analysis

A strong correlation was between results obtained selective PCA with r = 0.59, and r = 0.3 moderate correlation between ferric iron, a poor correlation for ferrous iron with r = 0.22. For unmixing and MTMF results both hematite and goethite have a poor positive and negative

correlation with r= 0.15 and -0.25 respectively which was similarly interpreted by (Neway Kifle and Binyam Tesfaw, 2021) for LST. In validating the results obtained using selective PCA show the best fit with the existing iron oxide polygons and the band ratio resulted from Landsat 8 OLI has a poor match. Whereas results obtained from hematite unmixing and goethite ASTER MTMF have a better fit with the existing polygons whereas hematite ASTER MF shows a good overlay. The MTMF obtained from Landsat 8 OLI and goethite unmixing show a very poor overlay. The comparison shows ASTER mapped better than Landsat 8 OLI for band ratio selective PCA, unmixing and MTMF.

CHAPTER SIX

6 CONCLUSION AND REMMENDATIONS

6.1 Conclusion

This study was conducted on mapping of ferric (Fe^{3}+) and ferrous (Fe^{2}+) iron oxides distribution using ASTER and Landsat 8 OLI data, in Negash Lateritic iron deposit, Northern Ethiopia. Abundance maps were generated both from pixel level and sub-pixel level and then anomalous areas were detected using thresholding with confidence levels ranging from 92% to 98%. The mean and standard deviation were used to calculate the threshold values. The result shows ASTER band ratio maps better for both ferrous and ferric iron oxides. The finding of the results obtained from selective PCA shows PC4 of both ASTER and Landsat 8 OLI mapped the iron oxides in dark.

From linear spectral unmixing an abundance map for each endmember and one RMS error image was mapped. Fraction image for the study site gives information about the relative abundance of the endmember material considering each endmember present in a pixel. From the analysis, MTMF produces a collection of rule images that correlate to both the MF and infeasibility scores. Places with higher MF scores appear as brighter pixels in the MF images, showing areas with a large abundance of the associated endmember. Both the MTMF and LSU showed the poor capability to differentiate goethite and hematite.

The finding shows a high correlation between results obtained using selective PCA with r = 0.59, and r = 0.3 moderate correlation between ferric iron, a poor correlation for ferrous iron with r = 0.22. The result was validated using existing iron oxide polygons and results obtained from selective PCA show the best match with the existing iron oxide polygons. Results obtained from ASTER images show a better match with the existing iron oxide polygons. The ASTER-derived unmixing and MTMF results also show a good match with the existing polygons. The comparison shows ASTER mapped better than Landsat 8 OLI for band ratio selective PCA, unmixing and MTMF.

6.2 Recommendations

The study utilizes remotely sensed multispectral images to detect and identify spectral anomalies of iron oxides based on the spectral signature of the mineral. The result shows the applied techniques can be used as preliminary iron oxide exploration in collaboration with a field

visit. In comparison to ordinary exploration methods for mineral exploration, the use of remotely sensed for preliminary prospect works well by minimizing exploration cost, time and overpowering challenges of inaccessibility. Thus, better to use these techniques in the exploration and mining sectors in poor countries like Ethiopia.

Since highly vegetated areas can also contain huge iron oxide minerals it's better to integrate other techniques such as geophysical and geochemical analysis to check the presence of iron oxides in vegetated areas.

The results obtained through subpixel techniques have a low correlation to minimize this it is better to use oversampled images (hyperspectral images).

Finally, I recommend to further apply image processing techniques to grade-wise categorization and grade estimation.

REFERENCES

Abera Fantaye (2009) Mapping Hydrothermally Altered Rocks and Lineament Analysis through Digital Enhancement of Aster Data Case Study: Kemashi Area, Western Ethiopia. Addis Ababa University.

Adams, J. B. J. R. g. a. E. and composition, m. (1993) Imaging spectroscopy: Interpretation based on spectral mixture analysis, pp. 145-166.

Alasta, A. F. 'Using Remote Sensing data to identify iron deposits in central western Libya'. *International conference on Emerging trends in Computer and Image processing, Bangkok*, 56-61.

Asfawossen Asrat&Barbey, P. and Gleizes, G. J. A. G. R. (2001) The Precambrian geology of Ethiopia: a review, **8**(3/4), pp. 271-288.

Bangira, T.&Alfieri, S. M.&Menenti, M.&Van Niekerk, A. and Vekerdy, Z. J. R. s. (2017) A spectral unmixing method with ensemble estimation of endmembers: Application to flood mapping in the Caprivi floodplain, **9**(10), pp. 1013.

Boardman, J. W. 'Automating spectral unmixing of AVIRIS data using convex geometry concepts'. *Proc. Summaries 4th Annu. JPL Airborne Geosci. Workshop*, 11-14.

Boardman, J. W. 'Leveraging the high dimensionality of AVIRIS data for improved sub-pixel target unmixing and rejection of false positives: mixture tuned matched filtering. *Summaries of the seventh JPL Airborne Geoscience Workshop, JPL Publication*, (1998): NASA Jet Propulsion Laboratory, 55-56.

Boardman, J. W.&Kruse, F. A. and Green, R. O. (1995) Mapping target signatures via partial unmixing of AVIRIS data.

Boardman, J. W.&Kruse, F. A. J. I. T. o. G. and Sensing, R. (2011) Analysis of imaging spectrometer data using $ n $-dimensional geometry and a mixture-tuned matched filtering approach, **49**(11), pp. 4138-4152.

Calin, M.-A.&Coman, T.&Parasca, S. V.&Bercaru, N.&Savastru, R. S. and Manea, D. J. J. o. b. o. (2015) Hyperspectral imaging-based wound analysis using mixture-tuned matched filtering classification method, **20**(4), pp. 046004.

Chen, X.&Mao, J. and Tian, H. J. S. (2020) Analysis of China's Iron Trade Flow: Quantity, Value and Regional Pattern, **12**(24), pp. 10427.

Cardoso-Fernandes, J., Teodoro, A.C. and Lima, A. (2019). Remote sensing data in lithium (Li) exploration: A new approach for the detection of Li-bearing pegmatites. *International Journal of Applied Earth Observation and Geoinformation,* **76**, pp.10-25.

Chandola, V., Banerjee, A. and Kumar, V. (2009). Anomaly detection: A survey. ACM computing surveys (CSUR), **41**(3), pp.1-58.

Congalton, R.G., 2007. Thematic and positional accuracy assessment of digital remotely sensed data. In In: McRoberts, Ronald E.; Reams, Gregory A.; Van Deusen, Paul C.; McWilliams, William H., eds. Proceedings of the seventh annual forest inventory and analysis symposium; October 3-6, 2005; Portland, ME. Gen. Tech. Rep. WO-77. Washington, DC: US Department of Agriculture, Forest Service: 149-154. (Vol. **77**).

Crósta, A.&Souza Filho, C.&Azevedo, F. and Brodie, C. (2003) Targeting key alteration minerals in epithermal deposits in Patagonia, Argentina, Using ASTER imagery and principal component analysis, *International Journal of Remote Sensing - INT J REMOTE SENS*, **24**, pp. 4233-4240.

Ducart, D. F.&Silva, A. M.&Toledo, C. L. B. and Assis, L. M. d. J. B. J. o. G. (2016) Mapping iron oxides with Landsat-8/OLI and EO-1/Hyperion imagery from the Serra Norte iron deposits in the Carajás Mineral Province, Brazil, **46**, pp. 331-349.

Ezana mining development (2007). *Progress report on the result of assessment work on iron ore occurrence conducted in Tigray region, Ethiopia*.

Ezana mining development (2011). Mineral resource estimate and technical report on iron deposit of ShireMentebteb area, Northwestern of Tigray region, Ethiopia.

Foody, G.M., (2002). The role of soft classification techniques in the refinement of estimates of ground control point location. *Photogrammetric Engineering and Remote Sensing*, **68**(9), pp.897-904.

Gad, S. and Kusky, T. J. G. R. (2007) ASTER spectral ratioing for lithological mapping in the Arabian–Nubian shield, the Neoproterozoic Wadi Kid area, Sinai, Egypt, **11**, pp. 326-335.

Gad, S. and Kusky, T. J. J. o. A. E. S. (2006) Lithological mapping in the Eastern Desert of Egypt, the Barramiya area, using Landsat thematic mapper (TM), **44**(2), pp. 196-202.

Galvao, L. S.&Formaggio, A. R. and Tisot, D. A. J. R. S. o. E. (2005) Discrimination of sugarcane varieties in Southeastern Brazil with EO-1 Hyperion data, **94**(4), pp. 523-534.

Gandhi, G. M.&Parthiban, S.&Thummalu, N. and Christy, A. J. P. C. S. (2015) Ndvi: Vegetation change detection using remote sensing and gis–A case study of Vellore District, **57**, pp. 1199-1210.

Gardiner, R. K. A., Clarke, John Innes, Dickson, . Kwamina Busumafi , Smedley, . Audrey , McMaster, . David N. , Kröner, . Alfred , Nicol, . Davidson S.H.W. , Middleton, . John F.M. , Steel, . Robert Walter and Mabogunje, . Akinlawon Ladipo. (2021) Africa. Encyclopedia Britannica.

Gopinathan, P.&Parthiban, S.&Magendran, T.&Al-Quraishi, A. M. F.&Singh, A. K.&Singh, P. K. J. R. S. A. S. and Environment (2020) Mapping of ferric (Fe3+) and ferrous (Fe2+)

iron oxides distribution using band ratio techniques with ASTER data and geochemistry of Kanjamalai and Godumalai, Tamil Nadu, south India, **18**, pp. 100306.

Grebby, S., Cunningham, D., Tansey, K. and Naden, J., 2014. The impact of vegetation on lithological mapping using airborne multispectral data: a case study for the north Troodos Region, *Cyprus. Remote Sensing*, **6**(11), pp.10860-10887.

Guha, S., Govil, H., Tripathi, M. and Besoya, M., 2018. Evaluating crosta technique for alteration mineral mapping in Malanjkhand Copper Mines, India. *International Archives of the Photogrammetry, Remote Sensing and Spatial Information Sciences*, **42**(5).

Haldar, S. K. (2018) *Mineral exploration: principles and applications.* Elsevier.

Hamrla, M. J. G. (2019) The iron and manganese ore deposits in Ethiopia, **9**(1), pp. 439-487.

Hosseinjani, M. and Tangestani, M. H. J. I. J. o. D. E. (2011) Mapping alteration minerals using sub-pixel unmixing of ASTER data in the Sarduiyeh area, SE Kerman, Iran, **4**(6), pp. 487-504.

https://lpdaac.usgs.gov/data/get-started-data/collection-overview/missions/aster-overview/.

https://www.usgs.gov/faqs/what-are-band-designations-landsat-satellites?qt-news_science_products=0#qt-news_science_products

Inzana, J.&Kusky, T.&Higgs, G. and Tucker, R. J. J. o. A. E. S. (2003) Supervised classifications of Landsat TM band ratio images and Landsat TM band ratio image with radar for geological interpretations of central Madagascar, **37**(1-2), pp. 59-72.

Jolliffe, I.T. and Cadima, J., 2016. Principal component analysis: a review and recent developments. Philosophical Transactions of the Royal Society A: Mathematical, Physical and Engineering Sciences, **374**(2065), p.20150202.

Kalinowski, A. and Oliver, S., 2004. ASTER mineral index processing manual. Remote Sensing Applications, Geoscience Australia, **37**, p.36.

Kaufmann, H.&Segl, K.&Guanter, L.&Chabrillat, S.&Hofer, S.&Bach, H.&Hostert, P.&Müller, A. and Chlebek, C. 'Review of EnMAP scientific potential and preparation phase'. *6th EARSeL SIG IS Workshop*.

Keshava, N. and Mustard, J. F. J. I. s. p. m. (2002) Spectral unmixing, **19**(1), pp. 44-57.

Kumar, U.&Kerle, N. and Ramachandra, T. (2008) 'Constrained linear spectral unmixing technique for regional land cover mapping using MODIS data', *Innovations and advanced techniques in systems, computing sciences and software engineering*: Springer, pp. 416-423.

Masoumi, F.&Eslamkish, T.&Honarmand, M. and Abkar, A. A. J. R. G. (2017) A comparative study of Landsat-7 and Landsat-8 data using image processing methods for hydrothermal alteration mapping, **67**(1), pp. 72-88.

Mia, B. and Fujimitsu, Y. J. J. o. E. S. S. (2012) Mapping hydrothermal altered mineral deposits using Landsat 7 ETM+ image in and around Kuju volcano, Kyushu, Japan, **121**(4), pp. 1049-1057.

Mishra, B. K.&Pattanayak, S. and Rautray, S. 'Geospatial and geological mapping of iron ore prospective zones in Singhbhum-Keonjhar belt, Orissa'.

MOME (2009) *Mineral Resources of Ethiopia Annual Report*.

Mulugeta Alene&Jenkin, G. R.&Leng, M. J. and Darbyshire, D. F. J. P. R. (2006) The Tambien Group, Ethiopia: an early Cryogenian (ca. 800–735 Ma) neoproterozoic sequence in the Arabian–Nubian shield, **147**(1-2), pp. 79-99.

Mundt, J. T.&Streutker, D. R. and Glenn, N. F. 'Partial unmixing of hyperspectral imagery: theory and methods'. *Proceedings of the American Society of photogrammetry and remote sensing*.

Neway Kifle and Binyam Tesfaw. (2021). Mapping Effects of Urban Blue-Green Landscapes on Land Surface Temperature Using Geo-Spatial Techniques: The Case of Addis Ababa, Ethiopia. *Unpublished thesis work.*

Ni, L.&Xu, H.&Zhou, X. J. I. J. o. S. T. i. A. E. O. and Sensing, R. (2020) Mineral Identification and Mapping by Synthesis of Hyperspectral VNIR/SWIR and Multispectral TIR Remotely Sensed Data With Different Classifiers, **13**, pp. 3155-3163.

Osinowo, O.O., Gomy, A. and Isseini, M., 2021. Mapping hydrothermal alteration mineral deposits from Landsat 8 satellite data in Pala, Mayo Kebbi Region, Southwestern Chad. *Scientific African*, **11**, p.e00687.

Ourhzif, Z.&Algouti, A.&Hadach, F. J. I. A. o. t. P., Remote Sensing and Sciences, S. I. (2019) lithological mapping using Landsat 8 OLI and ASTER multispectral data in imini-ounilla district south high atlas of Marrakech.

Pour, A. B.&Hashim, M.&Hong, J. K. and Park, Y. J. O. G. R. (2019) Lithological and alteration mineral mapping in poorly exposed lithologies using Landsat-8 and ASTER satellite data: North-eastern Graham Land, Antarctic Peninsula, **108**, pp. 112-133.

Pour, A. B.&Hashim, M. and Marghany, M. J. I. J. o. P. S. (2011) Using spectral mapping techniques on short wave infrared bands of ASTER remote sensing data for alteration mineral mapping in SE Iran, **6**(4), pp. 917-929.

Pour, A. B. and Hashim, M. J. O. g. r. (2012) The application of ASTER remote sensing data to porphyry copper and epithermal gold deposits, **44**, pp. 1-9.

Pour, A. B. and Hashim, M. J. S. (2014) ASTER, ALI and Hyperion sensors data for lithological mapping and ore minerals exploration, **3**(1), pp. 1-19.

Pour, A.B., Zoheir, B., Pradhan, B. and Hashim, M. (2021). Editorial for the Special Issue: Multispectral and hyperspectral remote sensing data for mineral exploration and environmental monitoring of mined areas.

Powell, V. and Lehe, L. J. U. h. s. i. e. p.-a. (2015) Principal component analysis.

Prasad, T. and Parthasarathy, G. (2018) Laterite and Laterization-A Geomorphological Review, *International Journal of Science and Research (IJSR)*, **7**(4), pp. 578-583.

Qiu, F.&Abdelsalam, M. and Thakkar, P. J. J. o. A. E. S. (2006) Spectral analysis of ASTER data covering part of the Neoproterozoic Allaqi-Heiani suture, Southern Egypt, **44**(2), pp. 169-180.

Rajendran, S.&Al-Khirbash, S.&Pracejus, B.&Nasir, S.&Al-Abri, A. H.&Kusky, T. M. and Ghulam, A. J. O. g. r. (2012) ASTER detection of chromite bearing mineralized zones in Semail Ophiolite Massifs of the northern Oman Mountains: Exploration strategy, **44**, pp. 121-135.

Rajendran, S.&Nasir, S.&Kusky, T. M.&Ghulam, A.&Gabr, S. and El-Ghali, M. A. J. O. g. r. (2013) Detection of hydrothermal mineralized zones associated with listwaenites in Central Oman using ASTER data, **53**, pp. 470-488.

Ranjbar, H.&Honarmand, M. and Moezifar, Z. J. J. o. A. E. S. (2004) Application of the Crosta technique for porphyry copper alteration mapping, using ETM+ data in the southern part of the Iranian volcanic sedimentary belt, **24**(2), pp. 237-243.

Rouskov, K.&Popov, K.&Stoykov, S. and Yamaguchi, Y. 'Some applications of the remote sensing in geology by using of ASTER images'. *Scientific Conf."SPACE, ECOLOGY, SAFETY" with Int. Participation*, 167-173.

Rowan, L.&Crowley, J.&Schmidt, R.&Ager, C. and Mars, J. J. J. o. G. E. (2000) Mapping hydrothermally altered rocks by analyzing hyperspectral image (AVIRIS) data of forested areas in the Southeastern United States, **68**(3), pp. 145-166.

San, B.T., Sumer, E.O. and Gurcay, B., (2004), July. *Comparison of band ratioing and spectral indices methods for detecting alunite and kaolinite minerals using ASTER data in Biga region, Turkey*. In Proceedings ISPRS.

Schubert, G. (2015) *Treatise on geophysics.* Elsevier.

Sentayehu Berihun, Mohamed. (2018) characterizing the surface mineralogy in the aggeneys sedex system with hyperspectral imagery.

Settle, J. J. I. T. o. G. and Sensing, R. (2006) On the effect of variable endmember spectra in the linear mixture model, **44**(2), pp. 389-396.

Shi, C.&Wang, L. J. I. T. o. G. and Sensing, R. (2016) Linear spatial-spectral mixture model, **54**(6), pp. 3599-3611.

Shi, C. and Wang, L. J. R. S. o. E. (2014) Incorporating spatial information in spectral unmixing: A review, **149**, pp. 70-87.

Solomon Gebresilassie&Bheemalingeswara, K. and Fiseha Adhanom, J. I. J. E. S. E. (2012) Geology and characteristics of meta-limestone-hosted iron deposit near Negash, Tigray and northern Ethiopia, **5**, pp. 1535-1544.

Solomon Tadesse (2009) *Mineral resources potential of Ethiopia.* Addis Ababa: Addis Ababa University Press.

Tarekegn Tadesse &Hoshino, M.&Suzuki, K. and Iizumi, S. J. J. o. A. E. S. (2000) SmNd, Rb-Sr and ThUPb zircon ages of syn-and post-tectonic granitoids from the Axum area of northern Ethiopia, **30**(2), pp. 313-327.

Teklay Gidey&Miruts Hagos, M.&Konka, B. and Azeb Gebremicale, J. J. o. A. E. S. (2020) Genesis and characteristics of lateritic iron deposit in Mai-Kuhli area, western Tigray, northern Ethiopia, **172**, pp. 104005.

Tompolidi, A.-M.&Sykioti, O.&Koutroumbas, K. and Parcharidis, I. J. R. S. (2020) Spectral Unmixing for Mapping a Hydrothermal Field in a Volcanic Environment Applied on ASTER, Landsat-8/OLI, and Sentinel-2 MSI Satellite Multispectral Data: The Nisyros (Greece) Case Study, **12**(24), pp. 4180.

Transon, J.&d'Andrimont, R.&Maugnard, A. and Defourny, P. J. R. S. (2018) Survey of hyperspectral earth observation applications from space in the sentinel-2 context, **10**(2), pp. 157.

TRAORE, M.&ÇAN, T. and TEKİN, S. 'Discrimination of Iron Deposits Using Feature-Oriented Principal Component Selection and Band Ratio Methods: Eastern Taurus/TURKEY'. *International Symposium on Applied Geoinformatics (ISAG2019) was held in Istanbul on*, 9.

Van der Meer, F. D.&Van der Werff, H. M.&Van Ruitenbeek, F. J.&Hecker, C. A.&Bakker, W. H.&Noomen, M. F.&Van Der Meijde, M.&Carranza, E. J. M.&De Smeth, J. B.&Woldai, T. J. I. J. o. A. E. O. and Geoinformation (2012) Multi-and hyperspectral geologic remote sensing: A review, **14**(1), pp. 112-128.

Van Der Meer, F. J. I. J. o. R. S. (1999) Iterative spectral unmixing (ISU), **20**(17), pp. 3431-3436.

Wambo, J.D.T., Pour, A.B., Ganno, S., Asimow, P.D., Zoheir, B., dos Reis Salles, R., Nzenti, J.P., Pradhan, B. and Muslim, A.M. (2020). Identifying high potential zones of gold mineralization in a sub-tropical region using Landsat-8 and ASTER remote sensing data: A case study of the Ngoura-Colomines goldfield, eastern Cameroon. Ore Geology Reviews, 122, p.103530.

Widdowson, M. J. G. s. l. (2007) Laterite and ferricrete, pp. 488pp.

Winter, M. E, (2000*)*. 'Comparison of approaches for determining end-members in hyperspectral data'. *IEEE Aerospace Conference. Proceedings (Cat. No. 00TH8484)*: IEEE, 305-313.

Zhou, Z.G., Tang, P. and Zhou, M., (2016). Detecting anomaly regions in satellite image time series based on seasonal autocorrelation analysis. *ISPRS Annals of the Photogrammetry, Remote Sensing and Spatial Information Sciences*, **3**, p.303.

Appendices

Appendix 1. Vegetation masked ASTER image.

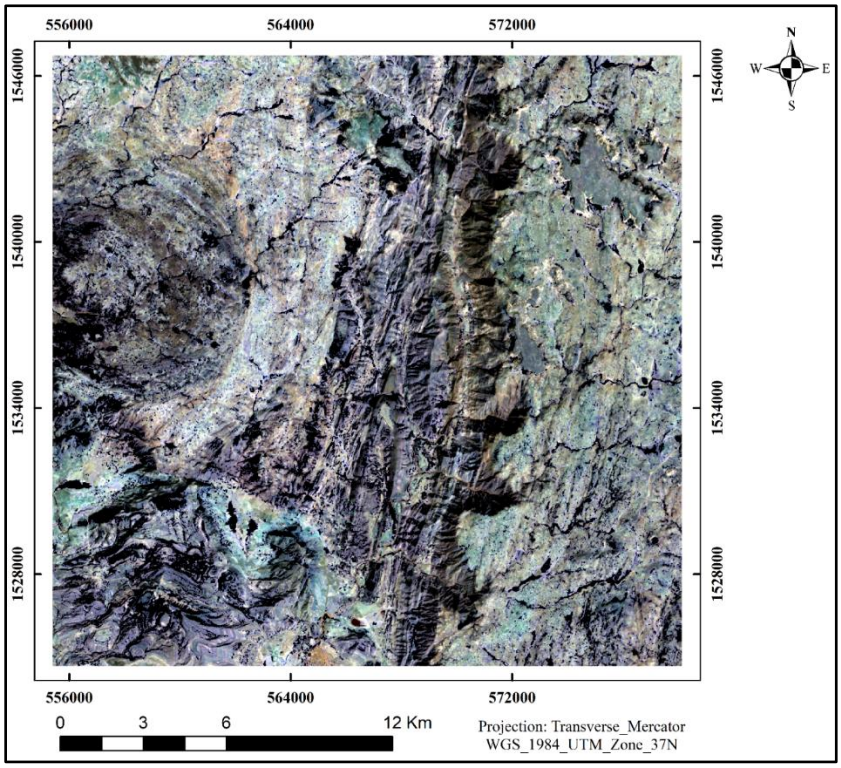

Appendix 2. Landsat 8 OLI vegetation masked map.

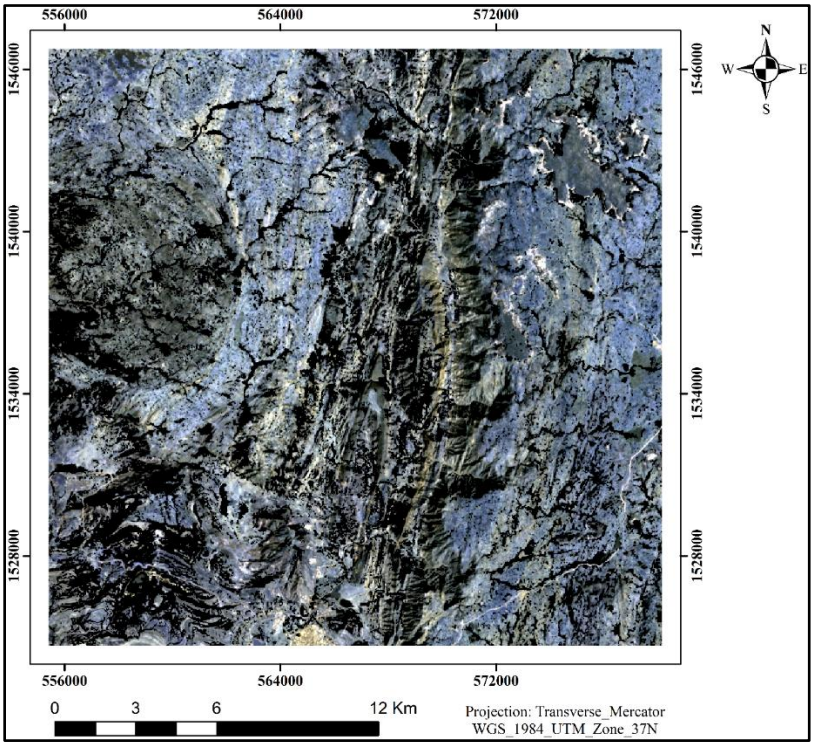

Appendix 3. PPI images(a) ASTER and (b) Landsat 8 OLI.

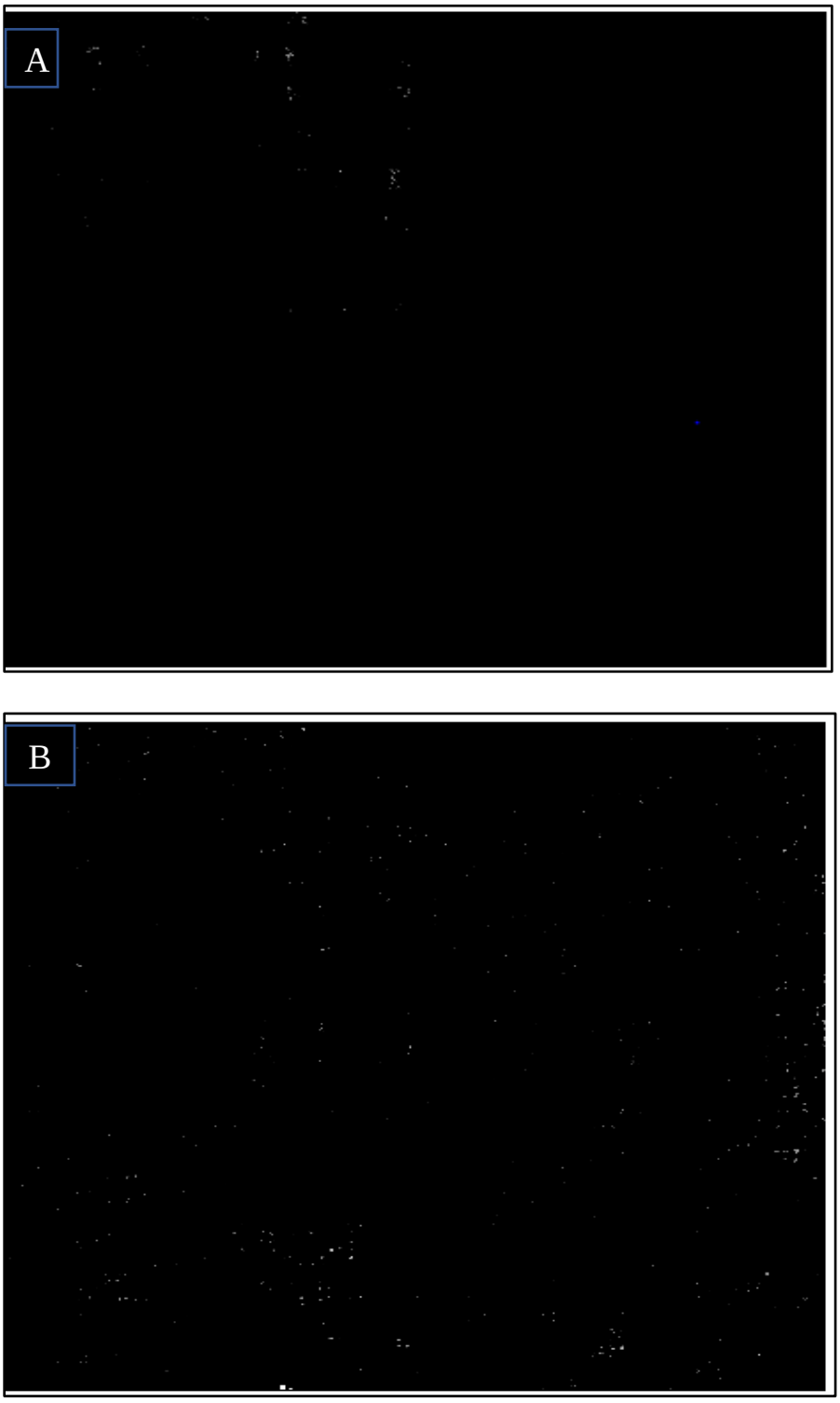

Appendix 4. Existing iron oxide map (source: Solomon Gebreslassie et al., 2012).

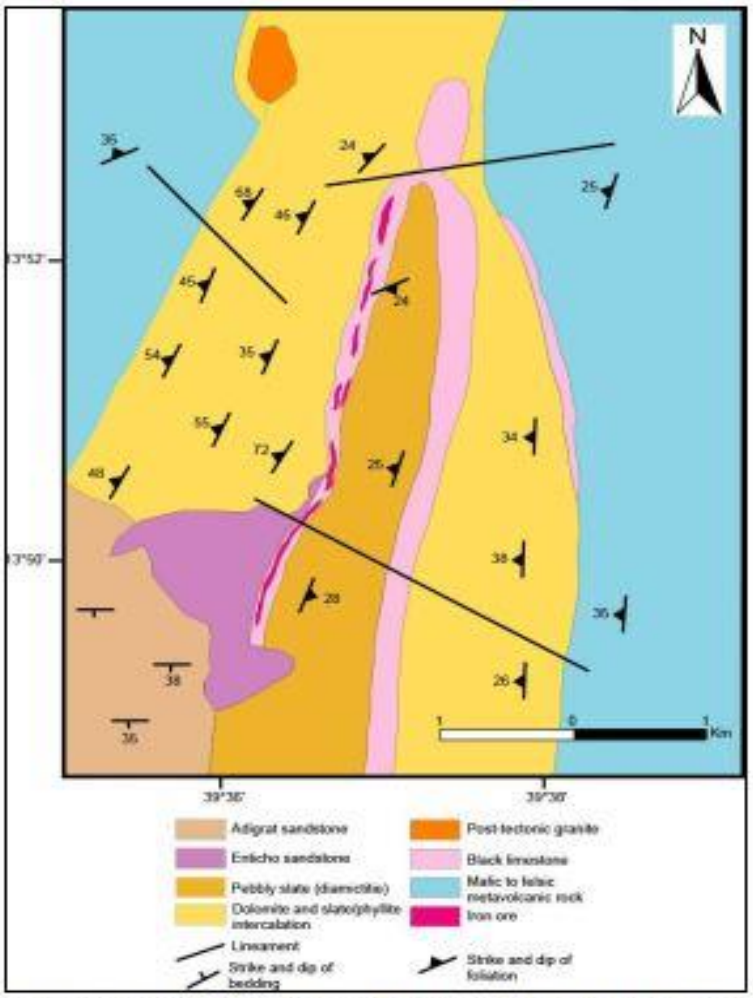

Figure 3: Geological Map of the Mukuat Area Showing the Outcrops of Both Tsaliet and Tambien Groups along with Iron Ore Lenses